



**THE DESIGN AND ANALYSIS OF ELECTRICALLY LARGE
CUSTOM-SHAPED REFLECTOR ANTENNAS**

THESIS

Joshua M. Wilson, Civilian Student, USAF

AFIT-ENG-13-J-08

**DEPARTMENT OF THE AIR FORCE
AIR UNIVERSITY**

AIR FORCE INSTITUTE OF TECHNOLOGY

Wright-Patterson Air Force Base, Ohio

DISTRIBUTION STATEMENT A:
APPROVED FOR PUBLIC RELEASE; DISTRIBUTION UNLIMITED

The views expressed in this thesis are those of the author and do not reflect the official policy or position of the United States Air Force, the Department of Defense, or the United States Government.

This material is declared a work of the U.S. Government and is not subject to copyright protection in the United States.

AFIT-ENG-13-J-08

THE DESIGN AND ANALYSIS OF ELECTRICALLY LARGE
CUSTOM-SHAPED REFLECTOR ANTENNAS

THESIS

Presented to the Faculty
Department of Electrical and Computer Engineering
Graduate School of Engineering and Management
Air Force Institute of Technology
Air University
Air Education and Training Command
in Partial Fulfillment of the Requirements for the
Degree of Master of Science in Electrical Engineering

Joshua M. Wilson, B.S.E.E.

Civilian Student, USAF

June 2013

DISTRIBUTION STATEMENT A:
APPROVED FOR PUBLIC RELEASE; DISTRIBUTION UNLIMITED

THE DESIGN AND ANALYSIS OF ELECTRICALLY LARGE CUSTOM-SHAPED REFLECTOR ANTENNAS

Joshua M. Wilson, B.S.E.E.
Civilian Student, USAF

Approved:

/signed/

 Andrew J. Terzuoli, PhD (Chairman)

16 May 2013

Date

/signed/
Jonathan T. Black, PhD (Member)

21 May 2013

Date

/signed/
Peter J. Collins, PhD (Member)

21 May 2013

Date

/signed/
 Ronald J. Marhefka, PhD (Member)

16 May 2013

Date

/signed/

 Alan L. Jennings, PhD (Member)

20 May 2013

Date

Abstract

Designing and analyzing electrically large reflectors poses numerically complex problems because the reflector must be sampled finely to obtain an accurate solution, causing an unwieldy number of samples. In addition to these complexities, a custom-shaped reflector poses a new analysis problem. Previously developed methods and theorems including Geometric Optics, Ray-Tracing, Surface Equivalence Theorems, Image Theory, and Physical Optics can be applied to these custom-shaped reflectors however. These methods all share in common their capability to provide accurate results in the analysis of electrically large structures. In this thesis, two custom-shaped reflector concepts are explored which include a rectangular shaped, spherically contoured reflector with largest dimension of 305 meters and a cross-shaped, parabolically contoured reflector with largest dimension of 150 meters. Each reflector is intended to operate in the Institute of Electrical and Electronics Engineers (IEEE) L-Band. The reflectors produced differing results, but the same methods apply to each. The motivation for pursuing these custom-shaped reflectors is for earth-based and space-based satellite communications respectively. In this thesis, the plane wave analysis and the ray tracing results are presented for each reflector, and the initial feed design results for the cross-shaped reflector are presented.

To my family and friends.

Acknowledgments

The author would like to thank several individuals for their contributions to this research without whom, it would have not been possible to complete. These include: Dr. Andrew J. Terzuoli Jr. for all the discussions and guidance; Lee R. Burchett for his help in getting the research up and running; Dr. Alan L. Jennings for his thorough review of this thesis from a different perspective; Dr. David K. Vaughan for his thorough review of this thesis stylistically; Dr. Teh-Hong Lee for all his help in performing the SatCom[™] simulations; Dr. Don Pflug for taking the time to review the presentations and provide useful feedback; John Cetnar for taking the time to discuss about the research and provide useful feedback; Dr. Ronald J. Marhefka for reviewing this thesis and working as a consultant for this research; Luke Fredette for his help in performing the sky study; Dr. Michael J. Havrilla for taking the time to help brainstorm research directions for this thesis; Dr. Peter J. Collins for participating as a committee member and providing good direction for this thesis; Dr. Jonathan T. Black for participating as a committee member and providing good feedback from the sponsor point of view; The Department of Aeronautical and Astronautical Engineering Satellite Tracking Group at Air Force Institute of Technology (AFIT) for providing the necessary direction on the sky study; Stephen Hartzell for his help in getting the research up and running; Thang Tran for taking the time to provide feedback from a different perspective, Joshua Kaster for providing good feedback from a different perspective; Amanda Kirk for listening about the project and working as the network administrator where this research took place, and Andre Flory for providing his services as the previous network administrator where this research took place.

Joshua M. Wilson

Table of Contents

	Page
Abstract	iv
Dedication	v
Acknowledgments	vi
Table of Contents	vii
List of Figures	x
List of Tables	xiv
List of Symbols	xv
List of Acronyms	xvii
 I. Introduction	 1
1.1 Background	1
1.1.1 Rectangular Shaped, Spherically Contoured Reflector	2
1.1.2 Cross-Shaped, Parabolically Contoured Reflector	2
1.2 Assumptions, Limitations, and Standards	3
1.3 Approach and Methodology	4
1.4 Materials & Equipment	5
1.5 Scope	6
1.6 Overview	7
 II. Background & Literature Review	 8
2.1 Geometric Optics (GO)	8
2.2 Solutions to Maxwell's Equations in the Far-Field (FF) Using Vector Potentials	12
2.3 The Physical Optics (PO) Approximation and Equivalence Theorems	19
2.3.1 The PO Approximation	20
2.3.2 Surface Equivalence Theorem and Image Theory	20
2.4 Two-Dimensional Transverse Magnetic (TM) ^z and Transverse Electric (TE) ^z	
Field Set Relations	22
2.5 Reciprocity of Antenna FF Radiation Patterns	27
2.6 Overview of Method of Moments (MoM)	27

	Page
III. Methodology	34
3.1 Geometrical Analysis	35
3.1.1 Rectangular Shaped, Spherically Contoured Reflector Geometry . .	36
3.1.2 Ray-Tracing Procedure: Rectangular Shaped, Spherically Con- toured Reflector	37
3.1.3 Cross-shaped, Parabolically Contoured Reflector Geometry	39
3.1.4 Ray-Tracing Procedure: Cross-shaped, Parabolically Contoured Reflector	40
3.2 Plane Wave Analysis	42
3.2.1 Rectangular Shaped, Spherically Contoured Reflector	43
3.2.2 Cross-shaped, Parabolically Contoured Reflector	46
3.3 Sky Study for the Rectangular Shaped, Spherically Contoured Reflector . .	48
3.4 Baseline Calculation for the Cross-shaped, Parabolically Contoured Reflector	51
3.5 Feed Design for the Cross-shaped, Parabolically Contoured Reflector . . .	55
3.5.1 Solving for the Field Distributions Within the Cross-Shaped Aperture using a Finite-Difference (FD) Approach to Eigenmode Analysis	58
3.5.2 Solving for the FF Radiation Pattern of the Cross-Shaped Aperture Using Love's Equivalence Principle	61
3.5.3 Discretizing the Laplacian Operator Using a Central Difference Approximation	64
3.5.4 Numerically Computing the FF Radiation Pattern of the Cross- Shaped Aperture	66
IV. Results & Analysis	70
4.1 Geometrical Analysis	70
4.1.1 Ray-Tracing Procedure: Rectangular Shaped , Spherically Con- toured Reflector	71
4.1.2 Ray-Tracing Procedure: Cross-shaped, Parabolically Contoured Reflector	73
4.2 Plane Wave Analysis	75
4.2.1 Rectangular Shaped, Spherically Contoured Reflector	77
4.2.2 Cross-shaped, Parabolically Contoured Reflector Geometry	80
4.3 Sky Study for the Rectangular Shaped, Spherically Contoured Reflector . .	82
4.4 Baseline Calculation for the Cross-shaped, Parabolically Contoured Reflector Geometry	84
4.5 Feed Design for the Cross-shaped, Parabolically Contoured Reflector Geometry	88

	Page
V. Discussion	100
5.1 Geometrical Analysis	101
5.1.1 Ray-Tracing Procedure: Rectangular Shaped, Spherically Contoured Reflector	101
5.1.2 Ray-Tracing Procedure: Cross-shaped, Parabolically Contoured Reflector Geometry	102
5.2 Plane Wave Analysis	102
5.2.1 Rectangular Shaped, Spherically Contoured Reflector	102
5.2.2 Cross-shaped, Parabolically Contoured Reflector Geometry	103
5.3 Sky Study for the Rectangular, Spherically Contoured Reflector	104
5.4 Baseline Calculation for the Cross-shaped, Parabolically Contoured Reflector Geometry	104
5.5 Feed Design for the Cross-shaped, Parabolically Contoured Reflector Geometry	105
5.6 Future Work	106
Appendix: MATLAB Code	107
Bibliography	129
Vita	131

List of Figures

Figure	Page
2.1 Spherical reflector geometry	9
2.2 Spherical reflector geometry; Analyzing inherent aberrations	11
2.3 Caustic by ray tracing [1]	12
2.4 Illustration of the Parallel Ray Approximation	17
2.5 Spherical coordinate system	18
2.6 Illustration of Image Theory applied to linear elements above perfect conductors [2]	23
2.7 Illustration of a particular application of Love's Equivalence Principle to a rectangular aperture set in an infinite ground plane	23
3.1 Geometry illustration for the spherical reflector	36
3.2 A chord of a circle	37
3.3 Conceptual drawing of the sparse reflector	40
3.4 Side-looking view of the sparse reflector	41
3.5 Coordinate convention used for Plane Wave Analysis of the rectangular shaped, spherically contoured reflector	44
3.6 Illustration of vectors used in performing the Fresnel-Kirchoff Diffraction Integral (FKDI) computations	45
3.7 Plot of the FF radiation pattern used as a plane wave source in plane wave analysis for the sparse reflector	48
3.8 Illustration of an analemma pattern traced out by a Geosynchronous (GEO) satellite over the course of one year. This is only a specific example and does not account for all GEO satellites	50
3.9 Two Line Element (TLE) example for the international space station	51

Figure	Page
3.10 Illustration of pyramidal horn antenna designed to feed the filled aperture Cassegrain system	54
3.11 Cross-shaped aperture concept for feeding structure of sparse reflector	56
3.12 Cross-shaped phased array concept for feeding structure of sparse reflector	57
3.13 The needed beamwidths to illuminate the entire cross-shaped reflector	58
3.14 Trigonometry used to solve for needed beamwidths and aperture feeding structure dimensions	59
3.15 Coordinate convention used in Eigenmode analysis for cross-shaped aperture	59
3.16 Illustration of how the discrete grid for the cross-shaped aperture is indexed for numerically evaluating the Laplacian operator	65
3.17 Discretizing the Laplacian operator generates a sparse matrix that follows a specific pattern as shown here	67
3.18 A single subdomain used to perform Nine-Point Integration over the cross- shaped aperture	68
4.1 Ray-tracing for 2-Dimensional cross-section of the spherical reflector with formation of caustic envelope highlighted. Only the incident and reflected rays are plotted.	72
4.2 Ray-tracing for 3-Dimensional cross-section the spherical reflector with formation of caustic envelope highlighted. Only the incident and reflected rays are plotted.	74
4.3 Ray-tracing for 2-Dimensional cross-section of the sparse reflector with focal point highlighted	75
4.4 Ray-tracing for 3-Dimensional cross-section of the sparse reflector: (a) Oblique view illustrating cross-shape (b) Side-view with focal point highlighted	76

Figure	Page
4.5 Left: On-axis propagation, no blockage amplitude distribution calculated using Fourier Analysis; Right: Tilted propagation at 5° azimuth and 2° elevation, no blockage amplitude distribution calculated using Fourier Analysis	78
4.6 Left: On-axis propagation, no blockage amplitude distribution calculated using FKDI Analysis; Right: Tilted propagation at 5° azimuth and 2° elevation, no blockage amplitude distribution calculated using FKDI Analysis	80
4.7 FF radiation pattern for the sparse reflector, in dB, with plane wave incident. Plot generated using MATLAB® and data generated by SatCom™	82
4.8 Resulting layout of locations needed to use the spherical reflector to communicate with all GEO satellites over the Continental United States (CONUS). Note that the specific latitudes of these locations is of interest and the city names are merely for reference.	84
4.9 Resulting layout of locations needed to use the rectangular shaped, spherically contoured reflector to communicate with all GEO satellites over the CONUS. This is shown to illustrate the criss-crossing view angles from each antenna location	85
4.10 FF radiation pattern 2-Dimensional planar cut for the L-Band Horn antenna designed for the baseline antenna system in Section 3.4	86
4.11 Wire frame view of the 50 meter diameter circular, parabolically contoured reflector used as the baseline antenna system for the sparse reflector. Graphic generated using SatCom™	87
4.12 FF radiation pattern 2-Dimensional planar cut for the baseline antenna system fed by the L-Band Horn antenna shown in Figure 3.10	88
4.13 First 10 TM^z approximated modes, square aperture, $N = 165$	89
4.14 First 10 TE^z approximated modes, square aperture, $N = 165$	89

Figure	Page
4.15 $\phi = 0, 0 \leq \theta \leq \pi/2$ planar cut of FF radiation pattern, in dB, of a $3\lambda \times 3\lambda$ square aperture excited by a uniform field distribution	91
4.16 Graphic showing the cross-shaped aperture feeding structure suspended above the sparse reflector. The cross-shaped aperture is intended to avoid illuminating the regions between the sparse reflector arms	92
4.17 First 10 TM^z approximated modes, Cross-Aperture, $N = 165$	93
4.18 First 10 TE^z approximated modes, Cross-Aperture, $N = 165$	94
4.19 $\phi = 0, 0 \leq \theta \leq \pi/2$ planar cut of FF radiation pattern, in dB, of cross-shaped aperture excited by lowest order TE^z mode	96
4.20 $\phi = 0, 0 \leq \theta \leq \pi/2$ planar cut of FF radiation pattern, in dB, of cross-shaped aperture excited by lowest order TM^z mode	97
4.21 $\phi = \pi/4, 0 \leq \theta \leq \pi/2$ planar cut of FF radiation pattern, dB, of cross-shaped aperture excited by lowest order TE^z mode	98
4.22 $\phi = \pi/4, 0 \leq \theta \leq \pi/2$ planar cut of FF radiation pattern, in dB, of cross-shaped aperture excited by lowest order TM^z mode	99

List of Tables

Table	Page
3.1 Specifications for filled parabolic reflector Cassegrain system compared to the Deep Space Network (DSN) Station 11	53
3.2 Nine-point integration rule weights	69
4.1 Geometrical analysis results of each reflector	71
4.2 Cutoff frequencies for first 10 TM^z and TE^z modes respectively, Aperture dimensions $a = b = 0.405m$	90
5.1 Summary of results from the Plane Wave Analysis of sparse reflector and baseline antenna simulation	105

List of Symbols

Symbol	Definition
α	Attenuation Constant
β	Phase Constant
γ	Propagation Constant
ϵ	General Permittivity
ϵ_0	Permittivity of Free-Space
η	Intrinsic Impedance $\left(\eta = \sqrt{\frac{\mu}{\epsilon}}\right)$
λ	Wavelength or eigenvalue
μ	General Permeability
μ_0	Permeability of Free-Space
σ_e	Electrical Conductivity
σ_m	Magnetic Conductivity
f	Frequency (Hz)
ω	Frequency (rad/s)
z	Intrinsic Impedance [3]
y	Intrinsic Admittance [3]

Subscripts

c	Cutoff
i	Incident Field
mn	Transverse Mode Number
p	Induced Current Density
R	Cartesian Coordinate System
S	Spherical Coordinate System

Symbol	Definition
--------	------------

s	Surface
-----	---------

t	Transverse
-----	------------

$trial$	Initial Guess for a Quantity to Try
---------	-------------------------------------

u	Individual Vector Component (i.e. x , y , or z)
-----	--

Superscripts

R	Cartesian Coordinate System
-----	-----------------------------

S	Spherical Coordinate System
-----	-----------------------------

s	Scattered Field
-----	-----------------

z	Transverse to \hat{z}
-----	-------------------------

List of Acronyms

Acronym	Definition
AFIT	Air Force Institute of Technology
AGI	Analytical Graphics Inc.
CEM	Computational Electromagnetics
CONUS	Continental United States
DSN	Deep Space Network
FD	Finite-Difference
FF	Far-Field
FKDI	Fresnel-Kirchoff Diffraction Integral
FNBW	First Null Beam Width
FSGF	Free Space Green's Function
GEO	Geosynchronous
GO	Geometric Optics
HPBW	Half Power Beam Width
IEEE	Institute of Electrical and Electronics Engineers
LOREnet	Low Observables Radar Electromagnetics network
MoM	Method of Moments
NASA	National Aeronautics and Space Administration
OSU	The Ohio State University
PEC	Perfect Electric Conductor
PMC	Perfect Magnetic Conductor
PO	Physical Optics
STK	Systems Tool Kit
TE	Transverse Electric

Acronym	Definition
TLE	Two Line Element
TM	Transverse Magnetic

THE DESIGN AND ANALYSIS OF ELECTRICALLY LARGE CUSTOM-SHAPED REFLECTOR ANTENNAS

I. Introduction

For this research, two reflector antenna design concepts are explored. The first is a rectangular shaped, spherically contoured reflector (spherical reflector), and the second is a cross-shaped, parabolically contoured reflector (sparse reflector). Each reflector is comparatively large with respect to the wavelengths of operation making them electrically large structures. Also, both reflectors have a custom-shaped cross-section as opposed to the typical circular cross-section due to their intended applications [2] [4] [5]. The aim of this research is to provide a design and analysis of these reflectors by studying the geometry and focal regions of both, and devising feeding antenna designs with analysis. Both reflector antennas pose a technical challenge where conventional design and analysis methods can be applied using the proper approximations and assumptions to be described later.

1.1 Background

Satellite communications require antennas that have high directivity to overcome the attenuation of signals due to the long travel distance and the earth's atmosphere. The most suitable antennas to provide high directivity are reflector antennas. These antennas are analogous to aperture antennas, but have the added benefit of higher directivity than that of typical aperture antennas [6]. A reflector antenna can also be made very large in order to increase the directivity. Reflector antenna directivity is directly proportional to the operational frequency and the effective reflector size [2] [6]. The reflector effective size can be determined from the physical size of the reflector [2] [6]. For the IEEE L-Band

frequency range, which is the particular frequency band of interest for this research, and the need for high directivity, the reflectors will be comparatively much larger than a wavelength in physical size, or electrically large.

1.1.1 Rectangular Shaped, Spherically Contoured Reflector.

The spherical reflector antenna is intended to be an earth-based satellite communications antenna. To avoid moving the spherical reflector it is typical to instead move the feeding structure to perform antenna steering. Steering in this manner is feasible because spherical reflectors do not direct all incident energy to a particular focal point, but rather to a line (paraxial) that shifts depending on the direction of incident energy on the reflector. In addition, spherical reflector antennas have a wide angle of steering as compared to parabolically contoured reflectors, which has motivated much research resulting in optimized designs, such as the Arecibo Observatory in Puerto Rico. A spherical reflector antenna system of similar scale to the Arecibo antenna can be used efficiently for satellite communications with the proper design of a feed antenna or system. However, the challenge in designing a proper feed antenna is correcting for inherent spherical aberrations of the reflector. Spherical aberrations are imperfections in the phase of a reflected wave front measured at the paraxial focus, or half the radius of curvature of the reflector [7]. The aberrations become even more prominent with electrically large spherical reflectors [2]. This research studies these aberrations to be able to propose a feeding structure design for the spherical reflector.

1.1.2 Cross-Shaped, Parabolically Contoured Reflector.

The sparse reflector is intended to be a space-based communications antenna. A major trade-off in designing and building large reflector antennas is their ability to deploy. Typically, a large reflector antenna is a solid structure that cannot be made smaller for deployability [2] [4] [6] [8]. In order to make a large reflector antenna more easily deployable, limiting the aperture to a sparse cross-section with foldable segments is a possible solution. The term

sparse used here is defined as a subset of a circular or complete aperture and in particular, a cross-shaped subset. Other work in deployable reflector antennas has been done, but none has proposed a sparse cross-section reflector. However, other published work includes folding reflector antennas comprised of flat plates that resemble a complete aperture when deployed [9] [10] [11], folding mesh reflectors [12], and inflatable reflector antennas [13]. Each of these concepts is different from the cross-shaped reflector concept and is much smaller in scale.

1.2 Assumptions, Limitations, and Standards

A convention used to approximate the design of electrically large reflector antennas is to use optical approximations. In particular, for the reflectors considered here:

1. The surface area is assumed to be much greater than the edge surface area (10λ wide ring) for the reflector [14].
2. The reflector is much larger than a wavelength (L-Band) [14].
3. The reflector is symmetric about the optical axis (axis extending from the center of the reflector) [14].
4. The radius of curvature for the spherical reflector and the focal length for the sparse reflector is large in comparison to a wavelength [14].
5. The incident waves are planar or their deviation from planar is less than $1/4$ of a wavelength [14].

These assumptions allow the use of Geometric Optics (GO) and ray-tracing. Ray-tracing assumes incident energy upon a reflecting surface can be represented as rays, and all reflections are treated using Snell's Law of Reflection [1] [15].

With regards to the sparse reflector, the Physical Optics (PO) approximation is used. This approximation assumes that the reflector is electrically large and is a good conducting material [2] [16] [17]. In particular, for this research, both reflector antennas are assumed to be Perfect Electric Conductor (PEC) materials. The PO approximation assumes that the scattered field, radiated by an induced current density from an incident field (from the

feed or other antenna), is equal to the incident field [2] [16] [17]. This approximation takes advantage of image theory under the assumptions that the perfectly conducting structures are locally planar and infinite in extent. Each reflector explored in this research satisfies these assumptions because they are electrically large [2].

It is important to note that in comparison to other methods for Far-Field (FF) analysis of electrically large radiating structures, such as Method of Moments (MoM) and the Finite Element Method (FEM), the use of optical approximations, surface equivalence theorems, and the PO approximation simplify the analysis and reduce the computational complexity of the radiating structures. The application of each method uses the $e^{+j\omega t}$ time convention for phasor domain quantities. These methods are valid based on the assumptions previously stated. If any one of the assumptions is not met, other more computationally intensive methods must be utilized for FF analysis. In order to perform the more computationally intensive methods, an antenna is typically sampled ten times per wavelength to yield accurate results [18]. This sampling is computationally infeasible for the reflector antennas explored in this thesis because of the large number of samples that result.

Finally, surface equivalence theorems simplify the analysis of the reflector surfaces and the aperture feeding structure concept for the sparse reflector described later. Specifically, Love's Equivalence Principle is important for simulating the cross-shaped aperture feeding structure for the sparse reflector [2] [16] [19]. The only limitation is that Love's Equivalence Principle constrains the regions where the field calculations are valid. Care must be taken to ensure that the fields calculated using Love's Equivalence Principle are valid.

1.3 Approach and Methodology

Both reflector antennas in this thesis pose a technical challenge that can be analyzed using conventional methods with careful considerations given to the assumptions required by each method. The aim of this research is to use multiple methods to obtain an overall system design of each reflector antenna. The approach taken for the design and analysis of each

of the two reflector antennas in this thesis is similar except special procedures that apply to the intended usage for each reflector. In particular, the spherical reflector includes a sky study to determine additional constraints on its geometry and the sparse reflector includes the design and analysis of a 50 meter diameter circular shaped, parabolically contoured baseline reflector antenna system for comparisons of the results. However, the other design procedures are similar for both reflector antennas and include:

1. Geometrical analysis
2. Plane wave analysis
3. Feed antenna system design
4. Feed antenna analysis

Each method is valid for the design of a specific reflector antenna system. However, the methods produce results with differing accuracies and some methods produce unique results that are needed in the final design analysis. The application of the procedures in the order shown here is based on which procedures require results from other procedures. For instance, the feed design step requires input from the results of the plane wave analysis. Also, the order is based on which methods produce more accurate results, where the latter methods are more accurate than the former methods. Results of each procedure will be unique according to the reflector antenna system.

1.4 Materials & Equipment

The AFIT Low Observables Radar Electromagnetics network (LOREnet) laboratory was utilized for the research in this thesis. This laboratory is an independent network of high powered computers with several current Computational Electromagnetics (CEM) software packages installed for student research. Due to the sensitive nature of topics discussed and software utilized, access to LOREnet is restricted. However, the research, simulations, document composition, and communications needed to complete this thesis were all approved.

For completion of the sky study for the spherical reflector, Systems Tool Kit (STK) software from Analytical Graphics Inc. (AGI) is used. In completing the cross-shaped aperture feeding structure simulations, MATLAB® is used. Finally, the simulations of the sparse reflector and the baseline antenna are all completed using SatCom™ software. SatCom™ is a CEM software package that incorporates the use of the MoM, the Geometrical Theory of Diffraction, and the Physical Theory of Diffraction to analyze antenna structures. SatCom™ is provided by The Ohio State University (OSU) under a specific agreement stating that the software be used strictly for academic research, and is only installed on workstations within the LOREnet laboratory.

1.5 Scope

The shaping of the spherical reflector is accomplished in this thesis by analyzing the reflector using geometrical analysis, ray-tracing, and plane wave analysis performed from optical diffraction methods. In addition, a sky study is performed for the spherical reflector to analyze the imposed steering limitations from the plane wave analysis. The sky study concludes the analysis of the spherical reflector. The design of a feeding structure for the spherical reflector is not addressed in this thesis.

The shaping for the sparse reflector has already been determined, but geometrical analysis is performed in order to define the sparse reflector for computer simulations. In addition, ray-tracing is performed as a proof of concept, and plane wave analysis is performed to obtain the FF radiation pattern for the sparse reflector. The results from these analyses are then compared to a 50 meter diameter circular shaped, parabolically contoured reflector stated previously as the baseline system. The baseline system calculation is completed using SatCom™ and includes the design of a horn antenna feed structure used in the analysis. Finally, a cross-shaped aperture antenna is proposed and explored as a possible optimal feeding structure for the sparse reflector. The analysis of this antenna is performed using a Finite-Difference (FD) approach to Eigenmode analysis to determine the modes

supported within this structure. The FF radiation patterns of the cross-shaped aperture are computed numerically from the dominate Transverse Magnetic (TM) and Transverse Electric (TE) modes respectively. These patterns are used to determine the suitability of using a cross-shaped aperture antenna as a feeding structure for the sparse reflector.

The physical implementation and experimental testing of these reflector antennas will not be performed. Also, the designs will not contain specific parts, manufacturers, or detailed mechanical drawings for implementing either antenna systems.

1.6 Overview

This thesis is organized as follows: Chapter 2 is a literature review of the published methods employed in this research; Chapter 3 presents the approach taken and the applications of the procedures from the literature review; Chapter 4 presents the results and analysis from the methodology; and Chapter 5 contains a summary, the conclusions from the analysis, and an explanation of future work. Chapter 2 is organized by analysis method as: GO, Vector Potential Solutions to Maxwell's Equations in the FF, The PO Approximation and Equivalence Theorems, 2-Dimensional Transverse Field Set Relationships, Reciprocity of Antenna FF Radiation Patterns, and an Overview of the MoM with the derivation of an Integral Equation. Chapters 3 - 5 are each organized similarly in the following manner: the geometrical analysis of each reflector antenna, the ray-tracing procedure applied to each reflector, the plane wave analysis applied to each reflector, the sky study for the spherical reflector, the baseline antenna design for the sparse reflector, and the feed design for the sparse reflector.

II. Background & Literature Review

This chapter presents theoretical concepts involved in the design of electrically large reflector antennas. Specifically, Geometric Optics (GO) (Section 2.1), solutions to Maxwell's equations in the Far-Field (FF) using vector potentials (Section 2.2), Equivalence principles using image theory, and the physical optics (PO) approximation (Section 2.3) will be developed [1] [2] [20] [21]. Solutions to Maxwell's equations for antenna designs often are not closed-form analytical solutions. Therefore, this chapter also describes the Method of Moments (MoM) for modeling and simulation of the antenna designs. The research presented in this chapter reviews the theory needed to design an electrically large reflector antenna system that provides the desirable directivity and efficiency for remote sensing and communications. Many publications written in the 1950s and 1960s focused on the design of reflector antenna systems [1] [7] [20]. The methods in these publications, along with methods in a collection of works from the 1990s and 2000s, are the basis for the theoretical concepts of this research [2] [21].

2.1 Geometric Optics (GO)

A simple preliminary step in the design of electrically large reflector antennas is to analyze the reflector geometry using ray optics which is used interchangeably with GO. Although this method is not relatively accurate, it is a fast method that can give insight into how a reflector will perform. GO assumes that the electric and magnetic fields can be divided into discrete rays which can then be propagated through a reflector system [1]. Also, GO assumes that the waves propagate through and around objects that are much greater in size than a wavelength [1]. Finally, GO assumes that all reflections at an interface follow Snell's law of Reflection [1]. If the surface of a reflector is a perfectly conducting surface, all incident energy will be reflected.

GO is developed in this section using a spherically contoured reflector example. The use of GO in the methodology will show the ray-tracing method applied to both a spherically contoured reflector and a parabolically contoured reflector. Also, note that the overbar notation used in this development signifies a line segment between two points.

An electrically large spherical reflector can be analyzed using GO. Figure 2.1 shows the cross-sectional geometry for a general spherical reflector under consideration.

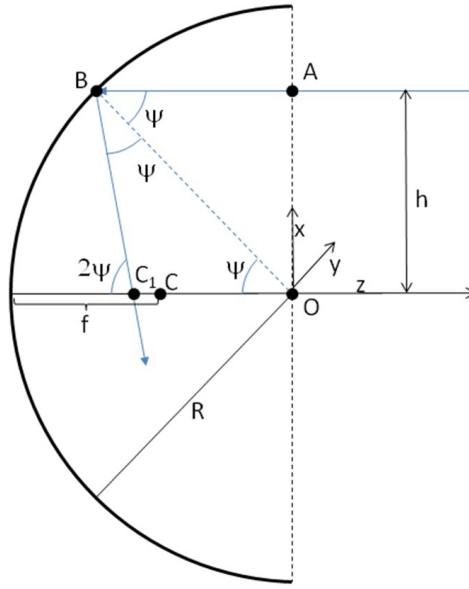


Figure 2.1: Spherical reflector geometry

The radius of curvature is denoted by R and is set equal to 1 for simplicity. The focus is labeled as C and its distance from the center of the reflector is f , where f is equal to half the radius of curvature. The distance f constitutes the paraxial focus where the z -axis is considered the paraxial [1]. For this analysis, a ray entering at point A is incident on the reflector at point B . A is a distance $h = \sin \psi$ from the z -axis. The ray is then reflected at B towards the paraxial. Snell's law of reflection states that the angle of incidence at a point measured with respect to the surface normal at that point is equal to the angle of reflection

measured opposite the angle of incidence. This is shown in Figure 2.1 where the angle of incidence is denoted by ψ and is equal to the angle of reflection. These angles are measured with respect to the surface normal at B shown as a dashed line. This ray then passes through a point C_1 on the paraxial some distance ΔC from the paraxial focus. The relationship of the angle ψ and the line segments $\overline{BC_1}$ and $\overline{OC_1}$ is determined by using the properties of the isosceles triangle (ΔOC_1B) [1]

$$\overline{BC_1} = \overline{OC_1} = \frac{1}{2} \sec \psi. \quad (2.1)$$

As seen in Figure 2.1, there is a deviation, ΔC , from C for larger angles. This distance can be calculated as:

$$\Delta C = \overline{CC_1} = \frac{1}{2} (\sec \psi - 1). \quad (2.2)$$

ΔC is known as the longitudinal spherical aberration, or focusing imperfection along the paraxial [1].

Further development of Figure 2.1 involves analyzing a tight bundle of rays that are incident on the reflector. This geometry is depicted in Figure 2.2. All parameters of the reflector are the same as shown in Figure 2.1 with the added illustration of a curve extending from C which is later described as a caustic surface.

The focusing of rays (energy) to multiple foci, or astigmatism, for this reflector is described using two steps. First, the tangential focal length, or the distance from a point B on the reflector to the point P tangent on the caustic surface, is calculated in Equation (2.3) with the approximations $dh/f_t = d(2\psi)$ and $dh/d\psi = \cos \psi$ [1]. Each of these differential distances is shown in Figure 2.2

$$f_t = \overline{BP} = f \cos \psi. \quad (2.3)$$

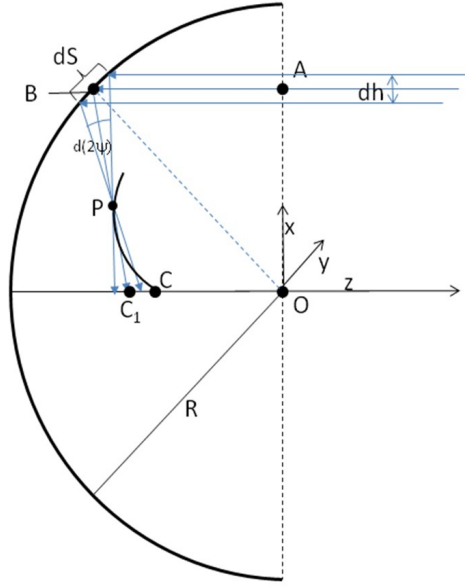


Figure 2.2: Spherical reflector geometry; Analyzing inherent aberrations

Then, the sagittal focal length, or the distance between point B and C_1 , is calculated in Equation (2.4) [1]

$$f_s = \overline{BC_1} = f \sec \psi. \quad (2.4)$$

The Astigmatism is then calculated as the difference between the sagittal and the tangential focal length [1]

$$\overline{PC_1} = f_s - f_t. \quad (2.5)$$

Finally, Figure 2.3 shows how the use of GO on a spherical reflector will result in a caustic surface. The caustic surface is a contour that is traced by the rays as they travel from the reflector towards the paraxial. Caustic surfaces occur frequently in optics problems and can be classified according to their shape. In the case of this spherical reflector, the caustic surface is a nephroid (kidney bean shape), which comes from the epicycloid classification of caustic surfaces [1].

harmonic phasor representation that assumes a linear, homogeneous, and isotropic medium. Each quantity is shown as dependent on frequency, indicating that it may be dispersive. The equations are given as:

$$\nabla \times \mathbf{E}(\mathbf{r}, \omega) = -z(\omega)\mathbf{H}(\mathbf{r}, \omega) - \mathcal{M}(\mathbf{r}, \omega) \quad (2.6)$$

$$\nabla \times \mathbf{H}(\mathbf{r}, \omega) = y(\omega)\mathbf{E}(\mathbf{r}, \omega) + \mathbf{J}(\mathbf{r}, \omega) \quad (2.7)$$

$$\nabla \cdot \mathbf{D}(\mathbf{r}, \omega) = q_e(\mathbf{r}, \omega) \quad (2.8)$$

$$\nabla \cdot \mathbf{B}(\mathbf{r}, \omega) = q_m(\mathbf{r}, \omega) \quad (2.9)$$

where

$$z(\omega) = \sigma_m(\omega) + j\omega\mu(\omega)$$

$$y(\omega) = \sigma_e(\omega) + j\omega\epsilon(\omega).$$

In Equations (2.6) - (2.9),

$$\mathbf{r} = (x, y, z),$$

\mathbf{E} and \mathbf{H} are the electric and magnetic fields,

\mathbf{J} and \mathcal{M} are the electric and magnetic current densities (sources),

$q_e(\mathbf{r}, \omega)$ and $q_m(\mathbf{r}, \omega)$ are the electric and magnetic charge densities,

\mathbf{B} and \mathbf{D} are the electric and magnetic displacement fields,

z and y are the intrinsic impedance and admittance of the media,

$\sigma_e(\omega)$ and $\sigma_m(\omega)$ are the electric and magnetic conductivities.

Again, each quantity is shown as dependent on angular frequency, $\omega = 2\pi f$, indicating that the medium may be dispersive.

The approach to solving these equations in this development involves the use of auxiliary functions known as vector potentials. Specifically, the resulting integrals from using the auxiliary functions will be manipulated to obtain concise mathematical representations that are well suited to the geometry of the antenna system. Electric sources only will be considered. However, the use of magnetic sources is the dual of the development that follows and will yield similar results based on the duality theorem [16]. Also, a deviation to the use of spherical coordinates will be shown for the integrations for spherically shaped sources such as the spherical reflector [21]. However, the use of Cartesian coordinates can be used by not performing the dyadic transforms shown later.

The first step in this approach to solving Equations (2.6) - (2.9) is to set $\mathcal{M} = 0$ and $q_m = 0$, which means that the fictitious magnetic sources have been turned off for this development. The next step is to multiply Equation (2.6) by μ . Here the dependencies on \mathbf{r} and ω are implied for shorthand notation [2] [21]

$$-\nabla \times \mu \mathbf{E} = \mu z \mathbf{H} = z \mathbf{B} \quad (2.10)$$

where

$$\mathbf{B} = \mu \mathbf{H} \quad \text{by Equation (2.9).}$$

Now, letting $\mathbf{B} \triangleq \nabla \times \mathbf{A}$, the $\nabla \cdot \mathbf{B} = 0$ because a purely circulating field has no divergence or $\nabla \cdot (\nabla \times \mathbf{A}) = 0, \forall \mathbf{A}$. Equation (2.10) can be written as [2] [21]

$$-\nabla \times \mu \mathbf{E} = z \nabla \times \mathbf{A} = \nabla \times z \mathbf{A}. \quad (2.11)$$

In Equation (2.11), bringing the intrinsic impedance, z , through the curl operator is valid because it has no spatial dependence. Rearranging Equation (2.11), it can be written as

$$\nabla \times (\mu \mathbf{E} + z \mathbf{A}) = 0. \quad (2.12)$$

Making the substitution that $-\nabla\Phi = \mu\mathbf{E} + z\mathbf{A}$, which implies that $\nabla \times (-\nabla\Phi) = 0$, Equation (2.12) can be rearranged into

$$\begin{aligned} -\nabla\Phi &= \mu\mathbf{E} + z\mathbf{A} \\ \Rightarrow \mu\mathbf{E} &= -z\mathbf{A} - \nabla\Phi \end{aligned} \quad (2.13)$$

Leaving this portion of the development temporarily, the next step is to multiply Equation (2.7) by μ [2] [21]

$$\mu\nabla \times \mathbf{H} = \nabla \times \mathbf{B} = y\mu\mathbf{E} + \mu\mathbf{J}. \quad (2.14)$$

Recalling that $\mathbf{B} \triangleq \nabla\mathbf{A}$, taking the curl of \mathbf{B} yields:

$$\nabla \times \mathbf{B} = \nabla \times \nabla \times \mathbf{A} = \nabla\nabla \cdot \mathbf{A} - \nabla^2\mathbf{A} \quad (2.15)$$

Equating Equations (2.13) - (2.14) with Equation (2.15), the result then becomes

$$\nabla\nabla \cdot \mathbf{A} - \nabla^2\mathbf{A} = -zy\mathbf{A} - y\nabla\Phi + \mu\mathbf{J}. \quad (2.16)$$

Equation (2.16) can be written as

$$\nabla(\nabla \cdot \mathbf{A} + y\Phi) = \left[\nabla^2 - \gamma^2 \right] \mathbf{A} + \mu\mathbf{J} \quad (2.17)$$

where $\gamma^2 = zy$ [2] [21].

Finally, letting $-y\Phi = \nabla \cdot \mathbf{A}$, known as the Lorentz Condition, the result may be obtained where by Equation (2.10), the magnetic vector potential, \mathbf{A} , can be obtained from a specified current density \mathbf{J} as in Equation (2.18) [2]

$$\left[\nabla^2 - \gamma^2 \right] \mathbf{A} = -\mu\mathbf{J}. \quad (2.18)$$

Further development is based on knowing a current density that resides on the surface of the antenna. The process for determining this will be discussed later in Section 2.3. However, for this development, the current density is expressed generally as a vector function using Cartesian vector components

$$\mathbf{J}_R(\mathbf{r}', \omega) = \hat{x}J_x + \hat{y}J_y + \hat{z}J_z. \quad (2.19)$$

Once the current density is specified in this form, it can be integrated over the surface of the reflector (denoted by the primed variables) for every observation point in the FF (denoted by the unprimed variables)

$$\mathcal{J}_R(\theta, \phi, \omega) = \int_{x'} \int_{y'} \int_{z'} \mathbf{J}_R(\mathbf{r}', \omega) e^{\gamma(\omega)x' \hat{x} \cdot \hat{r}(\theta, \phi)} e^{\gamma(\omega)y' \hat{y} \cdot \hat{r}(\theta, \phi)} e^{\gamma(\omega)z' \hat{z} \cdot \hat{r}(\theta, \phi)} dx' dy' dz' \quad (2.20)$$

$$\mathcal{J}_R(\theta, \phi, \omega) = \int_{|\mathbf{r}'|} \mathbf{J}_R(\mathbf{r}', \omega) e^{\gamma(\omega)\mathbf{r}' \cdot \hat{r}(\theta, \phi)} d\mathbf{r}'.$$

In Equation (2.20), $\hat{r}(\theta, \phi) = \hat{x} \sin \theta \cos \phi + \hat{y} \sin \theta \sin \phi + \hat{z} \cos \theta$ and also, the volume integral accounts for the skin depth of the current density that resides on the surface of the antenna.

The magnetic vector potential \mathbf{A} is then obtained by evaluating

$$\mathbf{A}_R(\mathbf{r}_S, \omega) = \mu(\omega)\psi(r, \omega)\mathcal{J}_R(\theta, \phi, \omega) \quad (2.21)$$

where ψ is the Free Space Green's Function (FSGF) given by:

$$\psi(r, \omega) = \frac{e^{-\gamma(\omega)r}}{4\pi r}. \quad (2.22)$$

The derivation of the FSGF is omitted in this thesis for brevity. Using the parallel ray approximation to simplify a solution to the time harmonic non-homogeneous vector wave

equation in Equation (2.18) can be done using the FSGF. The assumption that any vector from the surface of the antenna to some FF observation point is parallel to the corresponding vector measured from the source origin, to the observation point is known as the parallel ray approximation (see Figure 2.4) [2] [21]. It is important that the source origin is typically the same as the FF origin and can be chosen to simplify the analysis of a given antenna.

Note this solution for the vector potential assumes the removal of any object in space other than the source itself (i.e. only one continuous medium between the source and observer). The vector potential is a mathematical quantity that is used as an intermediate step to obtain the electric and magnetic FF patterns. It is a vector function that represents a directional pattern which varies over an imaginary sphere enclosing the antenna. Consequently, the electric and magnetic FF patterns vary in the same manner. Therefore, the vector potential is converted from rectangular unit vectors to spherical unit vectors of the FF. This conversion highlights the FF dependency on (θ, ϕ) .

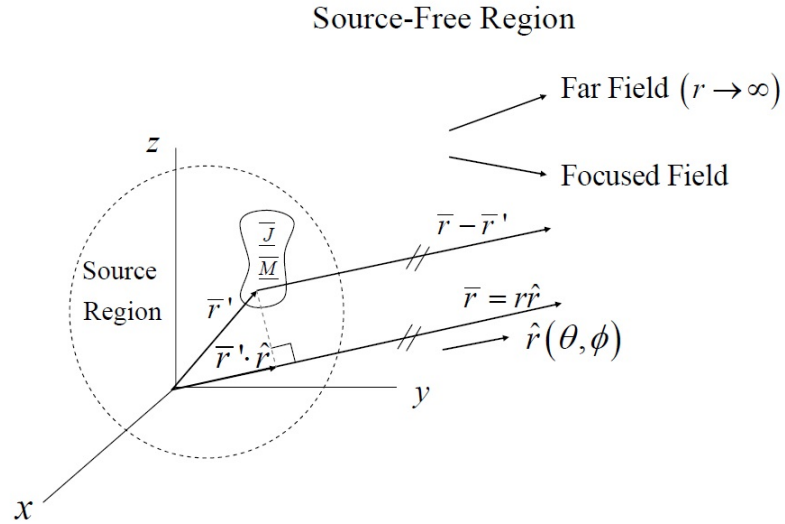


Figure 2.4: Illustration of the Parallel Ray Approximation

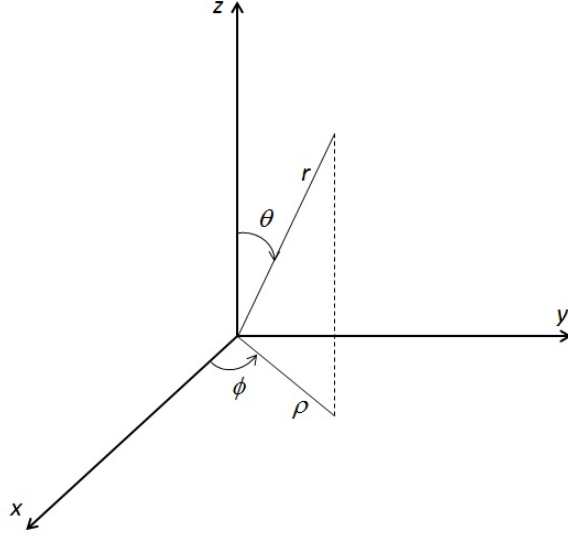


Figure 2.5: Spherical coordinate system

The conversion is performed using the dyadic transform

$$\overline{\mathbf{T}}_S^R = \begin{pmatrix} \sin \theta \cos \phi & \cos \theta \cos \phi & -\sin \phi \\ \sin \theta \sin \phi & \cos \theta \sin \phi & \cos \phi \\ \cos \theta & -\sin \theta & 0 \end{pmatrix}. \quad (2.23)$$

The spherical coordinate system utilized here has the following conventions:

\hat{r} is the unit vector oriented radially outward from the origin,

$\hat{\theta}$ is the unit vector oriented along the angle measured downward from the positive z -axis,

$\hat{\phi}$ is the unit vector oriented along the angle measured counter-clockwise from the positive x -axis (see Figure 2.5).

The dot product of this dyadic with the vector potential produces the vector potential in spherical vector components:

$$\mathbf{A}_S(\mathbf{r}_S, \omega) = \overline{\mathbf{T}}_S^R \cdot \mathbf{A}_R(\mathbf{r}_S, \omega). \quad (2.24)$$

Then the electric FF is calculated as:

$$\mathbf{E}_S(\mathbf{r}_S, \omega) = -\frac{z(\omega)}{y(\omega)} [\mathbf{A}_S(\mathbf{r}_S, \omega) - \hat{r}A_r]. \quad (2.25)$$

The radial component is omitted from the expression, denoted by the subtraction in Equation (2.25), at this point because the radial component of the electric FF is negligible due to the radiation condition [16].

Finally, from Equation (2.6), the magnetic FF is calculated as:

$$\mathbf{H}_S(\mathbf{r}_S, \omega) = \frac{1}{\eta(\omega)} \hat{r} \times \mathbf{E}_S(\mathbf{r}_S, \omega), \quad (2.26)$$

where $\eta(\omega)$ is the impedance of free space and is defined as:

$$\eta(\omega) = \sqrt{\frac{z(\omega)}{y(\omega)}}. \quad (2.27)$$

2.3 The Physical Optics (PO) Approximation and Equivalence Theorems

In the analysis of antennas, it is often convenient to use equivalence theorems to approximate the current density on the surface of the antenna. Equivalence theorems are focused on reducing a given geometry to a theoretical current radiating into free-space that sustains the same fields as the original source [2] [16] [22]. This theoretical current can be used in the radiation integral shown in Equation (2.20) to then calculate the vector potential and consequently the Electric and Magnetic FF radiation patterns. In the context of this

thesis, the surface equivalence theorem will be used and thus is described here along with the PO approximation.

2.3.1 The PO Approximation.

Electrically large structures, or structures that are much greater in size than a wavelength, pose a computational burden in numerical approximations of electromagnetic problems. In particular, if an electrically large structure such as a reflector antenna is a good conductor, the PO approximation may be used to solve for the current density on the surface. In general, a scattering problem has an expression such as:

$$\mathbf{J}_p = \hat{n} \times \mathbf{H} = \hat{n} \times (\mathbf{H}_1 + \mathbf{H}^s), \quad (2.28)$$

which describes the current density on the surface of scattering body. If this surface, however, is approximately flat and appears infinite in extent within a local region (i.e. electrically large), Equation (2.28) can be rewritten as:

$$\mathbf{J}_p = 2\hat{n} \times \mathbf{H}_1. \quad (2.29)$$

This is known as the PO approximation [16] [17]. It is valid based on how flat the structure is locally compared to a wavelength. Along the surface of the conductor, the scattered field component denoted by the superscripted s in Equation (2.28) is equal in amplitude and in phase with the incident field component denoted by the subscripted 1 in Equation (2.28).

2.3.2 Surface Equivalence Theorem and Image Theory.

The surface equivalence theorem starts with unknown current sources \mathbf{J} and \mathbf{M} sustaining known fields \mathbf{E} and \mathbf{H} . To obtain equivalent sources in terms of the known fields \mathbf{E} and \mathbf{H} , an imaginary surface can be carefully chosen to enclose the unknown sources \mathbf{J} and \mathbf{M} . The goal is then to determine the radiated fields outside of the surface. Therefore, it is critical to choose a surface such that the fields over the surface are known a

priori. Most often, the surface chosen corresponds closely to conducting parts of the antenna structure.

The equivalent sources can then be defined over the surface as:

$$\mathbf{J}_s = \hat{n} \times (\mathbf{H} - \mathbf{H}_1) \quad (2.30)$$

$$\mathbf{M}_s = -\hat{n} \times (\mathbf{E} - \mathbf{E}_1). \quad (2.31)$$

The subscript s here denotes that the current is over the imaginary surface. The subscript 1 on the additional fields shown in Equations (2.30) - (2.31) indicate that the fields are those within the volume enclosed by the imaginary surface.

These equivalent surface currents radiate out into unbounded space, where it is assumed the medium is the same everywhere, and sustain the unknown fields \mathbf{E} and \mathbf{H} outside of the surface. Because everywhere outside of the imaginary surface is the region of interest for field calculations, it is a valid approximation to assume that the fields within the imaginary surface are zero. This reduces Equations (2.30) - (2.31) to:

$$\mathbf{J}_s = \hat{n} \times \mathbf{H}_1 \quad (2.32)$$

$$\mathbf{M}_s = -\hat{n} \times \mathbf{E}_1. \quad (2.33)$$

Equations (2.32) - (2.33) are known as Love's Equivalence Principle [16] [19]. To validate the approximation made by the Love's Equivalence Principle, the surface will be replaced with either a Perfect Electric Conductor (PEC) or Perfect Magnetic Conductor (PMC) surface, based on the fields that reside on the surface. Having done this, image theory is required to obtain an equivalent current density radiating in unbounded space. Image theory is best described by studying Figure 2.6, where linear elements are imaged across a PEC and a PMC plane respectively. In order for image theory to be used, it must be assumed

that the PEC or PMC is on the order of several wavelengths, or electrically large. This assumption is approximating the original stipulation that image theory applies to a current radiating in the presence of an infinite PEC or PMC [2] [16].

Using the cases of either a tangential electric current in the presence of a PMC surface or a tangential magnetic current in the presence of a PEC surface, image theory is applied. This yields a single equivalent current source above a perfect conductor with twice the strength of the original source radiating into unbounded space. The imaginary surface is removed by Love's Equivalence Principle and image theory where the final equivalent current sources can be written more concisely as:

$$\mathbf{J}_s = 2\hat{n} \times \mathbf{H}_1 \quad (2.34)$$

$$\mathbf{M}_s = -2\hat{n} \times \mathbf{E}_1. \quad (2.35)$$

Figure 2.7 shows an illustration of applying Love's Equivalence Principle to a rectangular aperture surrounded by an infinite ground plane. The left hand picture shows the original problem with the two media, the known field components over the aperture, and the coordinate system convention. The right hand diagram shows the equivalent problem with the ground plane removed leaving only the equivalent sources radiating into free space. It is important to note that this particular application of Love's Equivalence Principle yields radiated field results that are valid only for $z > 0$ based on the original problem.

2.4 Two-Dimensional Transverse Magnetic (TM)^z and Transverse Electric (TE)^z Field Set Relations

In the previous section, a method for devising a problem that is equivalent to an aperture with known field components radiating in free space was developed. However, the method referred to relies on knowing the field components within a given aperture.

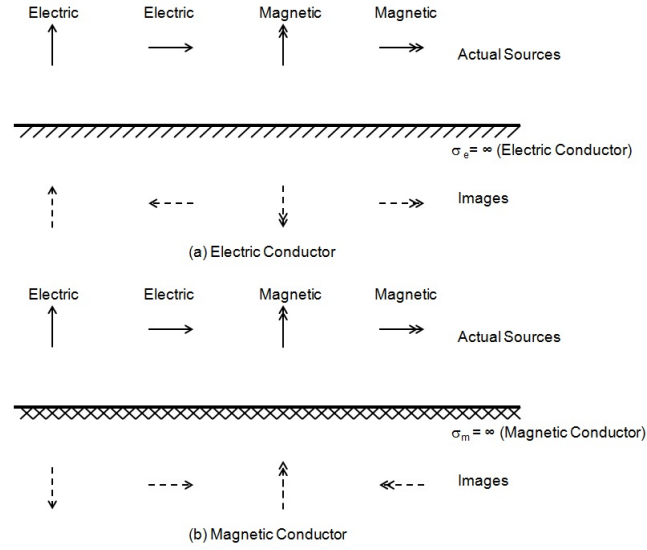


Figure 2.6: Illustration of Image Theory applied to linear elements above perfect conductors [2]

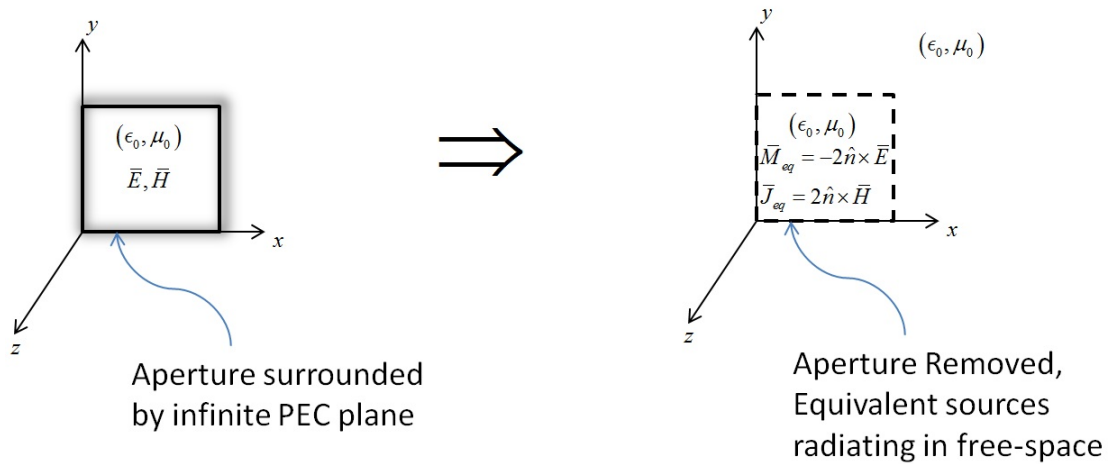


Figure 2.7: Illustration of a particular application of Love's Equivalence Principle to a rectangular aperture set in an infinite ground plane

Solving for the fields within an aperture is analogous to solving for the fields within the cross-section of a waveguide. Obtaining these field components can be accomplished using

a Finite-Difference (FD) approach to solving Maxwell's equations within a given aperture or waveguide cross-section.

Before being able to apply a FD approximation (shown later) to solving for the field components within a given aperture, Maxwell's equations must be simplified. Equations (2.6) and (2.7) shown previously are the form of Maxwell's equations that will be used. This form of Maxwell's equations, as stated previously, is the time harmonic phasor representation, which assume a linear, homogeneous, isotropic medium that may or may not be dispersive. Equations (2.6) and (2.7) are rewritten here for convenience

$$\nabla \times \mathbf{E}(\mathbf{r}, \omega) = -z(\omega)\mathbf{H}(\mathbf{r}, \omega) - \mathbf{M}(\mathbf{r}, \omega)$$

$$\nabla \times \mathbf{H}(\mathbf{r}, \omega) = y(\omega)\mathbf{E}(\mathbf{r}, \omega) + \mathbf{J}(\mathbf{r}, \omega).$$

In the previous development based on these two equations, a vector potential approach was used to simplify the mathematics. However, for this development, the fields will be approximated directly and several assumptions are made to further simplify the problem. First, the aperture is assumed to be source-free, meaning that the aperture is far enough away from the generating source allowing the sources to be neglected in the calculations. Second, ignoring loss in the aperture, the intrinsic parameters, $z(\omega)$ and $y(\omega)$, are equal to $j\omega\mu(\omega)$ and $j\omega\epsilon(\omega)$ respectively. Third, the problem is reduced from a 3-Dimensional problem to a 2-Dimensional problem because it is assumed, from the analogy of a waveguide problem, that the field components amplitude distributions within the aperture do not vary in the direction of propagation (i.e. propagation down a waveguide). Finally, it is assumed that there is no dispersion across the aperture, eliminating the dependency on frequency for the material parameters.

Given these assumptions, Equations (2.6) and (2.7) can be written as:

$$\nabla \times \mathbf{E}(\mathbf{r}) = -j\omega\mu\mathbf{H}(\mathbf{r}) \quad (2.36)$$

$$\nabla \times \mathbf{H}(\mathbf{r}) = j\omega\epsilon\mathbf{E}(\mathbf{r}). \quad (2.37)$$

To uncouple Equations (2.36) and (2.37) and arrange them in a more easily solved form, the curl of both sides of both equations is taken first

$$\nabla \times \nabla \times \mathbf{E}(\mathbf{r}) = -j\omega\mu\nabla \times \mathbf{H}(\mathbf{r}) \quad (2.38)$$

$$\nabla \times \nabla \times \mathbf{H}(\mathbf{r}) = j\omega\epsilon\nabla \times \mathbf{E}(\mathbf{r}). \quad (2.39)$$

From Equations (2.36) - (2.37), Equations (2.38) and (2.39) can be written as:

$$\nabla \times \nabla \times \mathbf{E}(\mathbf{r}) = -j\omega\mu(j\omega\epsilon\mathbf{E}(\mathbf{r})) = \omega^2\mu\epsilon\mathbf{E}(\mathbf{r}) = k^2\mathbf{E}(\mathbf{r}) \quad (2.40)$$

$$\nabla \times \nabla \times \mathbf{H}(\mathbf{r}) = j\omega\epsilon(-j\omega\mu\mathbf{H}(\mathbf{r})) = \omega^2\mu\epsilon\mathbf{H}(\mathbf{r}) = k^2\mathbf{H}(\mathbf{r}), \quad (2.41)$$

where k is referred to as the wave number and is expressed as $k^2 = \omega^2\mu\epsilon$.

To further simplify these expressions, the left hand sides of Equations (2.40) and (2.41) can be rewritten as:

$$\nabla \times \nabla \times \mathbf{E}(\mathbf{r}) = \nabla (\nabla \cdot \mathbf{E}(\mathbf{r})) - \nabla^2 \mathbf{E}(\mathbf{r}) \quad (2.42)$$

$$\nabla \times \nabla \times \mathbf{H}(\mathbf{r}) = \nabla (\nabla \cdot \mathbf{H}(\mathbf{r})) - \nabla^2 \mathbf{H}(\mathbf{r}). \quad (2.43)$$

It is important to note that under the assumption of a source-free aperture, $\nabla \cdot \mathbf{E}(\mathbf{r}) = 0$ and $\nabla \cdot \mathbf{H}(\mathbf{r}) = 0$ based on Equations (2.8) and (2.9):

$$\nabla \cdot \mathbf{E}(\mathbf{r}) = \frac{q_{ev}(\mathbf{r})}{\epsilon} = \frac{-\nabla \cdot \mathbf{J}(\mathbf{r})}{j\omega\epsilon} = 0 \quad (2.44)$$

$$\nabla \cdot \mathbf{H}(\mathbf{r}) = \frac{q_{mv}(\mathbf{r})}{\mu} = \frac{-\nabla \cdot \mathcal{M}(\mathbf{r})}{j\omega\mu} = 0. \quad (2.45)$$

Combining Equations (2.40) - (2.43), and the simplifications made in Equations (2.44) - (2.45), the resulting equations to be solved become:

$$\nabla^2 \mathbf{E}(\mathbf{r}) + k^2 \mathbf{E}(\mathbf{r}) = 0 \quad (2.46)$$

$$\nabla^2 \mathbf{H}(\mathbf{r}) + k^2 \mathbf{H}(\mathbf{r}) = 0. \quad (2.47)$$

Equations (2.46) and (2.47) are still 3-Dimensional, but as stated earlier, this particular problem can be reduced to a 2-Dimensional problem. In particular, Equations (2.46) and (2.47) can be rewritten in scalar form with only the longitudinal (assumed to be the z -direction) components of the fields:

$$(\nabla^2 + k_t^2) E_z = 0 \quad (2.48)$$

$$(\nabla^2 + k_t^2) H_z = 0. \quad (2.49)$$

Equation (2.48) can be referred to as the TM^z field set because the magnetic field resulting from solving this system will have no z -component. Similarly, Equation (2.49) can be referred to as the TE^z field set because the electric field resulting from solving this system will have no z -component. Note that the usage of the subscripted t indicates transverse direction, which in this case means x - and y -directions. In particular, $k_t^2 = k_x^2 + k_y^2$ where k_x and k_y are the x and y components of the overall wave number k .

Finally, to obtain a unique solution to either of these field sets, the aperture boundaries must be taken into account. As an example, which will be used later in this thesis, PEC boundaries can be used, which result in the following boundary conditions:

$$\text{TM}^z \quad E_z|_{\Gamma} = 0 \quad (2.50)$$

$$\text{TE}^z \quad \left. \frac{\partial H_z}{\partial n} \right|_{\Gamma} = 0 \quad (2.51)$$

where the evaluation at Γ means evaluation at the boundary. In Equation (2.51), the partial derivative with respect to n refers to the partial with respect to the normal direction, meaning it assumes the normal direction at any boundary.

Further development of these field set relations will be shown in the methodology section where the numerical approximations made to this problem will be detailed.

2.5 Reciprocity of Antenna FF Radiation Patterns

Reciprocity, as it applies to antenna FF radiation patterns, means that the FF radiation pattern of a particular antenna will be identical in either transmit or receive mode [2]. This property is valid under certain conditions, which include the medium of wave propagation and the materials used in the antenna system must be linear, a single distinct propagating mode feeds the antenna, and the antenna must be polarization matched to the probe antenna [2]. The probe antenna refers to an antenna used to either measure the transmitted signal from the antenna under test or to transmit a signal received by the antenna under test. The last condition is referring to the experimental determination of an antenna FF radiation pattern; but in a simulation, this condition will always be true. Much of the work within this thesis is hinged upon reciprocity to reduce the analysis of a given antenna system to only one mode (i.e. transmit or receive mode).

2.6 Overview of Method of Moments (MoM)

Discretizing a continuous geometry is the most common numerical approach to an approximate solution to Maxwell's equations for a given geometry. Dividing the geometry, such as the surface of a reflector antenna, into a finite number of discrete elements makes possible the application of a linear algebra approach to approximating the solutions to Maxwell's equations. Before discretizing a geometry, however, analytical manipulations of Maxwell's equations must occur to express them in a concise form known as an integral

equation. Integral equations are named as such because the unknown quantity is inside and possibly outside of an integral. One method of solving these types of equations involves using an approach referred to as the Finite Element Method (FEM) [18] [23]. The FEM discretizes a geometry into small pieces referred to as mesh cells and expands the unknown quantity into a series sum of basis functions, where the basis functions are chosen by the user. These approximations to the original integral equation result in a linear system that can be solved for a series of weights applied to the series sum of basis functions. To obtain a final solution for the unknown quantity, the weights are applied to the series of basis functions which are then summed together. It is important to note also that the FEM applies to electrically large and small geometries, but can result in impractically large linear systems for electrically large geometries, hence the motivation for Section 2.3.1. The approximations given in Section 2.3.1 do not require the use of a basis function expansion of the unknown current density and thereby simplifying the evaluation of the radiation integrals.

The MoM is a special case of the FEM [18]. However, the MoM can just be applied to surface integral equations and when it is, it can also be referred to as a Boundary Element Method (BEM). In general, the FEM is applied to volumetric problems dealing with the differential form of Maxwell's Equations. Both methods result in a linear system to be solved using matrix inversion or decomposition [18].

To illustrate how to apply the MoM, an integral equation is developed here. Previously, to avoid having to apply the MoM, the surface equivalence theorem coupled with image theory and Love's Equivalence Principle were applied in conjunction with the PO approximation in Section 2.3 to compute the surface current density from the known incident fields. Using the surface equivalence theorem coupled with image theory and Love's Equivalence Principle worked well for electrically large structures, but when the structure under test is not electrically large, the results will not be accurate [2] [17]. This

inaccuracy motivates the use of the MoM for better accuracy. The development of an integral equation follows.

This development starts with known incident fields \mathbf{E}^i and \mathbf{H}^i sustained by impressed current sources \mathbf{J}^i and \mathbf{M}^i . Maxwell's equations from Equations (2.6) and (2.7) rewritten for these quantities with the assumption that the medium is free-space, meaning that $\mathbf{z} = j\omega\mu_0$ and $\mathbf{y} = j\omega\epsilon_0$, are shown here as:

$$\nabla \times \mathbf{E}^i = -j\omega\mu_0\mathbf{H}^i - \mathbf{M}^i \quad (2.52)$$

$$\nabla \times \mathbf{H}^i = j\omega\epsilon_0\mathbf{E}^i + \mathbf{J}^i, \quad (2.53)$$

where the dependency on spatial coordinates (x, y, z) and frequency ω are assumed for the vector quantities.

The fields \mathbf{E}^i and \mathbf{H}^i can be assumed to be incident upon a scattering object of interest. In the case of this thesis, a reflector antenna is of interest. Using the surface equivalence principle, Equations (2.52) and (2.53) become:

$$\nabla \times \mathbf{E} = -j\omega\mu_0\mathbf{H} - \mathbf{M}^i \quad (2.54)$$

$$\nabla \times \mathbf{H} = j\omega\epsilon_0\mathbf{E} + \mathbf{J}^i, \quad (2.55)$$

where $\mathbf{E} = \mathbf{E}^i + \mathbf{E}^s$ and $\mathbf{H} = \mathbf{H}^i + \mathbf{H}^s$ respectively. The field quantities \mathbf{E}^s and \mathbf{H}^s are the scattered fields that are radiated by the equivalent current sources induced on the surface of the reflector by the incident fields \mathbf{E}^i and \mathbf{H}^i .

Substituting in $\mathbf{E} = \mathbf{E}^i + \mathbf{E}^s$ and $\mathbf{H} = \mathbf{H}^i + \mathbf{H}^s$ into Equations (2.54) and (2.55) and rearranging for the scattered fields, Maxwell's equations for the scattered fields become:

$$\nabla \times \mathbf{E}^s = -j\omega\mu\mathbf{H} + j\omega\mu_0\mathbf{H} - j\omega\mu_0\mathbf{H}^s \quad (2.56)$$

$$\nabla \times \mathbf{H}^s = j\omega\epsilon\mathbf{E} - j\omega\epsilon_0\mathbf{E} + j\omega\epsilon_0\mathbf{E}^s, \quad (2.57)$$

where μ_0 , ϵ_0 are the permeability and permittivity of free space and μ , ϵ are the permeability and permittivity associated with the reflector.

The scattered fields' dependence on \mathbf{E} and \mathbf{H} illustrate that the scattered fields are maintained by the incident fields. The incident fields induce a current on the surface of the reflector which maintains the scattered fields. Therefore, Equations (2.56) and (2.57) can be rewritten as:

$$\nabla \times \mathbf{E}^s = -\mathcal{M}^{eq} - j\omega\mu_0\mathbf{H}^s \quad (2.58)$$

$$\nabla \times \mathbf{H}^s = \mathbf{J}^{eq} + j\omega\epsilon_0\mathbf{E}^s, \quad (2.59)$$

where \mathcal{M}^{eq} and \mathbf{J}^{eq} are the induced currents on the surface of the reflector.

As shown in Section 2.2, it is mathematically simpler to solve for the unknown field quantity using vector potentials [2]. In the development presented in Section 2.2, the solution to Maxwell's equations using only the magnetic vector potential \mathbf{A} was presented. The solution using the electric vector potential \mathbf{F} is the dual of that particular development and therefore is omitted for brevity [2] [16]. However, the final expressions are presented as:

$$\mathbf{E}^s = \frac{1}{j\omega\epsilon_0\mu_0} \left[k_0^2 \mathbf{A}^s + \nabla(\nabla \cdot \mathbf{A}^s) \right] - \frac{\nabla \times \mathbf{F}^s}{\epsilon_0} \quad (2.60)$$

$$\mathbf{H}^s = \frac{\nabla \times \mathbf{A}^s}{\mu_0} + \frac{1}{j\omega\epsilon_0\mu_0} \left[k_0^2 \mathbf{F}^s + \nabla(\nabla \cdot \mathbf{F}^s) \right], \quad (2.61)$$

where the vector potentials \mathbf{A}^s and \mathbf{F}^s are calculated as:

$$\mathbf{A}^s(\mathbf{r}) = \int_S \mu_0 \mathbf{J}^{eq}(\mathbf{r}') G(\mathbf{r}|\mathbf{r}') dS' \quad (2.62)$$

$$\mathbf{F}^s(\mathbf{r}) = \int_S \epsilon_0 \mathcal{M}^{eq}(\mathbf{r}') G(\mathbf{r}|\mathbf{r}') dS'. \quad (2.63)$$

In Equations (2.62) and (2.63), the spatial dependency is noted due to the two different reference frames associated with this problem. The observation or observer reference frame is denoted by unprimed variables and the source reference frame is denoted by primed variables. Both reference frames share the same origin, but are independent of one another. Also, the $G(\mathbf{r}|\mathbf{r}')$ function is the generic representation for the Free Space Green's Function (FSGF) originally presented in Section 2.2 as $\psi(\mathbf{r}, \omega)$, but expressed here as:

$$G(\mathbf{r}|\mathbf{r}') = \frac{e^{-jkR}}{4\pi R}, \quad (2.64)$$

where $R = \sqrt{(x - x')^2 + (y - y')^2 + (z - z')^2}$. The difference here is that the FF approximation has not been made, meaning that the FSGF depends on both observer and source variables, which indicates that it cannot be split or moved outside the integral.

To obtain a unique solution to this problem, the boundary condition in Equation (2.65) is applied under the assumption that the reflector surface is a good conductor making it resemble a PEC (i.e. very high conductivity)

$$\hat{n} \times \mathbf{E}(\mathbf{r}) = 0 \quad \forall \quad \mathbf{r} \in \text{Reflector Surface} \quad (2.65)$$

$$\Rightarrow \hat{n} \times \mathbf{E}^s = -\hat{n} \times \mathbf{E}^i.$$

The integral equation for the scattered electric field, known as an Electric Field Integral Equation (EFIE), can be written as:

$$\hat{n} \times \frac{1}{j\omega\epsilon_0\mu_0} \left[k_0^2 + \nabla\nabla \cdot \right] \int_S \mu_0 \mathbf{J}^{eq}(\mathbf{r}') G(\mathbf{r}|\mathbf{r}') dS' = -\hat{n} \times \mathbf{E}^i. \quad (2.66)$$

Having developed a particular integral equation in Equation (2.66), the MoM can now be applied to solve for the unknown current density $\mathbf{J}^{eq}(\mathbf{r}')$. The first step is to choose a set of basis functions to use as an approximation to the unknown current density. For this

development, the basis functions will be left in a general form because the choice of basis functions are problem dependent [18]. Using this approximation for the unknown current density, the summation can be expanded or truncated to N number of terms. This is shown in Equation (2.67)

$$\mathbf{J}^{eq}(\mathbf{r}') \approx \sum_{n=1}^N a_n f_n(\mathbf{r}'). \quad (2.67)$$

Substituting Equation (2.67) into Equation (2.66) and exchanging the order of integration and summation, Equation (2.66) becomes:

$$\hat{n} \times \frac{1}{j\omega\epsilon_0\mu_0} [k_0^2 + \nabla\nabla\cdot] \mu_0 \sum_{n=1}^N a_n \int_S f_n(\mathbf{r}') G(\mathbf{r}|\mathbf{r}') dS' = -\hat{n} \times \mathbf{E}^i. \quad (2.68)$$

This step now has created N unknowns to solve for, $a_n \dots n = 1, 2, \dots, N$, and only one equation. In order to create the other equations to solve for the coefficients, a_n , a testing operation is presented. The choice of testing function is important to the problem type, but the most common testing function, the delta function, is presented here [18] [23]. The procedure of applying a testing operation at N points is the same as enforcing boundary conditions on the surface of the reflector:

$$\hat{n} \times \frac{1}{j\omega\epsilon_0\mu_0} [k_0^2 + \nabla\nabla\cdot] \mu_0 \int_{S_m} \left[\sum_{n=1}^N a_n \int_{S_n} f_n(\mathbf{r}') G(\mathbf{r}|\mathbf{r}') dS' \right] \delta(\mathbf{r}' - \mathbf{r}'_m) dS' = -\hat{n} \times \int_S \mathbf{E}^i(\mathbf{r}') \delta(\mathbf{r}' - \mathbf{r}'_m) dS', \quad (2.69)$$

which can be further simplified to:

$$\hat{n} \times \frac{1}{j\omega\epsilon_0\mu_0} [k_0^2 + \nabla\nabla\cdot] \mu_0 \sum_{n=1}^N a_n \int_{S_n} f_n(\mathbf{r}') G(\mathbf{r}|\mathbf{r}'_m - \mathbf{r}') dS' = -\hat{n} \times \mathbf{E}^i(\mathbf{r}'_m). \quad (2.70)$$

The expression shown in Equation (2.70) can be reformulated into a linear system $\overline{\mathbf{A}}\mathbf{x} = \mathbf{b}$ where:

$$\begin{aligned} A_{mn} &= \mu_0 f_n(\mathbf{r}') G(\mathbf{r}|\mathbf{r}'_m - \mathbf{r}') \\ x_n &= a_n \\ b_n &= E_u^i(\mathbf{r}'_m). \end{aligned} \tag{2.71}$$

It is important to note the subscript u on the known incident field indicates only one of the individual vector components of the current density. For the other dimensions, the same set of equations is used with the other vector components of the incident electric field.

The solution for the coefficients, a_n , follow from solving the linear system in Equation (2.71), which can then be used to approximate the current density on the surface of the reflector. The approximate current density can then be used to solve for the scattered fields everywhere surrounding the reflector and other antenna parameters such as the directivity, gain, beam widths, and front to back ratio.

The MoM will be used in this thesis by the commercial Computational Electromagnetics (CEM) codes. The general presentation of MoM here shows the basis of the commercial CEM codes, but each will apply different proprietary methods for solving the systems more efficiently.

III. Methodology

For this thesis, there are two particular reflector antenna designs of interest. The first is a rectangular shaped, spherically contoured reflector (spherical reflector) and the second is a cross-shaped, parabolically contoured reflector (sparse reflector). These reflectors are electrically large because the largest dimensions of each are on the order of hundreds to thousands of wavelengths. In addition, each reflector has a custom-shape. Each poses a technical challenge that can be analyzed using conventional methods with careful considerations given to the assumptions required by each method. The aim of this research is to use multiple methods to obtain an overall system design of each reflector antenna.

A presentation of the approach and methods that are used to generate the field data and corresponding results is given in this chapter. The approach taken for the design and analysis of each of the two reflector antennas in this thesis is similar except for special procedures that apply to the intended usage for each reflector. In particular, the spherical reflector includes a sky study to determine additional constraints on its geometry and the sparse reflector includes the design and analysis of a baseline antenna system for comparisons of the results. However, the other design procedures are similar for both reflector antennas and include:

1. Geometrical analysis, which includes determining the dimensions of each reflector and ray-tracing as a qualitative experiment to ensure the reflectors will perform as expected.
2. Plane wave analysis, which involves analyzing each reflector in its receiving mode with a plane wave incident on the surface. The results from this procedure are numerical results which include the directivity, the Far-Field (FF) radiation pattern (amplitude and phase), the beam width(s) (First Null Beam Width (FNBW) or Half

Power Beam Width (HPBW)), and the front to back ratio of the sparse reflector. This procedure will also produce results that give insight into designing a feeding structure for each reflector.

3. Feed antenna system design based on the Plane Wave Analysis results. This procedure is different for each reflector due to the differences in the Plane Wave Analysis results. Designing a feeding antenna system is not an exact procedure because it involves intuition to devise possible feed antenna systems. This intuitive insight is the creative aspect of antenna design which is a skill acquired only after gaining a thorough knowledge of Electromagnetics.
4. Feed antenna analysis to obtain the FF radiation pattern of the feeding antenna as the incident pattern on the reflector antenna. This procedure is performed only for the sparse reflector.

Many of the processes and procedures used in this chapter are presented generally in Chapter 2. Each method is valid for the design of a specific reflector antenna system. However, the methods produce results with differing accuracies and some methods produce unique results that are needed in the final design analysis. Applying the procedures in the order shown here is based on which procedures require results from other procedures. For instance, the feed design step requires input from the results of the plane wave analysis. Also, the order is based on increasing accuracy of results where the latter methods are more accurate than the former methods. Results of each procedure are unique according to the reflector antenna system.

3.1 Geometrical Analysis

This section presents the geometrical analysis of each reflector antenna. These reflectors are each a new concept in reflector antenna systems with several dimensional degrees of freedom. However, many dimensions of the reflector antennas have been provided by the

sponsoring group. These dimensions are used as design constraints to further analyze the dimensions that must be determined.

3.1.1 Rectangular Shaped, Spherically Contoured Reflector Geometry.

An illustration of the rectangular, spherically contoured reflector (spherical reflector) is shown in Figure 3.1. The length and width of the rectangular shape are the constrained dimensions. However, the radius of curvature for the reflector was not specified and thus constitutes a degree of freedom in the design procedure. In order to apply the ray-tracing procedure for this reflector, the relationship between the given dimensions and the variable dimension is first determined.

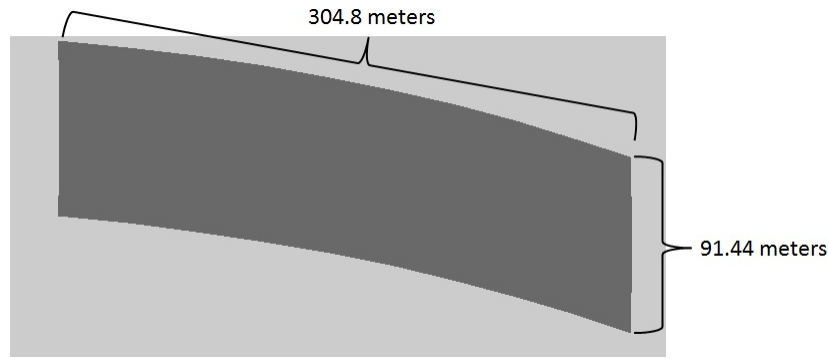


Figure 3.1: Geometry illustration for the spherical reflector

Given that the dimensions shown in Figure 3.1 are analogous to the chord length of a circle illustrated in Figure 3.2, the formula for the length of a chord is used and is given as:

$$\text{Chord Length} = l = r \text{ crd} \theta = 2r \sin \frac{\theta}{2}, \quad (3.1)$$

where the radius of curvature r and the angle θ are both unknowns and the chord length corresponds to either of the dimensions given in Figure 3.1. To use Equation (3.1), one of the two unknown quantities needs to be specified. Given that the radius of curvature, r , is a

degree of freedom, it is used as the specified variable while allowing θ to vary according to r . Therefore, rearranging Equation (3.1) for θ gives the expression:

$$\theta = \sin^{-1}\left(\frac{l}{2r}\right). \quad (3.2)$$

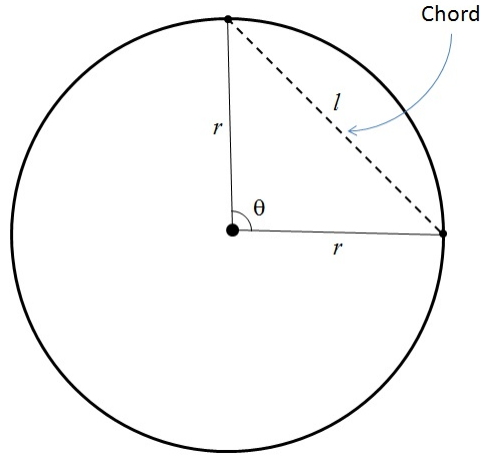


Figure 3.2: A chord of a circle

Equation (3.2) is then used in the geometry discretization for the spherical reflector to perform ray-tracing. The ray-tracing procedure is described in Section 3.1.2 and the corresponding results are presented in Section 4.1.1. Also, the surface area calculations and the comparison of dimensions to wavelengths are presented in Section 4.1.

3.1.2 Ray-Tracing Procedure: Rectangular Shaped, Spherically Contoured Reflector.

The ray-tracing procedure is a simple method for determining the qualitative performance of a reflector system. It is a method that is based on the same assumptions as Geometric Optics (GO) in that all incident waves are treated like discrete rays that travel in a straight path until they encounter a boundary between surfaces. Transmission through boundaries between surfaces take into account the refractive index difference between the

two media causing a bending of the path the energy follows. However, it is assumed that the surface of the spherical reflector is a Perfect Electric Conductor (PEC), meaning that all incident energy is reflected. Reflections are then handled using Snell's law as described in Section 2.1 which states that the angle of incidence upon a surface measured from the surface normal at that point is equal and opposite to the angle of reflection measured also from the surface normal at the point of incidence.

The ray-tracing procedure is implemented for the spherical reflector using MATLAB®. The user inputs to the code include the width and height of the rectangular shaped reflector, the radius of curvature, and the number of incident rays to simulate for each 2-Dimensional cross-section. From these inputs, the code generates three figures: the geometry as shown in Figure 3.1, a 2-Dimensional cross-section of the spherical reflector with incident and reflected rays, and a 3-Dimensional rendition of the spherical reflector with incident and reflected rays. The `surf()` command is used to plot the reflector from a meshed grid based on the user inputs. The `quiver()` and `quiver3()` functions are used to plot each ray for the 2-Dimensional and 3-Dimensional cases respectively. The inputs to each function include the beginning point of each ray and the vector components of each ray.

Calculating the surface normals involves using the spherical to Cartesian coordinates transform equations given as:

$$\begin{aligned} X &= R \sin \theta \cos \phi \\ Y &= R \sin \theta \sin \phi \\ Z &= R \cos \theta, \end{aligned} \tag{3.3}$$

where R is the radius of curvature, θ is the angle measured with respect to the z -axis, and ϕ is the angle measured in the xy -plane counter-clockwise from the x -axis. The coordinate convention is shown in Figure 2.5 where the origin is considered as the center point for the radius of curvature of the spherical reflector (see Figure 3.5). Calculating the reflected rays is performed by projecting the incident rays onto their corresponding surface normal and

subtracting twice the projection from the incident vector. This vector method of Snell's law avoids the use of programming loops, but the reflected rays are plotted using a programming loop. The resulting plots from this method are shown in Section 4.1.1 with the discussion. Also, the code for performing the ray-tracing is given in Section A.1

3.1.3 Cross-shaped, Parabolically Contoured Reflector Geometry.

The cross-shaped, parabolically contoured reflector (sparse reflector) concept was proposed as a folding antenna concept for a more deployable high directivity antenna system. The geometry was developed as a structurally feasible concept, but with unknown electrical performance. To analyze the electrical performance of this reflector, again the geometrical analysis is the first step.

Figure 3.3 shows the conceptual drawing of the sparse reflector. The dimensions are not variable, thereby reducing the number of design iterations in the early phases of analysis. The only dimension not shown in Figure 3.3 is the focal length, which was specified as $f = 80\text{m}$. Unlike the spherical reflector, the sparse reflector focuses incident energy to a single point referred to as the focal point because of the parabolic contour. There are no inherent aberrations, meaning that all energy received at the focal point will be in phase causing little to no signal strength loss on receive.

The illustration in Figure 3.3 shows only a cross-sectional view of the cross-shape formed by this reflector. A side-looking view shown in Figure 3.4 illustrates the parabolic contour that the sparse reflector has. The sparse reflector is a cross-shaped cutout from a paraboloid with a focal distance of 80m, resulting in a shallow curved shape.

Given all the dimensions for the sparse reflector, the parabolic contour associated with this reflector is calculated as:

$$x = \left(\frac{1}{4f} \right) y^2 \quad (3.4)$$

$$z = \left(\frac{1}{4f} \right) (x^2 + y^2). \quad (3.5)$$

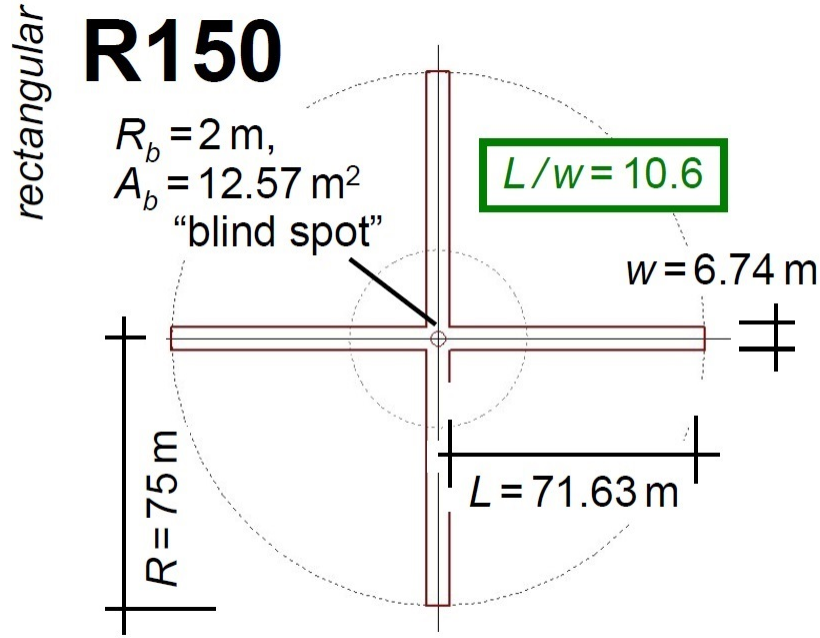


Figure 3.3: Conceptual drawing of the sparse reflector

To then discretize the geometry for the ray-tracing procedure, the x and y coordinates are sampled every 0.1 meters and the limits are determined from the sparse reflector diameter as $\pm 75 \text{ m}$. Equations (3.4) and (3.5) are used with the discrete values of y to solve for x and discrete values of x and y to solve for z respectively. MATLAB[®] is used to generate the plots shown in Figures 3.3 and 3.4. Finally, the surface area calculations and the comparison of dimensions to wavelengths are presented in Section 4.1.

3.1.4 Ray-Tracing Procedure: Cross-shaped, Parabolically Contoured Reflector.

The ray-tracing procedure is implemented for the sparse reflector using MATLAB[®]. However, in this case, the user inputs are the diameter, arm width, and arm length shown in Figure 3.3; the focal length; and the number of incident rays for any 2-Dimensional section of the reflector. From these inputs, the code generates 2-Dimensional and 3-Dimensional plots of the reflector with incident, normal, and reflected rays. The same MATLAB[®] functions mentioned in Section 3.1.2 are used to perform the plotting.

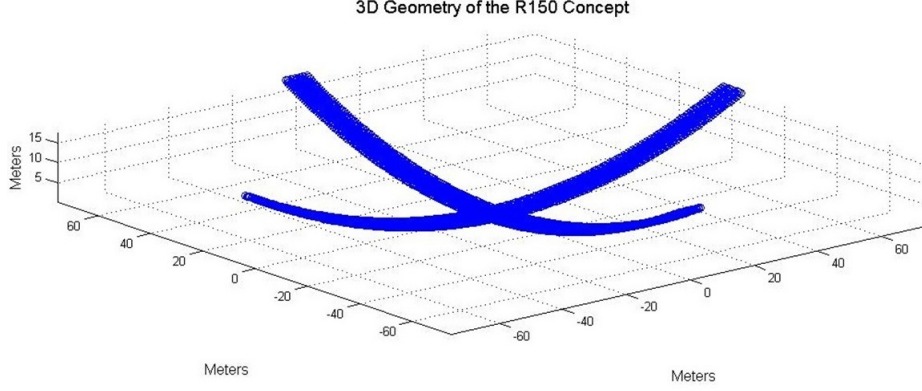


Figure 3.4: Side-looking view of the sparse reflector

In contrast to the ray-tracing code for the spherical reflector, the surface normals and reflected rays are calculated differently because of the parabolic contour. In the case of the spherical reflector, the surface normals are rays that converge at the center of the sphere describing the spherical contour of the reflector. For the sparse reflector geometry, the surface normals are calculated by defining a line tangent to the reflector at each point of incidence and rotating it by $\pi/2$, about the proper axis according to the local coordinate frame. The tangent line is created by drawing a line between two points: the point of incidence and a second point which is calculated by computing the derivative of the parabolic function and evaluating it at a point different from the point of incidence.

Another contrasting method in performing ray-tracing for the sparse reflector is calculating the reflected rays. The angle between each incident ray, \mathbf{I} , and its corresponding surface normal, \mathbf{N} , is computed by rearranging the dot product of each incident and normal vector. This rearrangement is given as:

$$\theta = \pi - \cos^{-1} \left(\frac{\mathbf{I} \cdot \mathbf{N}}{|\mathbf{I}| |\mathbf{N}|} \right). \quad (3.6)$$

The reflected ray is then constructed by rotating the normal vector about an axis tangent to the reflector by the angle θ using the following vector rotation matrix:

$$\begin{bmatrix} \cos \theta & 0 & -\sin \theta \\ 0 & 1 & 0 \\ \sin \theta & 0 & \cos \theta \end{bmatrix}. \quad (3.7)$$

See Section 4.1.2 for the resulting plots and discussion of the ray-tracing procedure for the sparse reflector. Finally, see Section A.2 for the code developed to perform the ray-tracing procedure for the sparse reflector.

3.2 Plane Wave Analysis

To further determine the performance of each reflector antenna, plane wave analysis is performed on each reflector. The plane wave analyses in this research are basic and do not include an angular spectrum or le-space analysis. Optical methods are used for the spherical reflector because they reduce the complexity of analysis by making special approximations. These approximations include:

1. The surface area is assumed to be much greater than the edge surface area for the reflector assuming a 10λ wide ring around each reflector [14].
2. The reflector is much larger than a wavelength (L-Band) [14].
3. The reflector is symmetric about the optical axis (axis extending from the center of the reflector) [14].
4. The radius of curvature for the spherical reflector and the focal length for the sparse reflector is large in comparison to a wavelength [14].
5. The incident waves are planar or their deviation from planar is less than $1/4$ of a wavelength [14].

It is shown in Table 4.1 that these approximations are applicable to both reflectors discussed in this thesis. Therefore, plane wave analysis using optical methods is a valid approach to determining the performance of each reflector. However, optical methods are

only used for the spherical reflector. For both reflectors, the assumed acceptable phase ripple is not determined and is not addressed in this research.

Plane wave analysis is a method of analyzing the fields scattered from an object with a plane wave incident upon its surface. A plane wave is an electromagnetic field with a source far enough away (Far-Field (FF)) such that its wavefront is planar meaning all the energy across the plane is equal in amplitude and phase [3] [6] [14] [16]. For the reflectors discussed in this thesis, plane wave analysis can be understood as receiving mode, which by reciprocity, will yield the same results as if the antenna system were in transmitting mode. Each reflector is analyzed differently due to its different cross-section shape and contour. The following subsections address each reflector and the specific plane wave analysis method employed.

3.2.1 Rectangular Shaped, Spherically Contoured Reflector.

From the theory and shown from the ray-tracing procedure performed in Section 3.1.2, the spherical reflector has inherent focusing errors known as spherical aberrations. These errors will cause a phase progression at the paraxial focus point from the energy spreading. This phase progression causes destructive interference which decreases the received signal strength, and if the signal phase is encoded with a message, that message will be lost. Therefore, it is vital that these aberrations be corrected at the paraxial focal point. To obtain a quantitative description of the aberrations, the reflector is analyzed in receive mode with a plane wave incident upon the surface.

Equation (3.8) describes a plane wave propagating through free-space

$$\mathbf{E}_i = \hat{x}E_0e^{-jk_0z}. \quad (3.8)$$

The coordinate convention used in this section is shown in Figure 3.5. In Equation (3.8), the subscript i indicates incident wave, E_0 is an arbitrary amplitude, the negative argument for the exponential term indicates a positive traveling wave, and k_0 is the free-space wave

number equal to $\frac{2\pi}{\lambda}$. For this analysis, the frequency is within the L-Band. This plane wave is then incident upon the surface of the reflector and the reflections are directed toward the paraxial focus. To visualize the aberrations at the paraxial focus, an image plane was placed there to capture the reflected energy. To calculate the amplitude and phase of the reflected energy, two optical methods were used: Fourier Analysis and Fresnel-Kirchoff Diffraction Integral (FKDI) analysis.

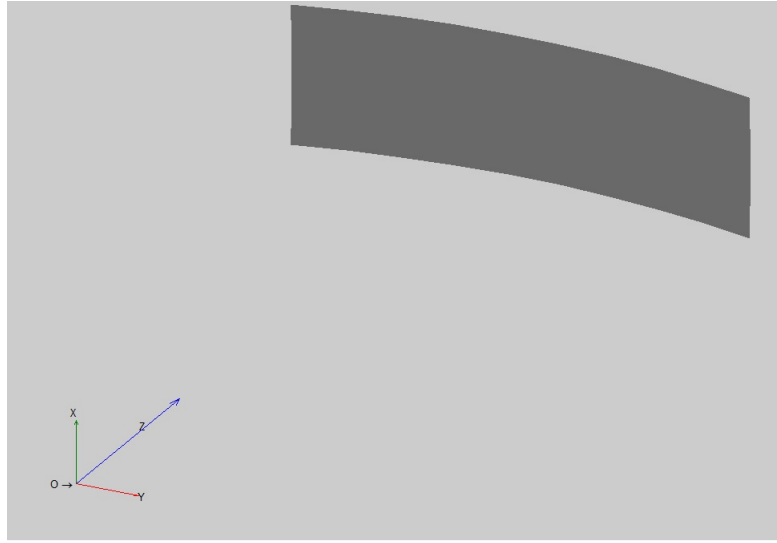


Figure 3.5: Coordinate convention used for Plane Wave Analysis of the rectangular shaped, spherically contoured reflector

Using Fourier analysis, the amplitude distribution on the image plane where the reflected energy is incident is the Fourier transform of the aperture equivalent current sources. These sources are related to the tangential field components on the reflector surface [14] [24]. The plane wave incident upon the already discretized reflector surface yields a discrete representation of the energy on the reflector. More specifically, it is a representation of the same plane wave, with an added phase progression, due to the curvature of the reflector. A Discrete Fourier Transform (DFT) calculates the amplitude distribution in the

image plane. Section 4.2.1 shows the resulting image planes with on and off axis plane waves incident.

FKDI analysis is a similar method to the Fourier analysis method, but differs in that it accounts for the known aberrations and allows for further off-axis calculations [14]. Equation (3.9) describes the FKDI method [14] [24]

$$U(x, y) = \frac{E_0}{j\lambda} \iint_S \frac{e^{jk(r_i - r_r)}}{r_i r_r} \left[\frac{\cos^{-1}(\mathbf{n}(x, y) \cdot \mathbf{r}_r(x, y)) - \cos^{-1}(\mathbf{n}(x, y) \cdot \mathbf{r}_i(x, y))}{2} \right] dS. \quad (3.9)$$

As can be seen, Equation (3.9) resembles a 2-Dimensional Fourier Transform with a different Kernel function. The integration is performed over the surface of the reflector, S , and the function $U(x, y)$ is the resulting image. Also, the cosine terms shown represent a projection of the second vector in the argument projected onto the first. Finally, the vector \mathbf{r}_i is the incident ray, the vector \mathbf{r}_r is the reflected ray, and the vector \mathbf{n} is the surface normal at the point of incidence. See Figure 3.6 for an example of a single incident ray, reflected ray, and surface normal.

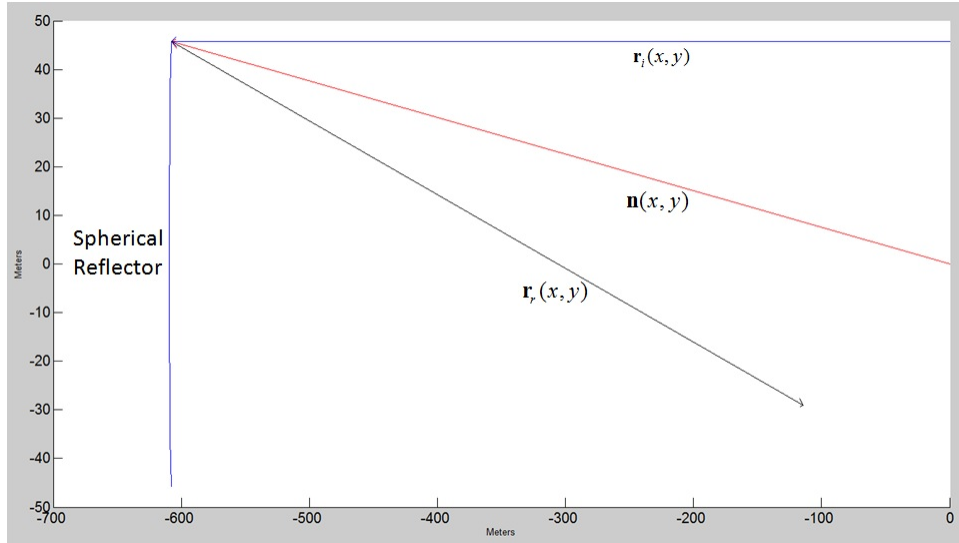


Figure 3.6: Illustration of vectors used in performing the FKDI computations

The FKDI proves to be a more useful method for calculating the image of reflected energy because non-uniform grids, 3-Dimensional grids, and off-axis angles of incidence can be used [14] [24]. In this research, off-axis results are generated to visualize the aberrations that the feeding structure must correct.

Implementing the FKDI is approximated by replacing the integral with a summation. This is shown in Equation (3.10) [24]. The index n indicates that the reflector surface is divided into N discrete parts

$$U(x, y) \approx \frac{E_0}{j\lambda} \sum_{n=1}^N \frac{e^{jk_n(r_{in}+r_{rn})}}{r_{in}r_{rn}} \left[\frac{\cos^{-1}(\mathbf{n}_n(x, y) \cdot \mathbf{r}_{rn}(x, y)) - \cos^{-1}(\mathbf{n}_n(x, y) \cdot \mathbf{r}_{in}(x, y))}{2} \right] \Delta S. \quad (3.10)$$

The results of using the FKDI are presented in Section 4.2.1 where both on-axis and off-axis images are shown. Also presented is a discussion about the steering capabilities of the reflector system by moving the feeding structure.

3.2.2 Cross-shaped, Parabolically Contoured Reflector.

The cross-shaped, parabolically contoured reflector (sparse reflector) antenna does not have aberrations as the spherical reflector does. As stated earlier, a parabolically contoured reflector focuses incident energy to a single point. The placement of a feeding structure for a parabolically contoured reflector is often at the focal point. This is the case for the sparse reflector. In contrast to the spherical reflector, feed placement is not an issue. However, there is still a need to determine the radiation characteristics of the sparse reflector because of its custom-shaped cross-section. Therefore, a different method of performing plane wave analysis is used for the sparse reflector.

SATCOM™, a Computational Electromagnetics (CEM) software package developed by The Ohio State University Electro-Science Laboratory, is the software chosen to perform the plane wave analysis of the sparse reflector. SATCOM™ requires that an antenna system have a feed specified because the analysis is always performed using the transmit mode of

the antenna. Because the feed placement is already known for the sparse reflector, a feeding structure that is capable of providing a uniform illumination of the sparse reflector is needed. Therefore, as opposed to the previous plane wave analysis on the spherical reflector, the sparse reflector is analyzed using the transmit mode. Providing that the sparse reflector is in the Far-Field (FF) region of the feeding structure and the FF radiation pattern of the feeding structure nearly provides uniform illumination of the sparse reflector, it is analogous to an incoming plane wave incident upon the sparse reflector. Therefore, a feeding pattern is devised to meet these criteria.

Following an example found in [4], the needed FF radiation pattern for a feeding structure to uniformly illuminate a reflector antenna is given as:

$$U(\theta, \phi) = A_0 \cos^{42} \left(\frac{\theta}{2} \right). \quad (3.11)$$

The independence with respect to ϕ shows that this FF radiation pattern is ϕ invariant, however in general, a FF radiation pattern depends on θ and ϕ . In order to verify this result, this radiation pattern is plotted using MATLAB®. Figure 3.7 shows that this FF radiation pattern illustrates an isotropic distribution of energy and given that the sparse reflector is in the FF region with respect to the feed point, the incident energy upon the reflector is nearly planar.

Two simulations, as opposed to one, are needed because the software cannot simulate the sparse reflector cross-shape directly. Rather, the reflector is segmented into two rectangular shaped, parabolically contoured reflectors which correspond to the horizontal and vertical sets of arms respectively. The SATCOM™ feed design wizard is used to define the FF pattern using Equation (3.11). After defining the input feed pattern, the simulation is run in two segments using the same polarization (left-hand circular) and frequency (1.5

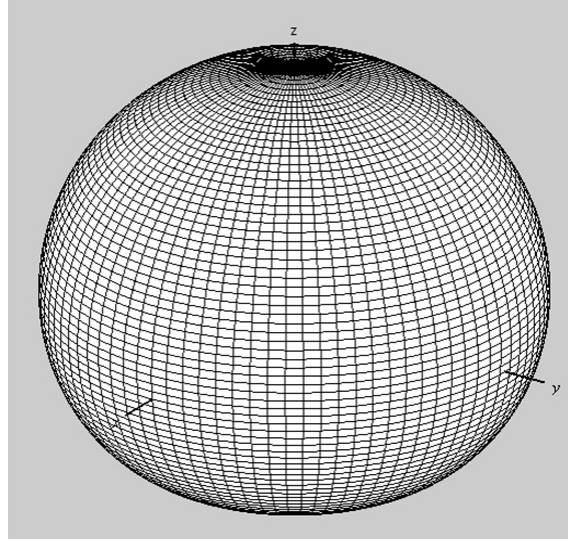


Figure 3.7: Plot of the FF radiation pattern used as a plane wave source in plane wave analysis for the sparse reflector

GHz) for each one. This is to ensure a similar field orientation is incident upon the reflector in both simulations.

The outputs of the two simulations are combined by first exporting the data to a text file format readable by MATLAB®. A script is then used to import the data to MATLAB® and perform pattern addition, also referred to as a coherent summation. In particular, the two patterns are summed together on a term by term basis to plot the overall resulting FF radiation pattern of the sparse reflector. Section 4.2.2 presents the results from the plane wave analysis simulations for the sparse reflector and Section A.4 presents the pattern addition code.

3.3 Sky Study for the Rectangular Shaped, Spherically Contoured Reflector

A necessary procedure for designing and analyzing the rectangular shaped, spherically contoured reflector (spherical reflector) is a study of to what region(s) in the sky the antenna will need to steer. This study has been labeled as a sky study. As mentioned previously, the design is expected to be used with Geosynchronous (GEO) satellites. The possible

locations for the antenna system were also expected to be within the Continental United States (CONUS) which led to the assumption that all GEO satellites over the CONUS were of interest. Under this assumption, the sky study is accomplished in several steps. The first is to contact sources at the Air Force Institute of Technology (AFIT) that have experience in tracking satellites, plotting satellite trajectories, and calculating plots of azimuth-elevation-range data. The second is to gather the satellite orbit data. The third is analyzing the data and performing the calculations of the azimuth-elevation-range data. Finally, the fourth is to draw conclusions based on the data to better constrain the steering needs of the spherical reflector antenna.

The AFIT Department of Aeronautical and Astronautical Engineering Satellite Tracking Group proved most helpful by referring us to a free, publicly available data source for satellite trajectory information. The source is a web site that provides the satellite trajectory information for nearly all satellites in GEO, Low Earth Orbit (LEO), and Medium Earth Orbit (MEO) using the universal Two Line Element (TLE) format [25]. The source is known as www.space-track.org. In order to gain access to the data, an individual must have a justification and an association with either a government, academic, or industrial institution. Registering for the web site was accomplished under the need to gather data for research at AFIT.

Gathering the TLE data is a matter of downloading a compressed zip file that contains all the GEO satellite data within text files. The data is updated twice daily. This is necessary because the satellite orbits vary slightly throughout the year. The variation in orbit causes what is known as an analemma to be traced by the satellite throughout the course of a year. An example is shown in Figure 3.8. Because the CONUS is above the Equator, it is important to consider that the analemma shape will be elongated because of the downward looking angle on GEO satellite belt which is directly above the Equator. This elongation

prompts yet another important question: What are the steering limitations in elevation? The sky study also answers this question.



Figure 3.8: Illustration of an analemma pattern traced out by a GEO satellite over the course of one year. This is only a specific example and does not account for all GEO satellites

To analyze the data, the TLE format first has to be explored. An example of the TLE data associated with the international space station for a specific day is shown in Figure 3.9. As described in [25], the data is arranged with the first line, referred to as line 0, containing the common name of the object that is found in the satellite catalog (columns 01-24). The second line, line 1, has a line number (column 01), the satellite catalog number (columns 03-07), the Elset classification (column 08), the international designator (columns 10-17), the element set epoch or Coordinated Universal Time (UTC) (columns 19-32), the first derivative of the mean motion with respect to time (columns 34-43), the second derivative of the mean motion with respect to time (columns 45-52), the B* drag term which estimates the atmospheric effects on the satellite motion (columns 54-61), the element set type (column

63), the element number (columns 65-68), and a checksum (column 69). Finally, the third line, line 2, has a line number (column 01), the satellite catalog number (columns 03-07), the orbit inclination in degrees (columns 09-16), the right ascension of ascending node in degrees (columns 18-25), the eccentricity (columns 27-33), the argument of perigee in degrees (columns 35-42), the mean anomaly in degrees (columns 44-51), the mean motion in revolutions per day (columns 53-63), the revolution number at epoch (columns 64-68), and a checksum (column 69).

```
ISS (ZARYA)
1 25544U 98067A 08264.51782528 -.00002182 00000-0 -11606-4 0 2927
2 25544 51.6416 247.4627 0006703 130.5360 325.0288 15.72125391563537
```

Figure 3.9: TLE example for the international space station

Plotting satellite tracks from the TLE data directly is outside of the scope of this thesis. Therefore, performing the necessary calculations on the TLE data is accomplished using a commercially available software known as Systems Tool Kit (STK) by Analytical Graphics Inc. (AGI). This particular software package has the capability to import TLE data for plotting the azimuth-elevation-range of a satellite. The text files that contain the TLE data from all GEO satellites are imported to calculate and visualize an estimate of the trajectories of all GEO satellites over the CONUS. The results are used to further refine the steering capabilities of the spherical reflector. The plots and discussion from the sky study can be found in Section 4.3.

3.4 Baseline Calculation for the Cross-shaped, Parabolically Contoured Reflector

A necessary procedure in designing and analyzing the cross-shaped, parabolically contoured reflector (sparse reflector) antenna is designing and analyzing a baseline antenna system to compare the performance of the sparse reflector. In particular, the goal is to explore how well the sparse reflector performs against a 50 meter diameter circular shaped,

parabolically contoured reflector, which has approximately the same surface area. The circular shaped reflector is referred to as the “filled” reflector because it has a smooth, continuous cross-section as opposed to the sparse reflector, which has a jagged, discontinuous cross-section.

The approach to performing the baseline calculation is to first search for existing antenna systems that are similar to the filled reflector. The search led to the large reflector antennas of the DSN built and maintained by the National Aeronautics and Space Administration (NASA). The design methodology and examples of the antenna systems are published in [4]. A chapter within this resource explains the specific design of one of the first NASA DSN reflector antennas which has been decommissioned. This antenna was known as the Deep Space Station 11: Pioneer [4]. It was the first large DSN Cassegrain antenna and was designed to operate in L-band, which is the frequency band of interest for the sparse reflector. The only differences between the DSN Station 11 and the filled aperture for this thesis are the dimensions and feeding antenna. However, in order to minimize design time and the number of design iterations for the baseline calculation, the DSN Station 11 is used as the basis for the filled aperture. In particular, the proportion of the secondary reflector diameter to the primary reflector diameter from the DSN Station 11 is used, but the dimensions are scaled up to the required 50 meters. The resulting dimensions are shown in Table 3.1. Note that the f/d ratio shown is the same as the sparse reflector.

With the geometry for the filled aperture in place, a feeding antenna is designed to operate the filled aperture in L-Band. A standard choice for feeding a filled aperture is a horn antenna [2] [6] [8]. In particular, for simplicity, a pyramidal horn is designed following the design methodology for a pyramidal horn in chapter 13 of [2] and is shown in Figure 3.10. The design method in use requires a desired gain to be specified, then the specified gain is related to the width and height of the horn antenna. Finally from the width and height, the length is calculated. Equation (3.12) shows the calculation of the intermediate quantity

Table 3.1: Specifications for filled parabolic reflector Cassegrain system compared to the DSN Station 11

Filled Aperture	Contour	Diameter	Focal Length	f/d ratio	Distance Between Apex and Primary Source
Primary	Parabolic	50m	26.67m	0.533	20m
Secondary	Hyperbolic	6.8462m	—	—	
DSN Station 11					
Primary	Parabolic	26m	—	—	—
Secondary	Hyperbolic	3.56m	—	—	

$\chi_{(trial)}$ for a given gain G_0 . The subscript *trial* indicates that this is a procedure repeated until desired results are obtained

$$\chi_{(trial)} = \chi_1 = \frac{G_0}{2\pi\sqrt{2\pi}}. \quad (3.12)$$

For this particular pyramidal horn, a gain of 20 dBi is used. The next design step is to use Equations (3.13) and (3.14) to solve for the horn slant lengths, ρ_e and ρ_h , respectively from χ and G_0

$$\frac{\rho_e}{\lambda} = \chi \Rightarrow \rho_e = \lambda\chi \quad (3.13)$$

$$\frac{\rho_h}{\lambda} = \frac{G_0^2}{8\pi^3} \left(\frac{1}{\chi} \right) \Rightarrow \rho_h = \frac{\lambda G_0^2}{8\pi^3} \left(\frac{1}{\chi} \right). \quad (3.14)$$

Then, to solve for the horn width and length, a_1 and b_1 , the following equations are used:

$$a_1 = \sqrt{3\lambda\rho_h} = \frac{G_0}{2\pi} \sqrt{\frac{3}{2\pi\chi}} \lambda \quad (3.15)$$

$$b_1 = \sqrt{2\lambda\rho_e} = \sqrt{2\chi\lambda}. \quad (3.16)$$

Finally, to solve the the horn height, the following equation is used:

$$p_e = p_h = (b_1 - b) \left[\left(\frac{\rho_e}{b_1} \right)^2 - \frac{1}{4} \right]^{1/2} = (a_1 - a) \left[\left(\frac{\rho_h}{a_1} \right)^2 - \frac{1}{4} \right]^{1/2}, \quad (3.17)$$

where the dimensions a and b are the length and width of the waveguide feeding the horn antenna. The resulting dimensions are shown in Figure 3.10.

Finally, using SATCOM™, the pyramidal horn antenna is simulated in an ideal free-space environment to obtain the radiation pattern. The end use for this pattern is then to provide an input to the filled aperture Cassegrain system. This is explained next.

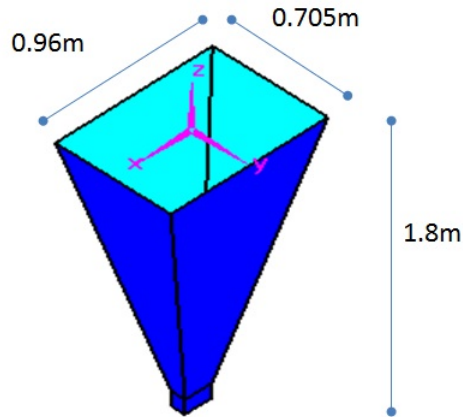


Figure 3.10: Illustration of pyramidal horn antenna designed to feed the filled aperture Cassegrain system

The final step in calculating the baseline is to simulate the performance of the filled aperture system using CEM methods. This is accomplished with two simulations performed using SATCOM™, which specializes in the design of antenna systems for satellite communications. The software uses the Physical Theory of Diffraction in solving Maxwell's

equations for the Far-Field (FF) radiation pattern of an antenna system. The first simulation uses an analytically specified antenna pattern as the feeding pattern to the filled aperture system without the subreflector. The second simulation uses the pyramidal horn as the feeding structure to the filled aperture with the subreflector. Section 4.4 shows the radiation patterns of the pyramidal horn antenna and the results of the filled aperture system with the analytical feed pattern and the pyramidal horn antenna as the feeding structures.

3.5 Feed Design for the Cross-shaped, Parabolically Contoured Reflector

Conventional antenna feed systems such as a basic horn antenna are not the optimal choice for the sparse reflector due to the energy wasted in the segments between the reflector arms. Therefore, two particular feed designs are proposed as possible feeding structures for the sparse reflector. The first is an aperture that resembles the sparse reflector cross-section. The second is a 2-Dimensional phased array that is comprised of two linear phased arrays orthogonal to one another. These two concepts are shown in Figures 3.11 and 3.12 respectively. Pursuing these feeding structures that resemble the sparse reflector is motivated by the inverse Fourier relationship between the directivity of the Far-Field (FF) radiation pattern of an antenna and its spatial dimensions. This relationship can be summarized with a scenario: an aperture antenna with a narrow rectangular opening will yield a FF pattern that is more directive, or narrower in beamwidth, across the longer dimension of the aperture and less directive, or wider in beamwidth, across the shorter dimension. The expectation is that the horizontal segments of either feeding structure will generate a portion of the FF radiation pattern that will correspond to the vertical segment of the sparse reflector. Similarly, the vertical segment of either feeding structure is expected to generate a portion of the FF radiation pattern that will correspond to the horizontal segment of the sparse reflector. Therefore these feeding structures are expected to result in a minimal amount of energy directed towards the sections between the arms of the sparse reflector.

Due to the complexity involved in designing a feeding structure, only the aperture is designed and analyzed in this thesis. This section of the thesis explores the use of an aperture antenna by first applying eigenmode analysis using a Finite-Difference (FD) approach to solve for the cutoff frequencies associated with a cross-shaped aperture. Then, using the field distributions of the dominant Transverse Magnetic (TM) and Transverse Electric (TE) modes, an equivalent problem is developed using Love's Equivalence Principle to determine the equivalent current densities within the aperture [16]. These current densities are then used to solve for the radiated FF due to the original field distribution within the aperture. Section A.3 presents the program used to perform all computations developed in this section.

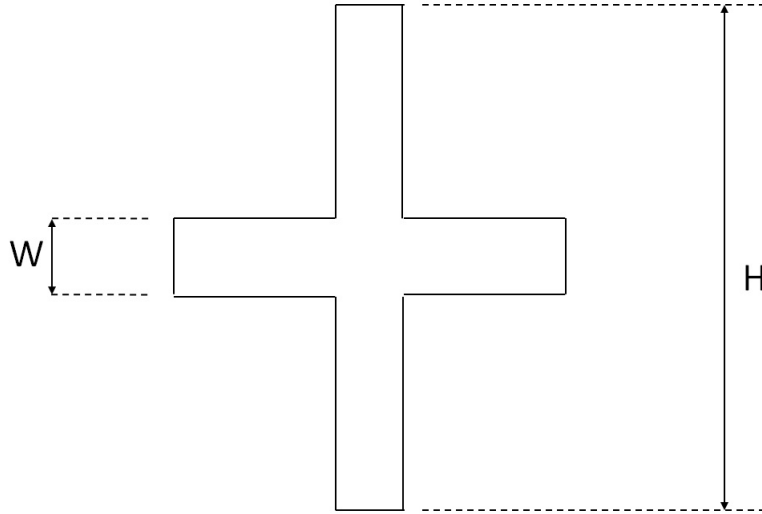


Figure 3.11: Cross-shaped aperture concept for feeding structure of sparse reflector

In starting this design process, the degrees of freedom are first identified as the dimensions of the aperture in Figure 3.11 labeled as W and H . These variables are to be refined as more design iterations are performed. In this first iteration, the dimensions W and H are determined by calculating the necessary First Null Beam Width (FNBW) for the dimensions of the sparse reflector. Figure 3.13 shows an illustration of the needed

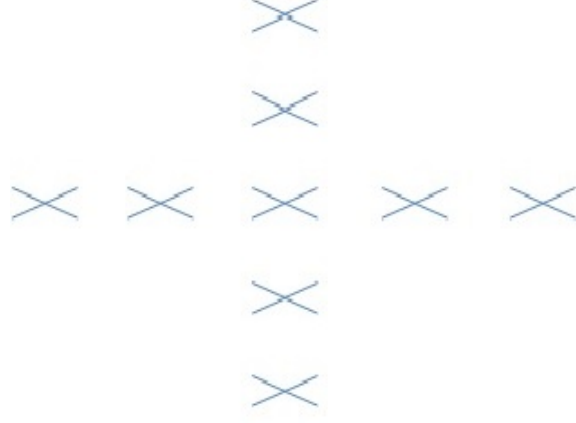


Figure 3.12: Cross-shaped phased array concept for feeding structure of sparse reflector

beamwidths. These angles are determined by studying the right triangle formed by the focal point, the center point of the reflector translated to be colinear with the edge of the sparse reflector, and the edge point of the sparse reflector. This triangle is shown in Figure 3.14. The angle labeled $\theta/2$ is calculated as

$$\frac{\theta}{2} = \tan^{-1} \left(\frac{75}{62.42} \right) = 50.23^\circ, \quad (3.18)$$

which implies then that the FNBW for the largest dimension of the sparse reflector is 100.46° . By a similar token, the FNBW associated with the smaller dimension of the sparse reflector is found to be 6.18° .

Based on these FNBWs, the aperture dimensions are then calculated using developments in [2]. In particular, Equation (3.19) shows the expression that relates the needed beamwidth with a dimension of the aperture, b ,

$$b = \frac{\sin\left(\frac{\theta}{2}\right)}{\lambda}, \quad (3.19)$$

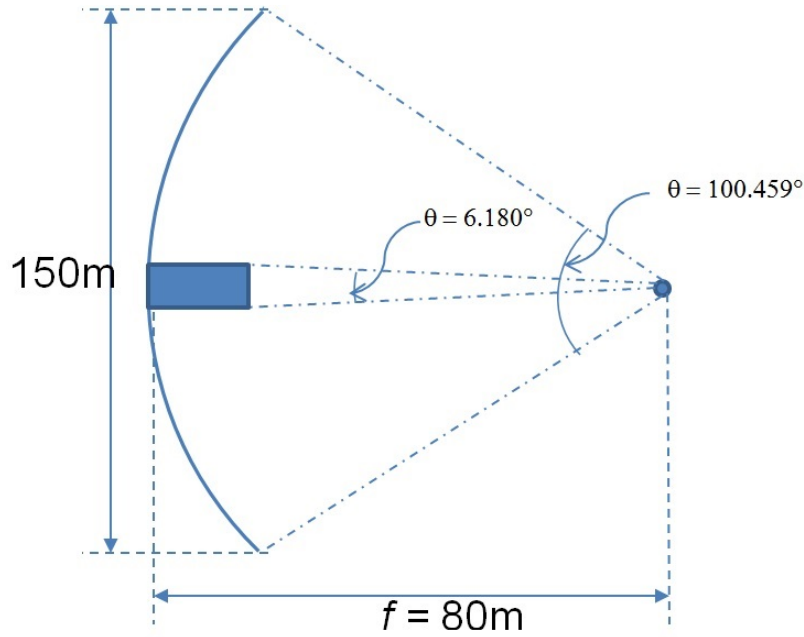


Figure 3.13: The needed beamwidths to illuminate the entire cross-shaped reflector

where λ is the wavelength, Θ is the FNBW previously found, and b is one of the dimensions W or H of the aperture.

3.5.1 Solving for the Field Distributions Within the Cross-Shaped Aperture using a FD Approach to Eigenmode Analysis.

In order to calculate the FF radiation pattern from the aperture shape in Figure 3.11, a solution of field distributions within the aperture is found using Eigenmode analysis. Solving for the field distributions within a cross-section of a waveguide is analogous to solving for the field distributions within an aperture. Both problems are 2-Dimensional problems only needing solutions in the transverse directions and not the longitudinal direction. Figure 3.15 shows the coordinate convention used in the eigenmode analysis. The origin is the lower left hand corner of the aperture. The xy -plane contains the aperture and includes the transverse directions. The z -direction is the longitudinal direction.

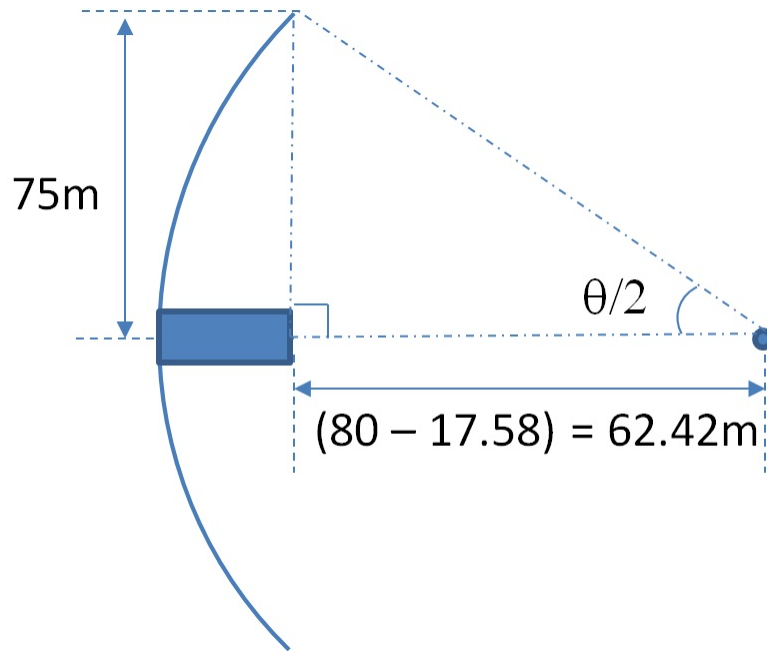


Figure 3.14: Trigonometry used to solve for needed beamwidths and aperture feeding structure dimensions

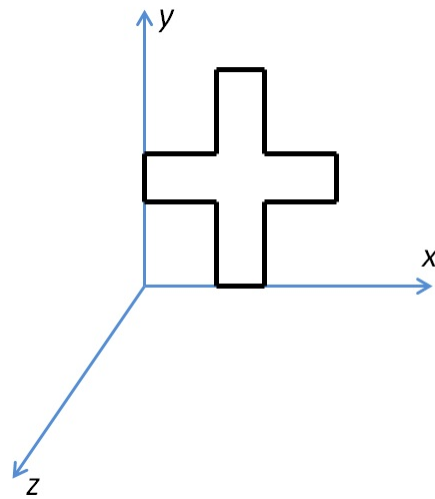


Figure 3.15: Coordinate convention used in Eigenmode analysis for cross-shaped aperture

The equations to be solved for the TE^z and TM^z mode sets are derived from Maxwell's equations. The derivation for this 2-Dimensional problem yields the following two equations [18]:

$$\text{TM}^z \text{ Modes: } (\nabla^2 + k_t^2)E_z = 0, \quad E_z|_{\Gamma} = 0 \quad (3.20)$$

$$\text{TE}^z \text{ Modes: } (\nabla^2 + k_t^2)H_z = 0, \quad \left. \frac{\partial H_z}{\partial n} \right|_{\Gamma} = 0. \quad (3.21)$$

The derivation details have been omitted here for brevity. Note that the partial derivative with respect to n indicates with respect to the normal component. This component varies depending on which boundary in the aperture the derivative is being applied. Also, the use of Γ indicates evaluation at the boundary, where Γ is the overall boundary of the aperture. Finally, k_t is the transverse wavenumber associated with the aperture, which is equal to:

$$\sqrt{k_x^2 + k_y^2} = \frac{2\pi}{\lambda}(\sin \theta \cos \phi + \sin \theta \sin \phi).$$

Generalizing this problem results in the following equation [18]:

$$\nabla^2 u = \lambda u \quad u|_{\Gamma} = 0 \quad \text{or} \quad \left. \frac{\partial u}{\partial n} \right|_{\Gamma} = 0, \quad (3.22)$$

where u can be either E_z or H_z for the TM^z or TE^z mode sets respectively. In generalizing this problem, $\lambda = -k_t^2$, which when the Laplacian operator is discretized, can be understood as an eigenvalue. Therefore, the function u can be understood then as an eigenvector which corresponds to later used equivalent current sources used to compute the FF pattern of the cross-shaped aperture. Section 3.5.3 describes the discretization of the Laplacian operator and the associated linear system that results.

After obtaining the eigenvalues, the cutoff frequencies of the waveguide can be calculated. A cutoff frequency is the frequency where propagation through the waveguide

stops and can be found from the following relationship [16] [18] [26]:

$$k_t^2 + k_z^{\prime} = k_0^2, \quad (3.23)$$

where the k_z^{\prime} indicates that $k_z = 0$ meaning no propagation occurs. Therefore, using the relationship $\lambda = -k_t^2$ and Equation (3.23), the cutoff frequencies can be solved as:

$$f_{c,mn} = \frac{1}{2\pi} \sqrt{\frac{-\lambda_{mn}}{\mu_0 \epsilon_0}}, \quad (3.24)$$

where the subscript c indicates cutoff, the subscript mn stands for mode number (i.e. TE_{10}), and the substitutions $k = \frac{2\pi f}{c}$, $c = \sqrt{\mu\epsilon}$, and $\lambda = -k_t^2$ have been made. c is the speed of light in free space, μ_0 is the permeability associated with the medium, and ϵ_0 is the permittivity associated with the medium.

3.5.2 Solving for the FF Radiation Pattern of the Cross-Shaped Aperture Using Love's Equivalence Principle.

Applying Love's Equivalence Principle simplifies the problem by allowing for the use of the Free Space Green's Function (FSGF) shown in Equation (2.64). The FSGF can then be used as a kernel in the radiation integrals shown later, which simplifies their evaluations. The form of the FSGF takes advantage of the FF approximation, which means the function can be split into two distinct portions; one with respect to only the observer or FF and one with respect only to the source. This split in the function means the FF portion can be moved outside of the radiation integral because the integration is only evaluated over the source variables.

From Maxwell's equations, the field set relations for the TM^z and TE^z modes for 2-Dimensional Cartesian geometries can be written as:

$$\begin{aligned} \nabla_t \times \mathbf{H}_t &= \hat{z}J_z + \hat{z}j\omega\epsilon E_z \\ \text{TM}^z : \quad \nabla_t \times (\hat{z}E_z) &= -\mathbf{M}_t - j\omega\mu\mathbf{H}_t, \\ \nabla_t \cdot \mathbf{H}_t &= \frac{q_{mv}}{\mu} = \frac{-\nabla_t \cdot \mathbf{M}_t}{j\omega\mu} \end{aligned} \quad (3.25)$$

$$\begin{aligned} \nabla_t \times \mathbf{E}_t &= -\hat{z}M_z - \hat{z}j\omega\mu H_z \\ \text{TE}^z : \quad \nabla_t \times (\hat{z}H_z) &= \mathbf{J}_t + j\omega\epsilon\mathbf{E}_t, \\ \nabla_t \cdot \mathbf{E}_t &= \frac{q_{ev}}{\epsilon} = \frac{-\nabla_t \cdot \mathbf{J}_t}{j\omega\epsilon} \end{aligned} \quad (3.26)$$

where the subscript t indicates transverse.

Equations (3.25) - (3.26) are general expressions for the field components in the TM^z and TE^z cases where the following field components exist for each:

$$\begin{aligned} \text{TM}^z : & E_z, H_x, H_y, J_z, M_x, M_y, q_{mv} \\ \text{TE}^z : & H_z, E_x, E_y, M_z, J_x, J_y, q_{ev} \end{aligned} .$$

In solving for the unknown equivalent current densities from Love's Equivalence Principle, the transverse field components within the aperture are necessary. From the previous Eigenmode analysis, an approximation for the longitudinal field component is known. Therefore, only the transverse field components need to be calculated. Realizing that each of the second equations in Equations (3.25) - (3.26) contains the needed relationships between the field components, the other equations may be ignored. Further developing the equations and making the assumption that the aperture is source free, the equations become:

$$\begin{aligned} \nabla_t \times (\hat{z}E_z) &= -j\omega\mu\mathbf{H}_t \\ \Rightarrow \mathbf{H}_t &= \frac{-1}{j\omega\mu} \left(\hat{x} \frac{\partial E_z}{\partial y} - \hat{y} \frac{\partial E_z}{\partial x} \right), \end{aligned} \quad (3.27)$$

$$\begin{aligned}\nabla_t \times (\hat{z}H_z) &= j\omega\epsilon\mathbf{E}_t \\ \Rightarrow \mathbf{E}_t &= \frac{1}{j\omega\epsilon} \left(\hat{x}\frac{\partial H_z}{\partial y} - \hat{y}\frac{\partial H_z}{\partial x} \right).\end{aligned}\quad (3.28)$$

Using these expressions for the transverse field components, the equivalent current densities are calculated by:

$$\mathbf{J}_{eq} = 2\hat{z} \times \mathbf{H}_t = -\hat{x}\frac{2}{j\omega\mu}\frac{\partial E_z}{\partial x} - \hat{y}\frac{2}{j\omega\mu}\frac{\partial E_z}{\partial y}, \quad (3.29)$$

$$\mathbf{M}_{eq} = -2\hat{z} \times \mathbf{E}_t = -\hat{x}\frac{2}{j\omega\epsilon}\frac{\partial H_z}{\partial x} + \hat{y}\frac{2}{j\omega\epsilon}\frac{\partial H_z}{\partial y}. \quad (3.30)$$

As stated previously, the goal of this development is to obtain the FF radiation pattern of the cross-shaped aperture feeding structure. The FF region is a generalized term used to describe being far enough away from a radiating structure such that radiated waves have a planar wave front relative to the wavelength, λ . Also, the largest dimension of the radiating structure, D , is used to describe the FF region of an antenna as can be seen in the following estimate of the FF distance [2]:

$$R \geq \frac{2D^2}{\lambda}. \quad (3.31)$$

In the FF region, calculating the radiated fields is simplified because the integrands in the integral equations can be approximated more easily (or solved in closed-form) and the FSGF can be split into source and observer variable parts. Balanis develops the expressions for calculating the FF radiated fields based on a particular current density in [2] and [16]. The details of the development are omitted here for conciseness, but the final expressions are presented as:

$$\begin{aligned}N_\theta &= \int_S (J_x \cos \theta \cos \phi + J_y \cos \theta \sin \phi - J_z \sin \theta) e^{-jkr' \cos \psi} dS' \\ N_\phi &= \int_S (-J_x \sin \phi + J_y \cos \phi) e^{-jkr' \cos \psi} dS'\end{aligned}, \quad (3.32)$$

$$\begin{aligned}
L_\theta &= \int_S (M_x \cos \theta \cos \phi + M_y \cos \theta \sin \phi - \cancel{M_z \sin \theta}) e^{-jkr' \cos \psi} dS' \\
L_\phi &= \int_S (-M_x \sin \phi + M_y \cos \phi) e^{-jkr' \cos \psi} dS'
\end{aligned} \tag{3.33}$$

$$\begin{aligned}
E_\theta &\simeq \frac{-jke^{-jkr}}{4\pi r} (L_\phi + \eta N_\theta) \\
E_\phi &\simeq \frac{jke^{-jkr}}{4\pi r} (L_\theta - \eta N_\phi)
\end{aligned} \tag{3.34}$$

The $\cancel{J_z \sin \theta}$ and $\cancel{M_z \sin \theta}$ terms are used to indicate that no z component exists for the equivalent current densities within the aperture. Also, the $r' \cos \psi$ terms shown in the exponentials become $x' \sin \theta \cos \phi + y' \sin \theta \sin \phi$ by the coordinate convention used in Figure 3.15. Finally, as mentioned in Chapter 2, the primed variables are referred to as source variables and the unprimed variables are referred to as observer or FF variables. Section 3.5.4 describes the numerical methods for approximating the equivalent current densities and calculating the resulting FF radiation patterns.

3.5.3 Discretizing the Laplacian Operator Using a Central Difference Approximation.

As shown previously, the Laplacian operator needs to be discretized for a given aperture grid. The discretization is best accomplished by applying a stencil to the grid. The stencil used in this thesis is a central difference approximation of the second derivatives [18]. This is written generally as:

$$\frac{\partial^2 u(x, y)}{\partial x^2} \approx \frac{u(x + \Delta x, y) - 2u(x, y) + u(x - \Delta x, y)}{\Delta x^2}, \tag{3.35}$$

where u is a place holder for a 2-Dimensional scalar function and Δx is the step size on the x dimension of the grid.

Applying this stencil to the laplacian operator in Equation (3.22) yields the following:

$$\nabla^2 u(x, y) \approx \frac{u(x + h, y) - 2u(x, y) + u(x - h, y)}{h^2} + \frac{u(x, y + h) - 2u(x, y) + u(x, y - h)}{h^2}, \tag{3.36}$$

where it is assumed that $\Delta x = \Delta y = h$.

This stencil can be applied to any generalized grid in a systematic fashion. The application is to a columnwise indexed grid as shown in Figure 3.16. It is worth noting at this point that the boundaries are set as zeros which implicitly takes care of the TM^z boundary conditions shown in Equation (3.20). The TE^z boundary conditions in Equation (3.21) are handled explicitly as can be seen in the code found in Section A.3.

	1	2	3	4	5	6	7	8	9	10	11	12	13	14	15	16	17	18	19	20	21	22	23	24	25
1	0	0	0	0	0	0	0	0	0	0	0	0	0	0	0	0	0	0	0	0	0	0	0	0	0
2	0	0	0	0	0	0	0	0	0	0	46	69	92	115	138	0	0	0	0	0	0	0	0	0	0
3	0	0	0	0	0	0	0	0	0	0	47	70	93	116	139	0	0	0	0	0	0	0	0	0	0
4	0	0	0	0	0	0	0	0	0	0	48	71	94	117	140	0	0	0	0	0	0	0	0	0	0
5	0	0	0	0	0	0	0	0	0	0	49	72	95	118	141	0	0	0	0	0	0	0	0	0	0
6	0	0	0	0	0	0	0	0	0	0	50	73	96	119	142	0	0	0	0	0	0	0	0	0	0
7	0	0	0	0	0	0	0	0	0	0	51	74	97	120	143	0	0	0	0	0	0	0	0	0	0
8	0	0	0	0	0	0	0	0	0	0	52	75	98	121	144	0	0	0	0	0	0	0	0	0	0
9	0	0	0	0	0	0	0	0	0	0	53	76	99	122	145	0	0	0	0	0	0	0	0	0	0
10	0	0	0	0	0	0	0	0	0	0	54	77	100	123	146	0	0	0	0	0	0	0	0	0	0
11	0	1	6	11	16	21	26	31	36	41	55	78	101	124	147	161	166	171	176	181	186	191	196	201	0
12	0	2	7	12	17	22	27	32	37	42	56	79	102	125	148	162	167	172	177	182	187	192	197	202	0
13	0	3	8	13	18	23	28	33	38	43	57	80	103	126	149	163	168	173	178	183	188	193	198	203	0
14	0	4	9	14	19	24	29	34	39	44	58	81	104	127	150	164	169	174	179	184	189	194	199	204	0
15	0	5	10	15	20	25	30	35	40	45	59	82	105	128	151	165	170	175	180	185	190	195	200	205	0
16	0	0	0	0	0	0	0	0	0	0	60	83	106	129	152	0	0	0	0	0	0	0	0	0	0
17	0	0	0	0	0	0	0	0	0	0	61	84	107	130	153	0	0	0	0	0	0	0	0	0	0
18	0	0	0	0	0	0	0	0	0	0	62	85	108	131	154	0	0	0	0	0	0	0	0	0	0
19	0	0	0	0	0	0	0	0	0	0	63	86	109	132	155	0	0	0	0	0	0	0	0	0	0
20	0	0	0	0	0	0	0	0	0	0	64	87	110	133	156	0	0	0	0	0	0	0	0	0	0
21	0	0	0	0	0	0	0	0	0	0	65	88	111	134	157	0	0	0	0	0	0	0	0	0	0
22	0	0	0	0	0	0	0	0	0	0	66	89	112	135	158	0	0	0	0	0	0	0	0	0	0
23	0	0	0	0	0	0	0	0	0	0	67	90	113	136	159	0	0	0	0	0	0	0	0	0	0
24	0	0	0	0	0	0	0	0	0	0	68	91	114	137	160	0	0	0	0	0	0	0	0	0	0
25	0	0	0	0	0	0	0	0	0	0	0	0	0	0	0	0	0	0	0	0	0	0	0	0	0

Figure 3.16: Illustration of how the discrete grid for the cross-shaped aperture is indexed for numerically evaluating the Laplacian operator

The creation of the grid shown in Figure 3.16 is performed using the MATLAB[®] function `numgrid()` to generate the grid for use with a FD algorithm. However, in order to generate the cross-shaped grid, a special case is added to the function where a given fraction is used with boolean algebra to determine which columns and rows to omit.

To apply the stencil to the grid shown in Figure 3.16, the MATLAB[®] function `delSq()` is used. This function expects an input FD grid indexed columnwise and generates the discrete Laplacian matrix assuming unit step size. In solving for the cutoff frequencies from

the eigenvalues, Equation (3.24) must be modified to account for step sizes other than unit step size. This modification is shown in Equation (3.37):

$$f_{c,mn} = \frac{1}{2\pi h} \sqrt{\frac{-\lambda_{mn}}{\mu_0 \epsilon_0}}. \quad (3.37)$$

Figure 3.17 shows the pattern of the discrete Laplacian output by the `delsq()` function. MATLAB® stores the output as a sparse matrix data structure due to the large number of zeros in the matrix. Operating on a sparse matrix data structure results in faster computation of the eigenvalues and eigenvectors which is accomplished by use of the `eigs()` function. Equation (3.24) is then used to calculate the cutoff frequencies from the eigenvalues.

3.5.4 Numerically Computing the FF Radiation Pattern of the Cross-Shaped Aperture.

In order to numerically compute the equivalent current sources that result from Love's Equivalence Principle, an approximation to the partial derivatives shown in Equations (3.29) - (3.30) must be made. As shown previously, the central difference approximation for derivatives is a good choice for this task. Applying the central difference approximation yields the following expressions for the equivalent current densities:

$$\mathbf{J}_{eq} \approx -\hat{x} \frac{\mathcal{Z}}{j\omega\mu} \frac{E_z(x, y+h) - E_z(x, y-h)}{2h} - \hat{y} \frac{\mathcal{Z}}{j\omega\mu} \frac{E_z(x+h, y) - E_z(x-h, y)}{2h}, \quad (3.38)$$

$$\mathbf{M}_{eq} \approx -\hat{x} \frac{\mathcal{Z}}{j\omega\epsilon} \frac{H_z(x, y+h) - H_z(x, y-h)}{2h} + \hat{y} \frac{\mathcal{Z}}{j\omega\epsilon} \frac{H_z(x+h, y) - H_z(x-h, y)}{2h}. \quad (3.39)$$

The last large step in obtaining the FF radiation pattern of the cross-shaped aperture is performing the integrations to obtain the **N** and **L** FF potentials vector components. Given that the current densities are in a numerical format as opposed to an analytical expression,

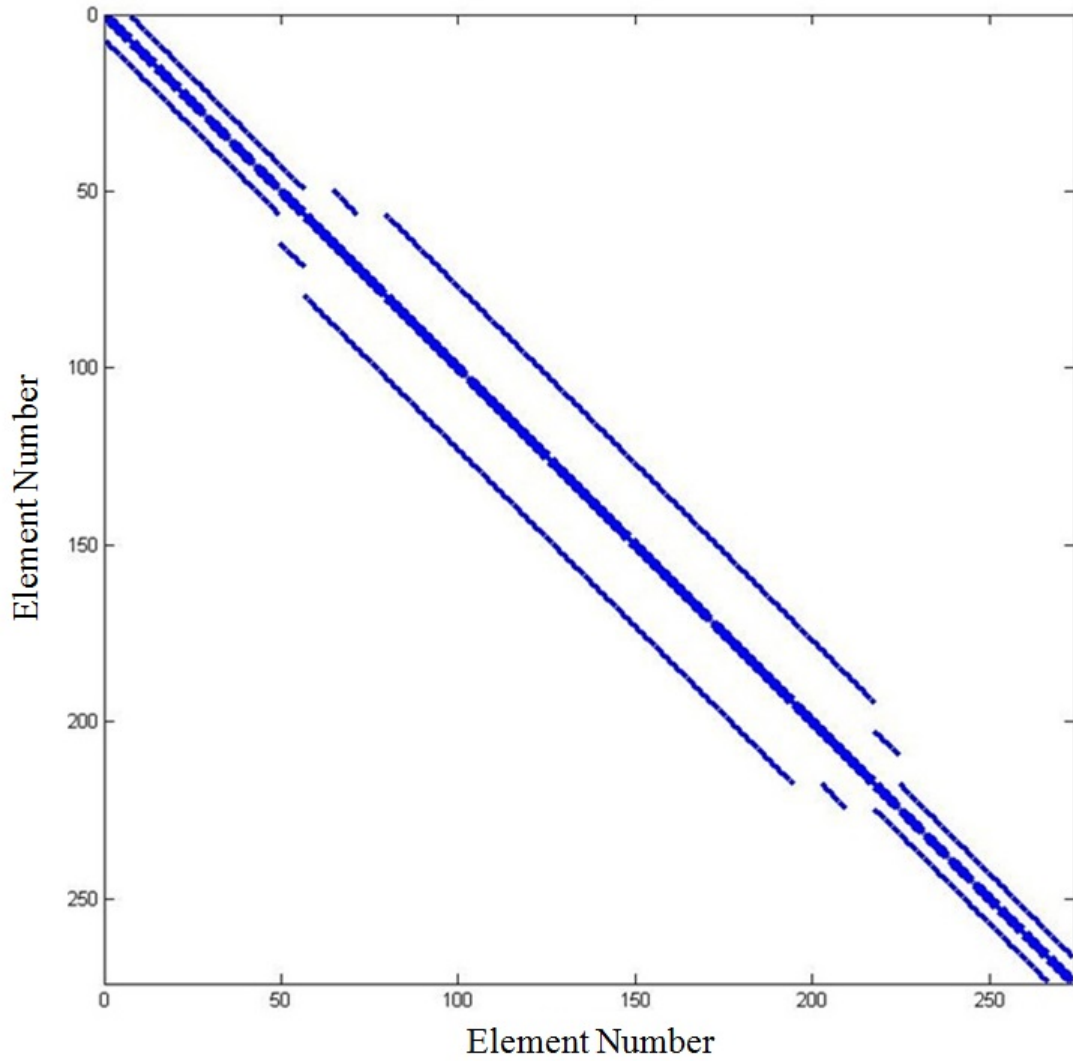


Figure 3.17: Discretizing the Laplacian operator generates a sparse matrix that follows a specific pattern as shown here

this problem lends itself to numerical integration techniques. In particular, the nine-point integration rule from [27] is the method of choice.

The nine-point integration rule uses nine points in a single subdomain as shown in Figure 3.18 and sums the function evaluated at them with proper weights applied to each

evaluated point. Equation (3.40) shown as:

$$I = 4h^2 \sum_i w_i \phi(x_i, y_i, 0), \quad (3.40)$$

illustrates the evaluation over a single subdomain shown in Figure 3.18 with the weights listed in Table 3.2. The function $\phi(x, y, z)$ is a generalized function of 3 variables which is a place holder for the equivalent current densities. To further apply this method, the replication of subdomains across the aperture until all the points are included is accomplished by having the center point for each subdomain lie outside of the adjacent subdomain boundaries by 1 sample. A certain number of grid points must be used to accomodate the nine-point integration rule properly. Otherwise, other rules would be needed. For this research, the choice of $N = 165$ is used.

Computing the **N** and **L** FF potentials vector components is accomplished using four nested for-loop constructs: two for-loops over the observer variables, one over all of the subdomains within the aperture, and one over the nine points in each subdomain.

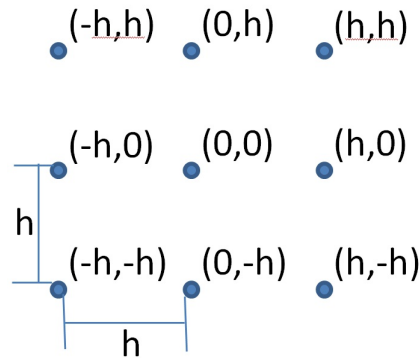


Figure 3.18: A single subdomain used to perform Nine-Point Integration over the cross-shaped aperture

See Sections 4.5 and 5.5 for the results and discussion from the method presented in this section. Also, see Section A.3 for the program developed for this method.

Table 3.2: Nine-point integration rule weights

i	x	y	w_i
1	-h	-h	$1/36$
2	0	-h	$1/9$
3	h	-h	$1/36$
4	-h	0	$1/9$
5	0	0	$4/9$
6	h	0	$1/9$
7	-h	h	$1/36$
8	0	h	$1/9$
9	h	h	$1/36$

IV. Results & Analysis

The results from each step in the methodology are presented in this chapter along with analysis. This chapter presents results from the geometrical analysis of both reflector antennas, the ray-tracing of both reflector antennas, the plane wave analysis of each reflector antenna, the sky study for the rectangular shaped, spherically contoured reflector (spherical reflector), the baseline antenna calculation for the cross-shaped, parabolically contoured reflector (sparse reflector) antenna, and finally the results from designing the cross-shaped aperture feed antenna for the sparse reflector.

4.1 Geometrical Analysis

As shown earlier in Section 3.1.1, the degree of freedom for the spherical reflector is the radius of curvature. The radius of curvature is then related to the known width and height dimensions of 304.8 meters and 91.44 meters by using the equation for the length of a chord of a circle, given in Equation (3.1). In the plane wave analysis and sky study, it is shown that a radius of curvature of 60.96 meters is feasible. Compared to the sparse reflector, which has no degree of freedom with respect to the geometry, the spherical reflector has more geometrical analysis to finalize its geometry before proceeding to designing a feeding antenna. However, the main objective of analyzing the geometry of each reflector is to obtain several figures of merit, shown in Table 4.1. In particular, it is seen that the largest dimension of each antenna is on the order of 1000λ . It is typical that a geometry be sampled ten times per wavelength in the discretization for a Computational Electromagnetics (CEM) solution [18]. This requirement is slightly different for time-domain methods which must satisfy the Nyquist-Shannon Sampling Theorem [18]. From Table 4.1 and following the sampling requirements for a CEM solution, a mesh cell or sample count will be on the order of 10^6 . Performing the simulation for a mesh cell count on the order of 10^6 is not feasible for

Table 4.1: Geometrical analysis results of each reflector

	Rectangular Shaped, Spherically Contoured Reflector	Cross-Shaped, Parabolically Contoured Reflector
Wavelengths of Operation (m) (IEEE L-Band)	0.1499 - 0.2998	0.1499 - 0.2998
Largest Dimension of Reflector (m)	304.8	150
Number of Wavelengths Across Reflector Largest Dimension	1016.68 - 2033.36	500.33 - 1000.67
Approximate Reflector Surface Area (m²)	27870.9	2022
Approximate Reflector Edge Surface Area (10λ ring) (m²)	1187.93 - 2375.85	469.91 - 939.81
Radius of Curvature/Focal Length (m)	609.6 - 1524	80

current computing systems. This limitation leads to the use of less computational intensive methods to analyze the reflector antennas for this thesis. These include ray-tracing and Far-Field (FF) analyses of the reflectors using optical approximations.

4.1.1 Ray-Tracing Procedure: Rectangular Shaped , Spherically Contoured Reflector.

In performing ray-tracing, there is no strict requirement for sampling the reflector. Therefore, for this thesis, the height and width of the spherical reflector are sampled ten times to visualize the caustic surface and keep runtime short. The use of the MATLAB® `surf()` command creates a continuous surface for visualization purposes, which is the main objective of ray-tracing. Then, using the `quiver()` and `quiver3()` commands, the rays are plotted at each step along the grid. The calculations for the rays are described in Section 3.1.2.

Figure 4.1 shows the resulting 2-Dimensional ray-tracing cross-section for the spherical reflector. The axes are marked in meters showing an accurate representation of the spherical

reflector with a radius of curvature equal to 60.96 meters. The scale of the plot makes it difficult to see the formation of the caustic envelope. The caustic envelope is explained in Section 2.1. Figure 4.1 is presented at this scale to show that the rays are focusing near a point that is measured to be half the radius of curvature away from the spherical reflector. This point constitutes the paraxial focus. An expanded plot is shown around the paraxial focus where the caustic envelope forms. However, as compared to the example spherical reflector in Section 2.1, this caustic envelope is smaller relative to the spherical reflector. Reduction in the size of the caustic envelope is attributed to the very long radius of curvature. The spherical reflector appears nearly flat at the scale it is presented, but the expanded view of the caustic envelope shows that the reflector is indeed spherically contoured.

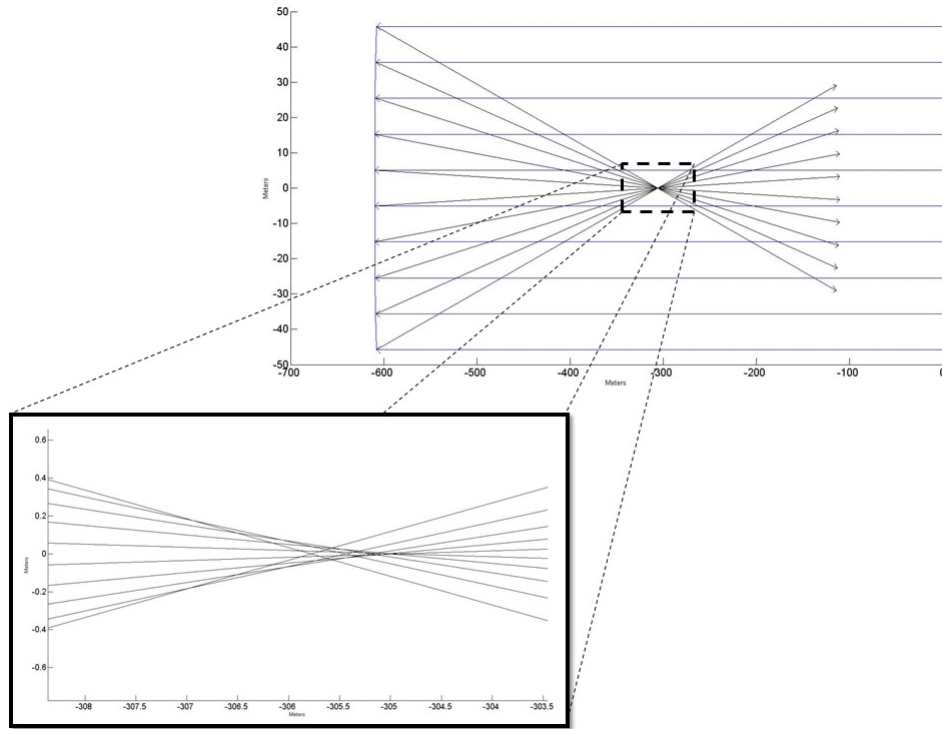


Figure 4.1: Ray-tracing for 2-Dimensional cross-section of the spherical reflector with formation of caustic envelope highlighted. Only the incident and reflected rays are plotted.

Figure 4.2 shows an extension to the 2-Dimensional ray-tracing figure. The spherical reflector is shown as a solid surface with several incident rays and the corresponding reflected rays. Again, the scale of the plot is not conducive to viewing the caustic envelope and thus an expanded plot is shown to clarify it. The 3-Dimensional plot agrees well with the 2-Dimensional plot showing that the caustic envelope for this particular radius of curvature and reflector size is not as large, relative to the spherical reflector, as the caustic envelope, relative to the example reflector discussed previously in Section 2.1. This reduction in size of the caustic envelope cause the rays to nearly converge to a single point. However, the spherical aberrations cause phase errors, meaning a correction must be performed by the feeding structure for the spherical reflector. In regards to these aberrations, the wavelength, λ , is the figure used to measure aberrations or phase errors. In particular, if the energy received at the paraxial focus is out of phase by $\lambda/4$, significant losses in received signal will occur due to destructive interference. In other literature, a more conservative figure of $\lambda/16$ is used as the maximum tolerable phase error [1]. The results of the plane wave analysis later illustrate this loss in received energy and the energy spreading that occurs due to the aberrations. Also, the feeding structure dimensions are proposed based on physical steering constraints, the plane wave analysis results, and the sky study results.

4.1.2 Ray-Tracing Procedure: Cross-shaped, Parabolically Contoured Reflector.

As stated previously, there is no sampling requirement for performing ray-tracing as opposed to applying CEM methods. Therefore, the same sampling as the spherical reflector of 10 rays per 2-Dimensional cross-section is used. The 2-Dimensional ray-tracing for the sparse reflector is shown in Figure 4.3. As can be seen, the incident rays all reflect to a single focal point that is 80 meters away from the apex of the reflector as expected. The scale that the reflector is presented is too large to clearly see the focal point and so an expanded view is shown for clarification. Also note that the small rays protruding from the reflector are the surface normals as calculated using the method presented in Section 3.1.4. The

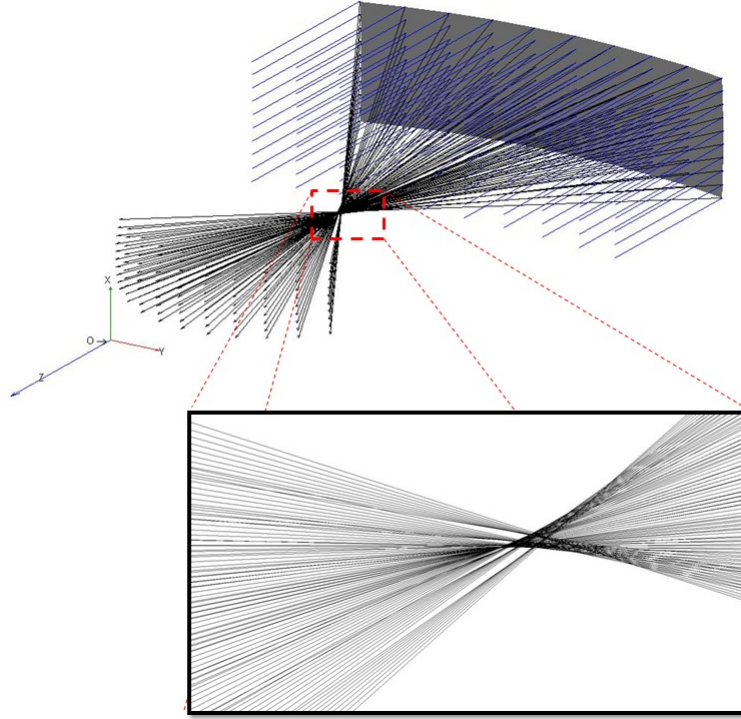


Figure 4.2: Ray-tracing for 3-Dimensional cross-section the spherical reflector with formation of caustic envelope highlighted. Only the incident and reflected rays are plotted.

calculation of the surface normals for the sparse reflector is not as simple as for the spherical reflector, and therefore the surface normals are shown in Figure 4.3 for reference to ensure the calculations are performed properly.

Similar to the spherical reflector ray-tracing, a 3-Dimensional extension of the 2-Dimensional ray-tracing for the sparse reflector is presented. The resulting 3-Dimensional ray-tracing is shown in Figure 4.4 with two viewing angles for better visualization of the overall reflector. All rays again are shown and the focal point is highlighted. Figure 4.4 agrees well with Figure 4.3 clearly showing that no aberrations are present. Placing a feeding structure at the focal point produces the best results for the reflector antenna system. The feeding structure will not have to correct for aberrations. This means less sophisticated

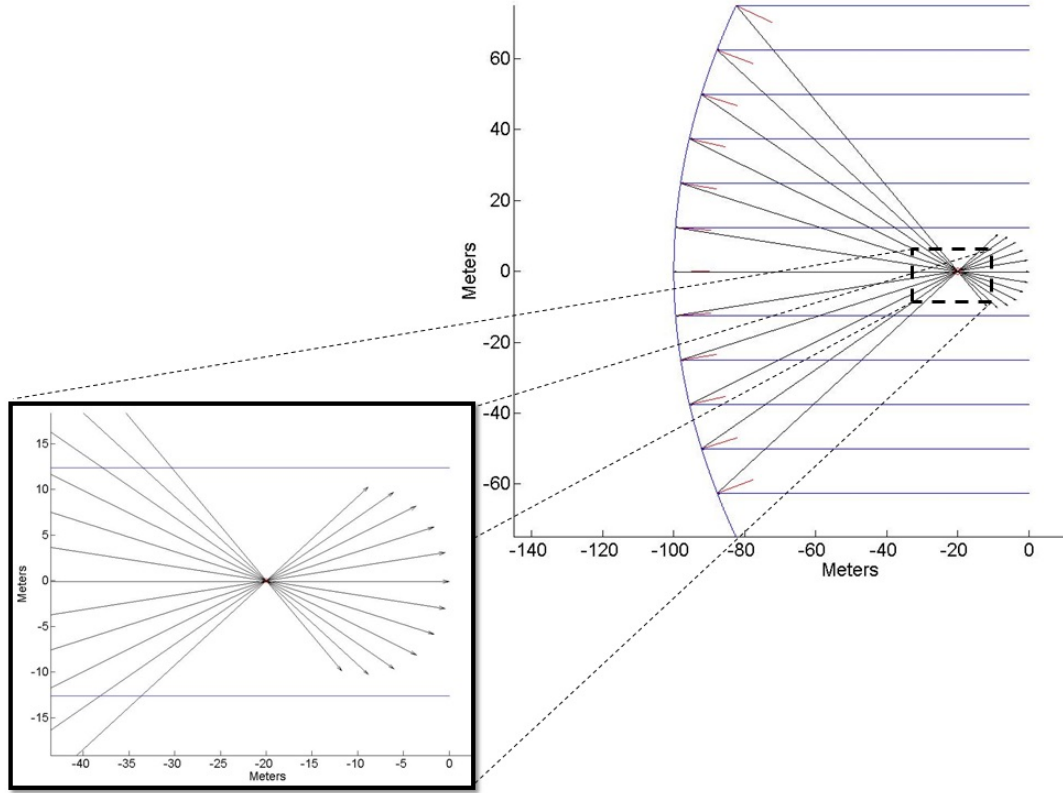


Figure 4.3: Ray-tracing for 2-Dimensional cross-section of the sparse reflector with focal point highlighted

designs, such as aperture antennas or phased arrays, can be explored in contrast to beam waveguide or Gregorian systems, which correct for aberrations [4] [5] [28].

Also, as a noteworthy design constraint, steering the antenna beam for the sparse reflector must be accomplished by steering the reflector and feeding structure simultaneously, posing a mechanical limitation. Designing the steering mechanisms for the sparse reflector is outside the scope of this thesis.

4.2 Plane Wave Analysis

This section is divided into two subsections, one for each reflector antenna examined in this thesis. The spherical reflector is analyzed using optical methods due to its electrical size and spherical contour. In particular, the aberrations caused by the spherical contour

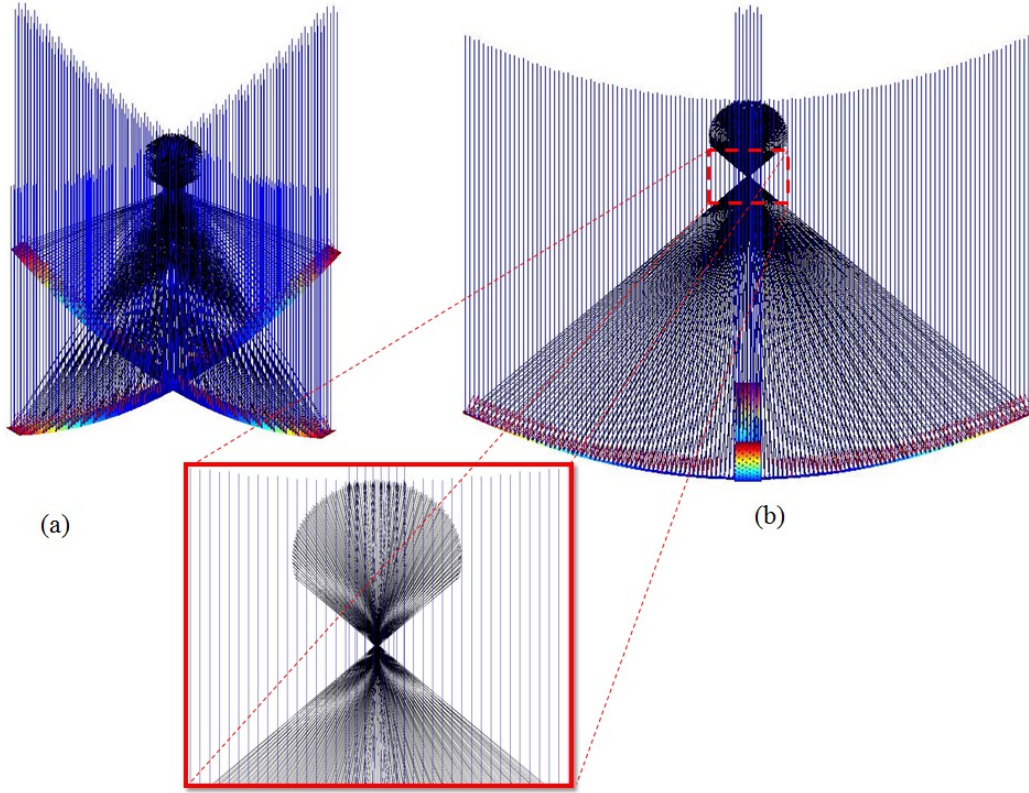


Figure 4.4: Ray-tracing for 3-Dimensional cross-section of the sparse reflector: (a) Oblique view illustrating cross-shape (b) Side-view with focal point highlighted

are considered in devising the feeding structure dimensional limitations and the steering limitations of the spherical reflector via moving the feeding structure. The methods are described in Section 3.2.1 and are implemented using MATLAB[®]. The results are presented in the first subsection.

In contrast, the sparse reflector is analyzed by feeding it with an analytically developed pattern and performing the simulation using a Physical Optics (PO) approximation in solving the radiation integral in the Far-Field (FF). This simulation is performed using SatCom[™] software. The results are presented in the second subsection.

4.2.1 Rectangular Shaped, Spherically Contoured Reflector.

In analyzing the spherical reflector in its receive mode, a plane wave is incident upon the surface. Equation (3.8) shows the analytical representation of the plane wave in the coordinate convention presented in Figure 3.5. As stated earlier, the same discretization as for the ray-tracing is used. However, the sampling of the surface is increased to ensure higher accuracy of the results. In applying the Fourier analysis method, a phase progression is induced in the plane wave expression from being incident upon the surface of the spherical reflector. The Discrete Fourier Transform is evaluated for the plane wave with the phase progression to obtain the amplitude distribution on an imaging plane. The plot of this is shown in Figure 4.5 where the left hand plot shows the resulting amplitude distribution for an on-axis plane wave incident on the spherical reflector and the right hand plot shows the amplitude distribution for a plane wave incident at 5° azimuth and 2° elevation. The imaging plane size was assumed as the maximum feeding structure size to avoid unwieldiness when moving it for steering purposes. The dimensions are further refined when using FKDI analysis.

The amplitude distribution is shown to be focused in both plots in Figure 4.5, but with lobing more prominent along the vertical axis. The vertical axis here corresponds to the shorter dimension of the spherical reflector. This lobing is caused by diffraction of the incident energy due to the finite extents of the spherical reflector. The Fourier Integral Transform is an infinite transform, but when performed discretely, must be truncated. If the Fourier transform is evaluated over a smaller aperture, more lobing will be seen in the imaging plane amplitude distribution. Thus, diffraction is not accounted for in Fourier analysis as can be seen. Looking now at the off-axis amplitude distribution, it again exhibits the lobing, but its center point has shifted due to the off-axis angle of incidence. The shifting of the center point for an off-axis incident plane wave is correct; however, the Fourier analysis fails to illustrate the energy spreading that takes place. The energy spreading is

caused by the spherical aberrations or phase errors inherent to the spherical reflector. Due to this inaccurate representation of the amplitude distribution from off-axis energy, the more accurate Fresnel-Kirchoff Diffraction Integral (FKDI) method is used, which accounts for diffraction.

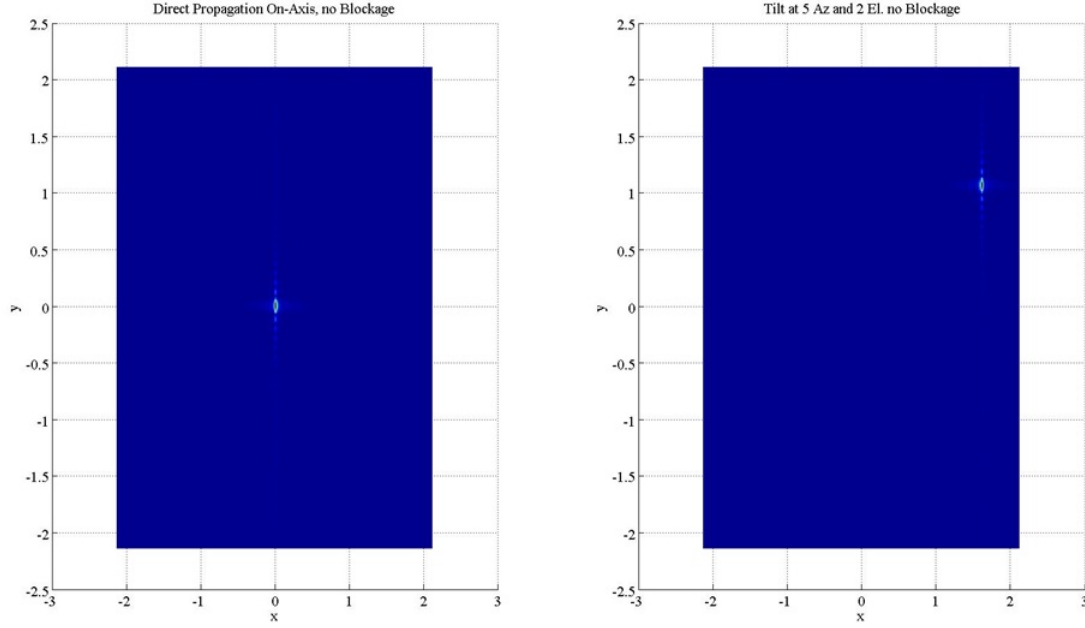


Figure 4.5: Left: On-axis propagation, no blockage amplitude distribution calculated using Fourier Analysis; Right: Tilted propagation at 5° azimuth and 2° elevation, no blockage amplitude distribution calculated using Fourier Analysis

Using Equation (3.10) from Section 3.2.1, the plots shown in Figure 4.6 are calculated. To ensure the data remained comparable for both methods, a similar experiment as for the Fourier analysis method is performed for the FKDI method. The only differences are that the image plane is shifted to keep the amplitude distribution centered as the incident energy angle changes to better visualize the energy spreading; and the imaging plane size is different because of the design decision to keep the feeding structure 10 meters by 10 meters. The Fourier analysis method determines the amplitude distribution center for shifting the

imaging plane in the FKDI method. The left hand plot in Figure 4.6 shows the amplitude distribution calculated on the imaging plane for an on-axis plane wave and the plot on the right shows the amplitude distribution calculated for a plane wave incident at 5° azimuth and 2° elevation. The first observation to notice is the energy spreading in both spots. The energy spreading is caused by the spherical aberrations. Comparing the two plots shows that as incident energy moves further off-axis, the aberrations become more apparent. The trail of energy that forms behind the main focus in the amplitude distribution is a typical result of spherical aberrations and gives insight into how a feeding structure should be designed. A feeding structure should be designed to capture as much energy as possible, but it must also correct for phase errors that will be at the paraxial focus. Correcting for these phase errors can be accomplished several ways, including designing a sub reflector system that forces the path length traveled by an incoming ray to be the same as any other incident path length [5] [28], designing a continuous line source oriented along the paraxial [29], or designing a 2-Dimensional reconfigurable phased array. Each of these feeding structures would provide a feasible solution; however, they will not be explored in this thesis.

The final result from this plane wave analysis is the steering limitations for the spherical reflector. As stated previously, steering the antenna beam for the spherical reflector will be performed by moving the feeding structure. Because the spherical reflector is symmetric and does not have a single focal point, this method of steering is valid. Also, the spherical reflector does not have to be moved for this steering method, removing the need to design complex mechanisms for moving the primary reflector. For brevity, no plots of the received energy are given for this result due to the number of plots resulting. However, limiting the feeding structure to 10 meters by 10 meters in size led to the steering limitations of $\pm 15^\circ$ for azimuth and $\pm 5^\circ$ in elevation. The assumption made for imposing this limitation is that the resulting phase errors at any angle within the constraints can be corrected in the feeding structure to ensure that maximum energy is received. The sky study originally presented in

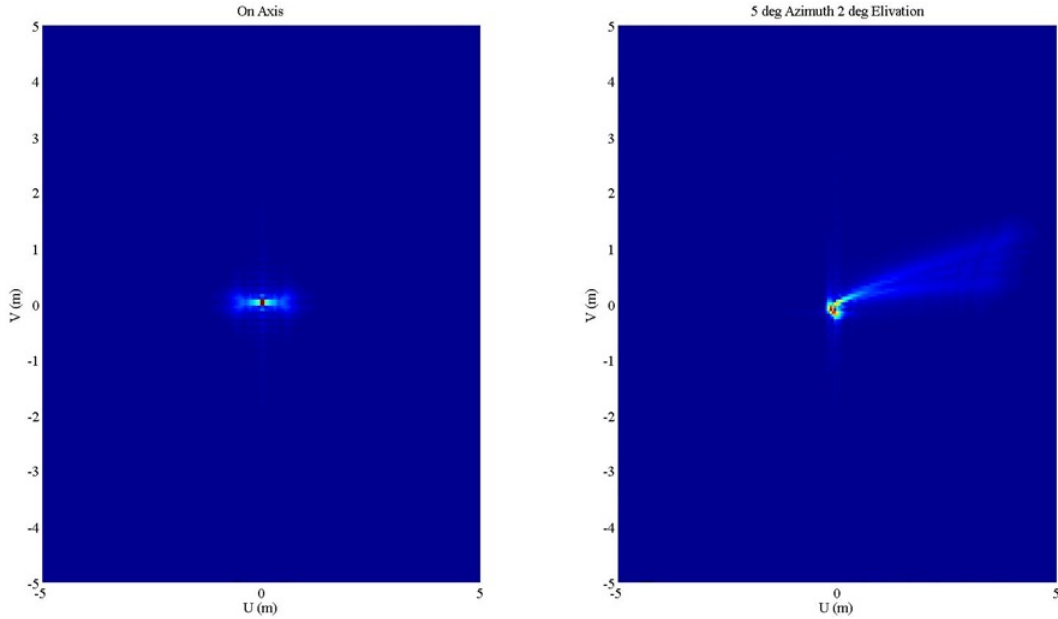


Figure 4.6: Left: On-axis propagation, no blockage amplitude distribution calculated using FKDI Analysis; Right: Tilted propagation at 5° azimuth and 2° elevation, no blockage amplitude distribution calculated using FKDI Analysis

Section 3.3 uses the imposed steering limitation from this section. The results from the sky study are presented in Section 4.3.

4.2.2 Cross-shaped, Parabolically Contoured Reflector Geometry.

Following the method presented in Section 3.2.2, the FF radiation pattern for the sparse reflector is shown in Figure 4.7 from two angles. Again, this plot is generated using a pattern addition post processing step in MATLAB® operating on data from two SatCom™ simulations. The individual sets of arms of the sparse reflector are simulated separately due to the limitation in SatCom™ analyzing custom-shaped reflector antennas.

As expected, the sparse reflector FF radiation pattern shows a large amount of energy directed along the arms of the reflector surface (left hand plot of Figure 4.7). Between the arms little to no energy is being directed. The boresight of the antenna or the main beam has a First Null Beam Width (FNBW) that measures $\approx 0.8^\circ$ making for a narrow “pencil

beam” with a directivity of 50.58 dB. These are good results and expected because the sparse reflector is a large parabolically contoured reflector. Parabolically contoured reflector antennas are highly directional, as shown in literature [2] [4] [6] [8]. In particular, the larger a reflector becomes, the narrower the main beam becomes. Steering a parabolically contoured reflector is accomplished by moving the primary reflector and its feeding structure in unison to keep the feeding structure at the focal point of the reflector. Therefore, for the sparse reflector, steering is to be accomplished by moving the reflector and its feeding structure together.

The right hand plot, in Figure 4.7, shows a very large back lobe. This back lobe is quantified using the front to back ratio figure of merit calculated as:

$$(F/B)_{ratio} = U(0, \phi)_{dB} - U(\pi, \phi)_{dB}, \quad (4.1)$$

where $U(\theta, \phi)_{dB}$ is the FF radiation pattern function in dB. The evaluation at $\theta = 0$ and $\theta = \pi$ indicate evaluation at the front and back respectively. Using Equation (4.1), the front to back ratio for the sparse reflector is 37.32 dB. This will be later compared to the baseline antenna system in Section 5.4.

Feeding the sparse reflector with a plane wave results in a uniform illumination of the entire circular cross-section of the sparse reflector. This illumination includes the arms of the reflector and the blank areas between the arms, resulting in a large amount of energy passing by the reflector. In addition, the sparse reflector has an increased amount of edge surface area as opposed to a filled reflector causing additional diffraction to occur. This additional diffraction means that more energy bends around the edges and therefore passes by the reflector. It is concluded that the large backlobe shown in Figure 4.7 is caused collectively by energy that is not incident on the sparse reflector and energy that diffracts around the edges of the sparse reflector. Figure 4.7 further confirms this conclusion because the cross-section of the sparse reflector is outlined in the back lobe.

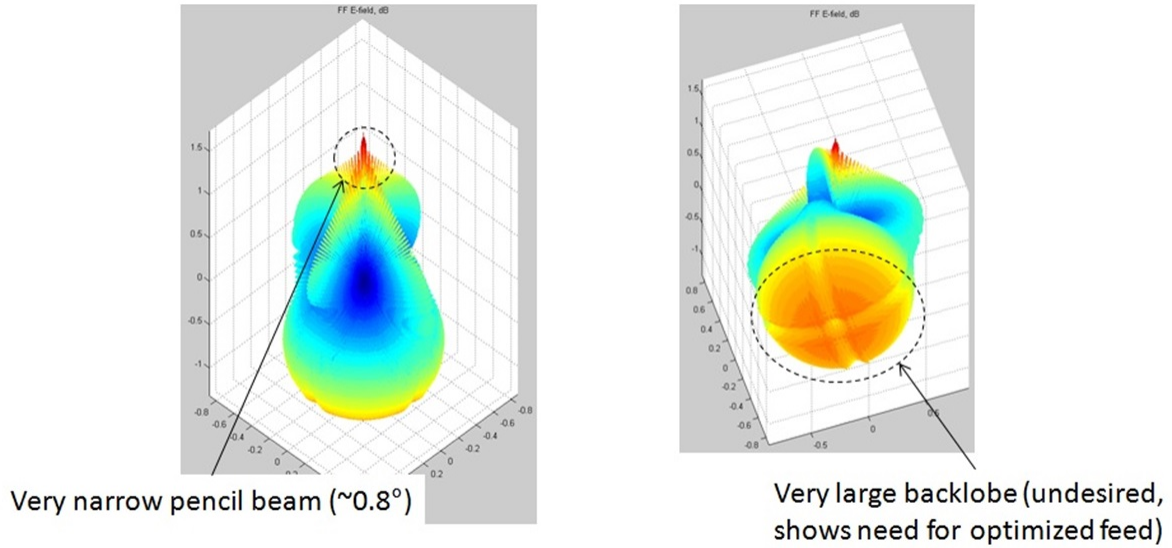


Figure 4.7: FF radiation pattern for the sparse reflector, in dB, with plane wave incident. Plot generated using MATLAB[®] and data generated by SatCom[™]

The results of the plane wave analysis of the sparse reflector clearly show that the sparse reflector must have a feeding structure that is optimized in order to be used effectively. Optimization, in this context, means that the feeding structure must direct more energy towards the arms of the sparse reflector and less energy towards the blank areas. Then in receive mode, by reciprocity, the incident energy upon the sparse reflector will be better received because the feeding structure is focused more towards where the sparse reflector focuses energy. This increases the aperture efficiency of the overall sparse reflector system. By the analysis presented here, the two feeding structure ideas presented in Section 3.5 were generated. The cross-shaped aperture feeding structure is examined in this thesis and the results are in Section 4.5.

4.3 Sky Study for the Rectangular Shaped, Spherically Contoured Reflector

In Section 3.3 the sky study is introduced. This section details the results and implications from the sky study. Figure 4.8 shows a view of the Continental United States (CONUS) with several points labeled. These include: Seattle, Los Angeles, Roswell,

Miami, and Albany. There is no expectation that such locations can sustain an antenna system such as the spherical reflector antenna, but the particular latitude of these sites is the key point to note. The longitude is also relevant, but can be varied more without causing additional sites to be needed. The sites labeled in Figure 4.8 follow a ‘U’ shaped pattern across the CONUS. This shape shows that as the azimuthal steering angle tends towards the horizon, the latitude of the antenna location should be increased to better aid in steering. This relationship is observed because as an antenna location shifts up in latitude, its elevation angle must be closer to the horizon to view the Geosynchronous (GEO) satellite belt and the distance between the antenna and the GEO satellite belt increases. This downward looking angle and increased distance causes a reduction in the azimuthal and elevation steering angular ranges. Specifically, the stations closer to the coast have a higher latitude to incorporate the satellites over the ocean within their azimuthal constraint of $\pm 15^\circ$ and the stations towards the middle of the CONUS are lower in latitude to accommodate more satellites directly above them within the same azimuthal constraint. Also, the stations higher in latitude can view GEO satellites that trace out a larger analemma by looking downward on the GEO satellite belt. Therefore, placing the stations at the particular latitudes shown accommodated nearly all of the GEO satellites over the CONUS. Each of the antenna locations in Figure 4.8 is limited in its viewing range by the steering constraints determined from the plane wave analysis. Entering locations into the Systems Tool Kit (STK) software package and experimenting their placements, five locations were needed to ensure nearly all GEO satellites were in view of one or more spherical reflector antennas.

Figure 4.9 shows a constrained plot of the results from the sky study. In this graphic, the GEO satellite belt is plotted with a line segment drawn to each satellite from the corresponding intended viewing location. Note also that two satellites are omitted. Removing these two satellites is justified to have the spherical antenna remain within its design constraint of 91.44 meters in height. The satellites that are removed trace out a

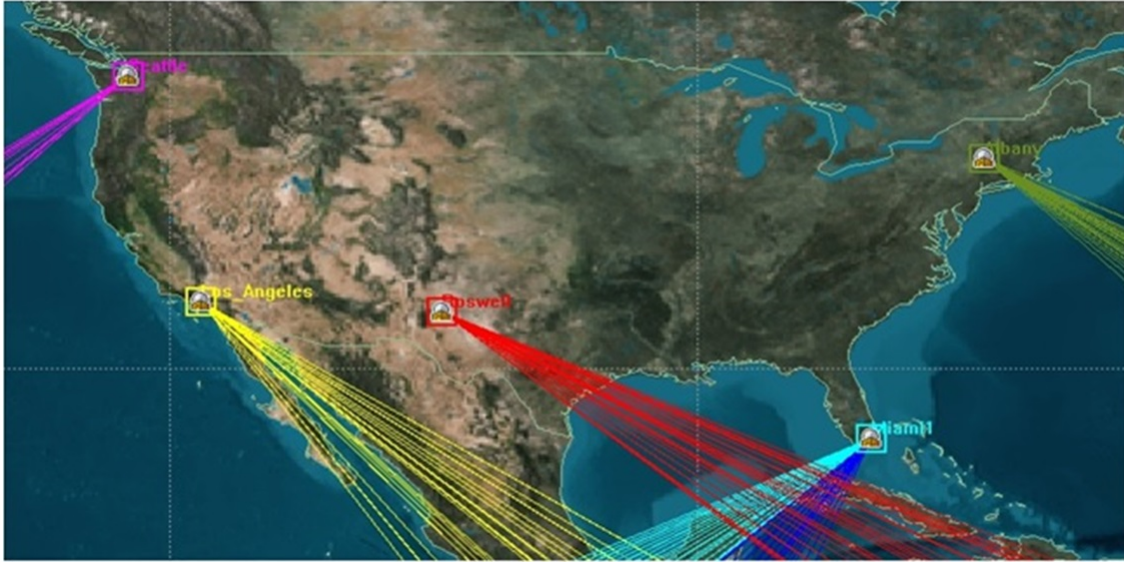


Figure 4.8: Resulting layout of locations needed to use the spherical reflector to communicate with all GEO satellites over the CONUS. Note that the specific latitudes of these locations is of interest and the city names are merely for reference.

very large analemma pattern throughout the year which causes them to be impossible to steer the spherical reflector, while maintaining the spherical reflector dimensions previously presented.

Finally, the criss-cross pattern of viewing angles from the antenna locations is important to stay within the azimuthal limitation from the plane wave analysis and the dimensions of the spherical reflector.

4.4 Baseline Calculation for the Cross-shaped, Parabolically Contoured Reflector Geometry

Figure 4.10 shows a 2-Dimensional planar section of the FF radiation pattern of the L-Band Horn antenna designed in Section 3.4. This pattern results from the SatComTM simulation of the L-Band horn antenna at 1.5 GHz. The left hand plot is the magnitude plot in dB, normalized to the maximum directivity and the right hand plot is the phase plot. The black lines are the electric FF and the fuchsia lines are the magnetic FF.

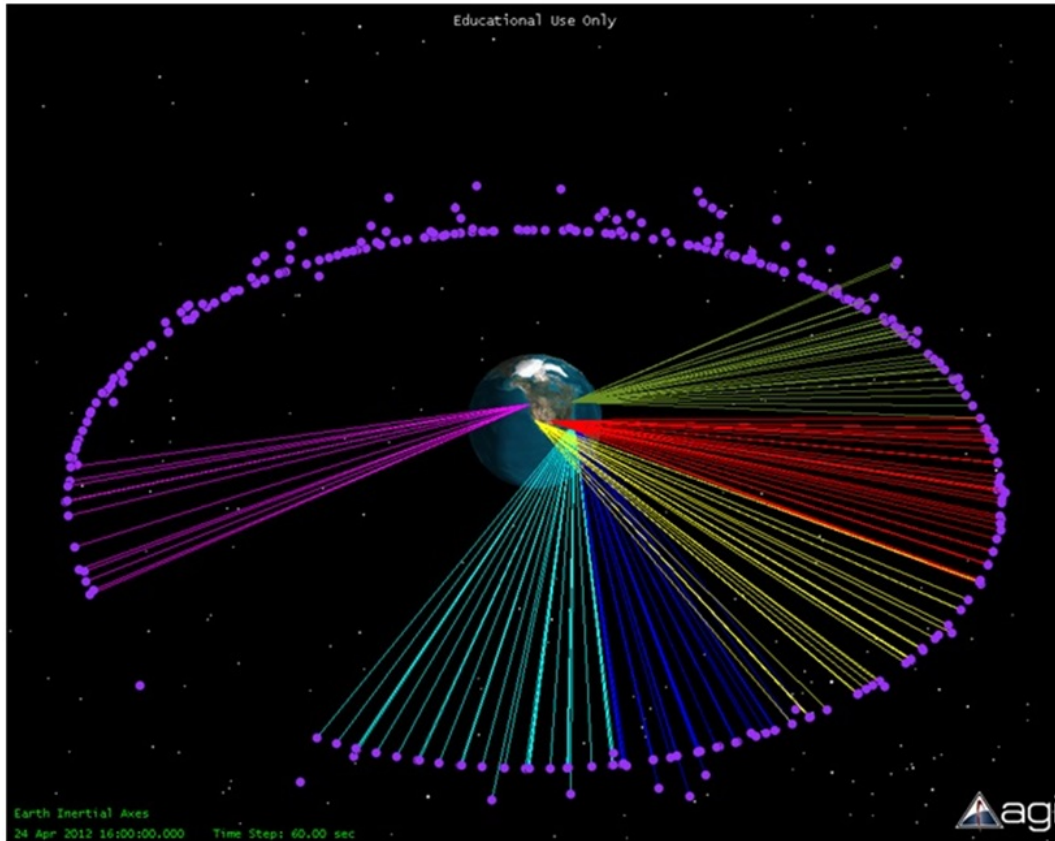


Figure 4.9: Resulting layout of locations needed to use the rectangular shaped, spherically contoured reflector to communicate with all GEO satellites over the CONUS. This is shown to illustrate the criss-crossing view angles from each antenna location

The FF plots for the L-Band horn show a Half Power Beam Width (HPBW) that corresponds well to the secondary reflector shown in Figure 4.11. There is no section of the secondary reflector that is not illuminated by the L-Band horn. Also, the phase plot in Figure 4.10 shows a smooth phase progression over the HPBW which is acceptable in analyzing the baseline antenna system. Had the design not been carried out properly, phase errors may have been present that would cause destructive interference resulting in a reduction in energy received or transmitted. Finally, it is shown that no cross-polarization term is present in the FF radiation pattern of the L-Band horn antenna from the lack of a dashed line in the plot. This means that all energy radiated by the antenna holds a constant

polarization as expected. Having no cross-polarization term in the L-Band horn antenna FF radiation pattern eliminates the possibility of cross-polarization problems caused by the feeding structure of the baseline antenna system.

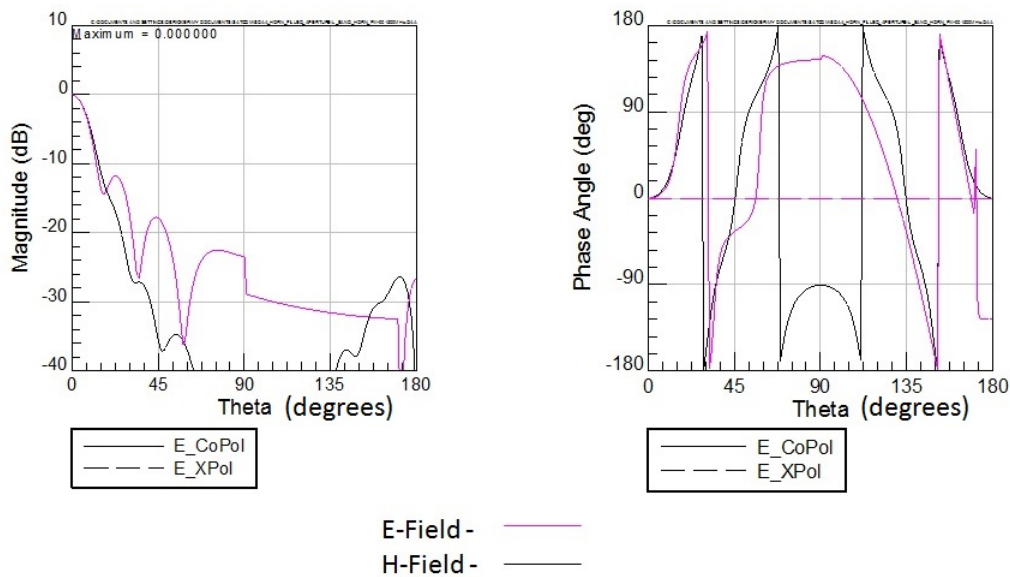


Figure 4.10: FF radiation pattern 2-Dimensional planar cut for the L-Band Horn antenna designed for the baseline antenna system in Section 3.4

The FF radiation results of the L-Band horn antenna generated from SatCom™ are used as the feeding structure for the baseline antenna system or the filled reflector. A wire frame drawing of the filled reflector with its secondary reflector is shown in Figure 4.11 with ray-tracing to visualize the qualitative performance of the antenna system before proceeding to the full simulation. This particular model is an idealized model omitting mounting structures and other blockages. However, the ability to add arbitrary blockages is possible in SatCom™ and will be explored further in the follow-on work to this thesis.

Simulating the filled reflector antenna system with the L-Band horn antenna yields the FF radiation pattern shown in Figure 4.12. As opposed to the results from the L-Band horn

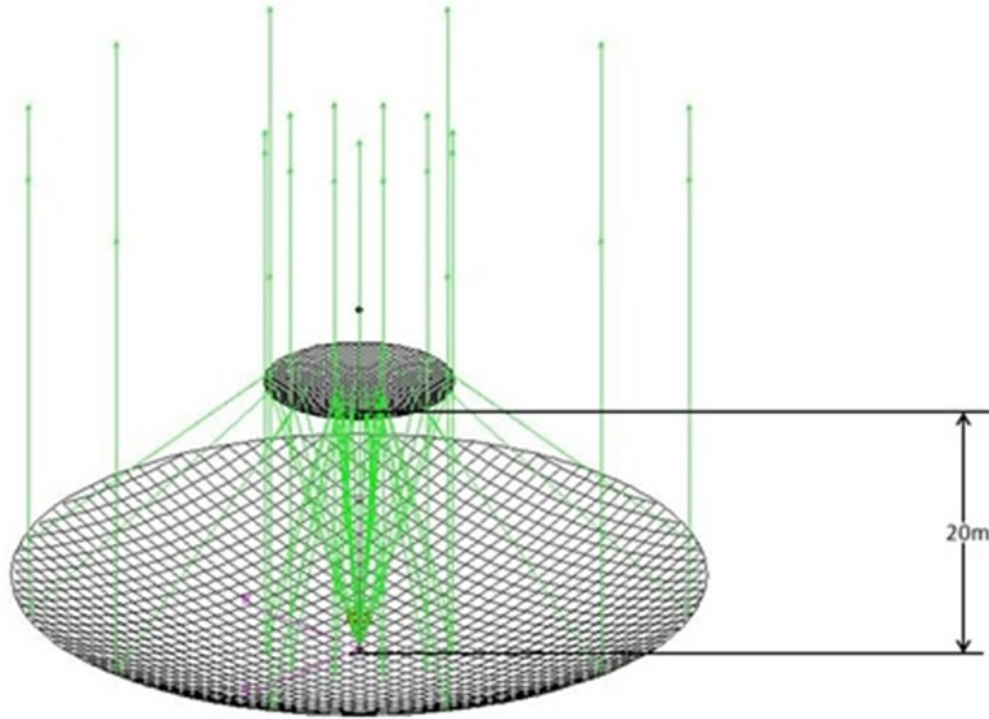


Figure 4.11: Wire frame view of the 50 meter diameter circular, parabolically contoured reflector used as the baseline antenna system for the sparse reflector. Graphic generated using SatComTM

antenna, the FF radiation pattern is not normalized to the maximum value and the electric FF is shown only. However, the magnetic FF would be similar to the electric FF differing only in polarization because the magnetic field is always orthogonal to the electric field. Figure 4.12 shows a high directivity of the antenna system with a 41.43 dB peak in the main beam, a FNBW that is $\approx 0.4^\circ$, and a front to back ratio of 55.92 dB. Another important aspect to note in Figure 4.12 is that the electric FF is mainly comprised of a θ component denoted by the solid line in Figure 4.12 and the phase over the FNBW is relatively flat for the electric FF. A flat phase is desirable to mitigate any unwanted destructive interference that may occur as a result of phase deviations or errors.

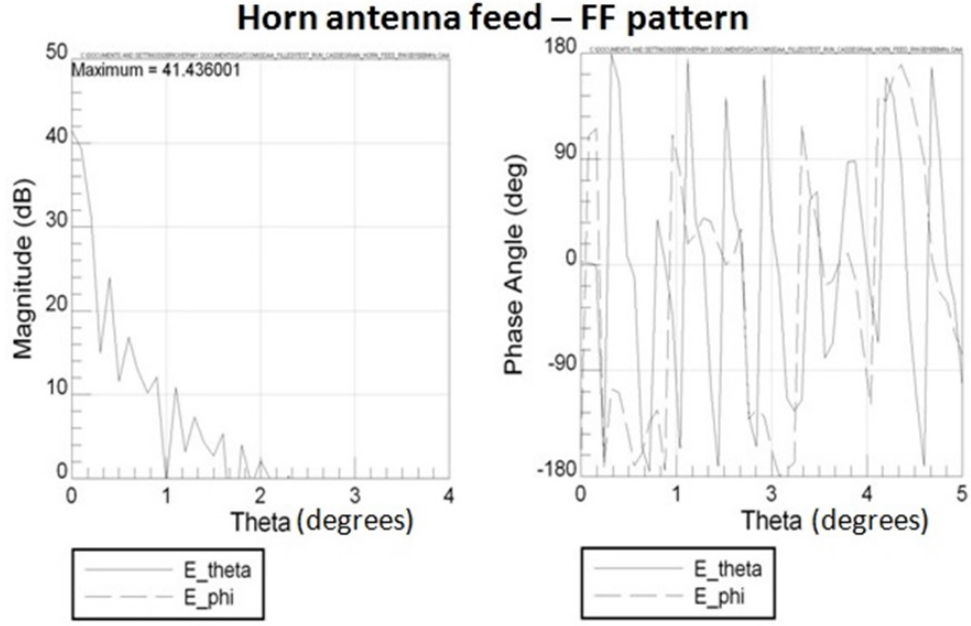


Figure 4.12: FF radiation pattern 2-Dimensional planar cut for the baseline antenna system fed by the L-Band Horn antenna shown in Figure 3.10

4.5 Feed Design for the Cross-shaped, Parabolically Contoured Reflector Geometry

The first set of results presented here are from applying the method shown in Section 3.5 on a square aperture as a test case. Figures 4.13 and 4.14 show the output mode shapes from the code for the first 10 modes. These correspond well to the analytical solutions shown in [26]. The mode struck out with an 'X' in Figure 4.14 indicates an invalid mode (i.e. TE_{00}). For the modal distribution plots generated in this thesis, the use of the MATLAB[®] `eigs()` merited a numerical fix in the post processing of the eigenvectors. In particular, a weighted sum is used where two modes share a common cutoff frequency. This is required because if two distributions output by the `eigs()` function share the same eigenvalue, the modal plots would consistently show a slight skew to them. The skew was arbitrary because the eigenvectors are not unique. Therefore, shifting the plots on-axis by applying a weighted sum is valid because it is a linear operation using the eigenvectors generated by the `eigs()` function.

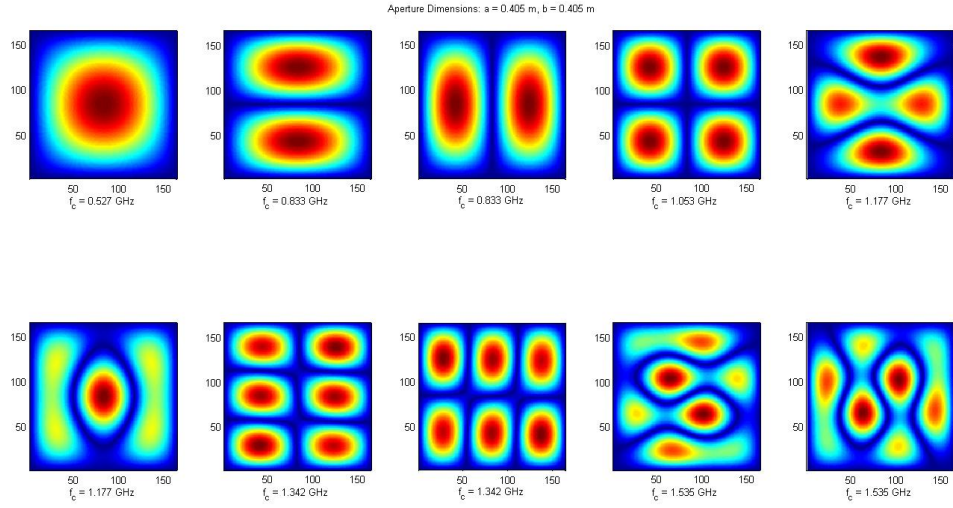


Figure 4.13: First 10 TM^z approximated modes, square aperture, $N = 165$

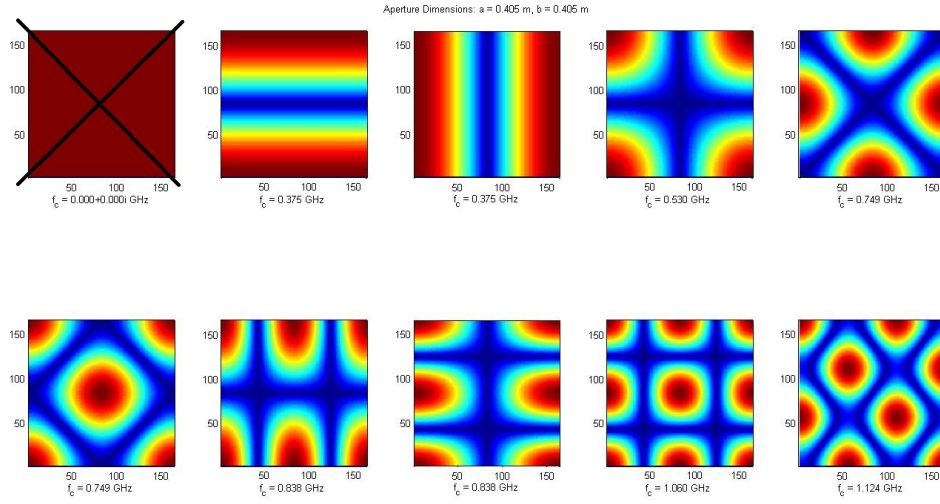


Figure 4.14: First 10 TE^z approximated modes, square aperture, $N = 165$

Table 4.2 summarizes the results for Figures 4.13 and 4.14 by showing the cutoff frequencies from the eigenvalues for the same square apertures computed numerically and

Table 4.2: Cutoff frequencies for first 10 TM^z and TE^z modes respectively, Aperture dimensions $a = b = 0.405m$

TM _{mn}	Numerical Cutoff (GHz)	Analytical Cutoff (GHz)
TM ₁₁	0.526	0.523
TM ₂₁	0.832	0.827
TM ₁₂	0.832	0.827
TM ₂₂	1.053	1.046
TM ₃₁	1.177	1.170
TM ₁₃	1.177	1.170
TM ₃₂	1.342	1.334
TM ₂₃	1.342	1.334
TM ₄₁	1.535	1.526
TM ₁₄	1.535	1.526
TE_{mn}		
TE ₀₀	–	–
TE ₁₀	0.374	0.370
TE ₀₁	0.374	0.370
TE ₁₁	0.529	0.523
TE ₂₀	0.749	0.740
TE ₀₂	0.749	0.740
TE ₂₁	0.837	0.827
TE ₁₂	0.837	0.827
TE ₂₂	1.059	1.046
TE ₃₀	1.123	1.110

analytically. The analytical cutoff frequencies are calculated using Equation (4.2) from [16]:

$$(f_c)_{mn} = \frac{1}{2\pi \sqrt{\mu\epsilon}} \sqrt{\left(\frac{m\pi}{a}\right)^2 + \left(\frac{n\pi}{a}\right)^2}. \quad (4.2)$$

The final check for the methodology is the FF radiation pattern calculations. The test case of a $3\lambda \times 3\lambda$ aperture with a uniform field distribution is shown in Figure 4.15, where

the FF radiation pattern of the square aperture is shown in dB. The 2-Dimensional plot is the $\phi = 0, 0 \leq \theta \leq \pi/2$ planar cut of the overall FF radiation pattern. A large main lobe is centered about the z -axis, which is considered as the $\theta = 0$ axis, followed by first side lobes ~ 13 dB down from the main lobe. This agrees with current literature and therefore validating the method for calculating the FF radiation pattern of an aperture in this thesis [2]. It is important to note that from the use of Love's Equivalence Principle, the FF radiation pattern is valid only in the $+z$ -direction. The plot in Figure 4.15 shows this valid region because it omits any field calculations in the $-z$ -direction, or where $|\theta| > \pi/2$.

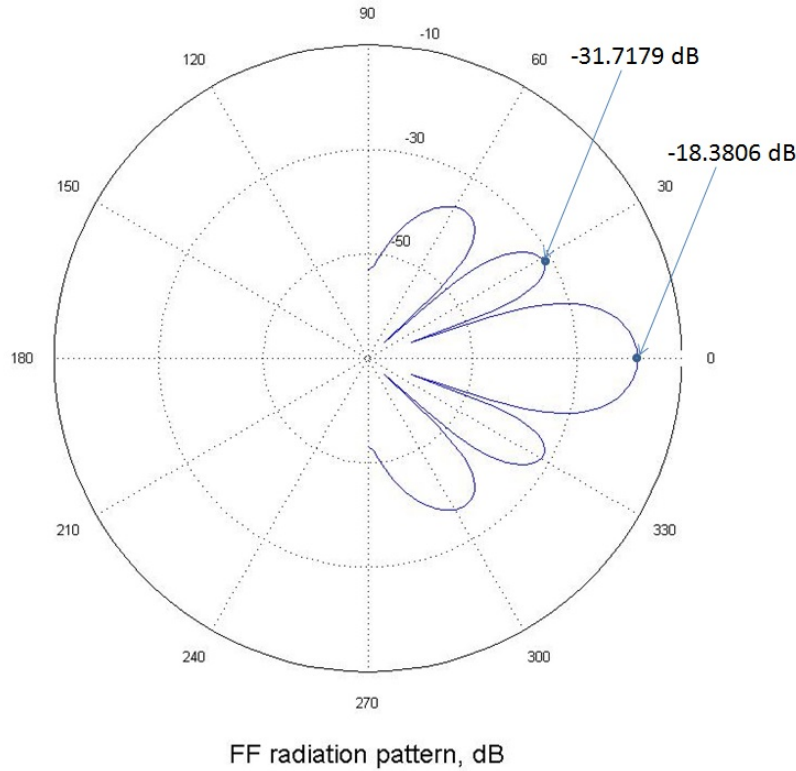


Figure 4.15: $\phi = 0, 0 \leq \theta \leq \pi/2$ planar cut of FF radiation pattern, in dB, of a $3\lambda \times 3\lambda$ square aperture excited by a uniform field distribution

Having tested the methodology using a known test case and proving it to be valid, the next step is to simulate the cross-shaped aperture. As stated previously in Chapter 3,

the expectation for the cross-shaped aperture is to mitigate the amount of energy directed towards the regions between the arms of the sparse reflector. Figure 4.16 illustrates this concept by showing a cross-shaped aperture of unknown dimensions suspended above the sparse reflector. The dashed lines indicate where the cross-shaped aperture antenna beams need to be focused. As stated earlier, the inverse Fourier relationship between the spatial dimensions of an aperture antenna and its directivity in the FF pattern is the reason to explore the use of the cross-shaped aperture as a feeding structure for the sparse reflector [2] [6].

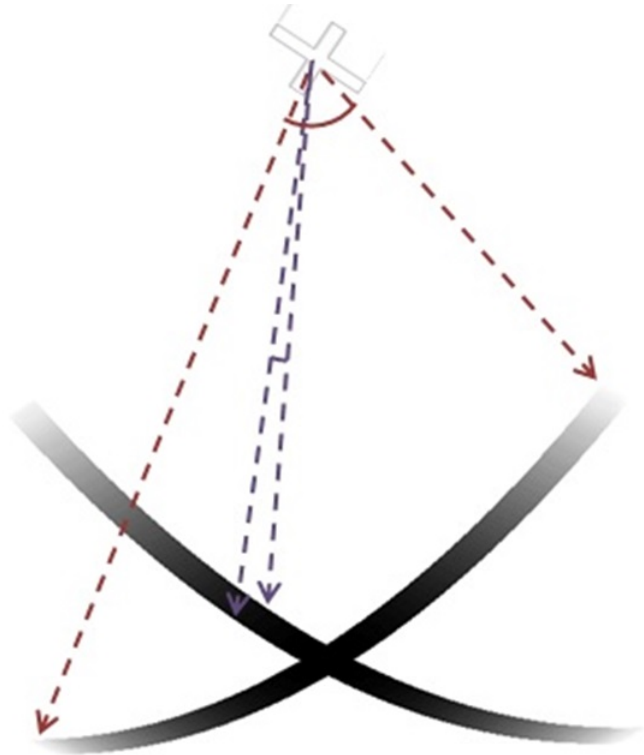


Figure 4.16: Graphic showing the cross-shaped aperture feeding structure suspended above the sparse reflector. The cross-shaped aperture is intended to avoid illuminating the regions between the sparse reflector arms

Figures 4.17 and 4.18 show the resulting longitudinal field distributions for the first 10 modes of the TM^z and TE^z cases respectively. The results exhibit noticeable patterns

that resemble the mode distributions of the square aperture, which was unexpected. Further analysis will be needed to determine which mode is the best choice for exciting the cross-shaped aperture feeding structure, but for this thesis, only the lowest order modes are considered. Particularly, because the use of the lowest order modes is a typical approach to feeding aperture antennas and the cutoff frequencies for the lowest order modes allow the use of L-Band frequencies. However, the TM mode has a cutoff within the L-Band which means it constrains the frequency range to only the upper portion of L-Band.

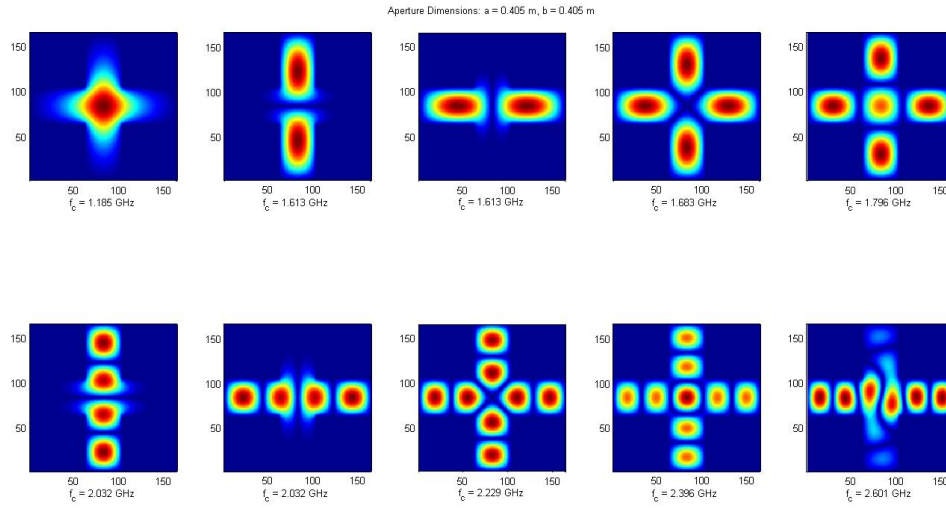


Figure 4.17: First 10 TM^z approximated modes, Cross-Aperture, $N = 165$

The final plots in Figures 4.19 - 4.22 show the FF radiation pattern cuts of the cross-shaped aperture excited by the lowest order TM^z and TE^z modes respectively. As before, the particular planar cut is the $\phi = 0$, $0 \leq \theta \leq \pi/2$ plane for Figures 4.19 and 4.20, however the planar cut for Figures 4.21 and 4.22 is the $\phi = \pi/4$, $0 \leq \theta \leq \pi/2$ plane. It is important to note that from the use of Love's Equivalence Principle, these FF radiation patterns are valid

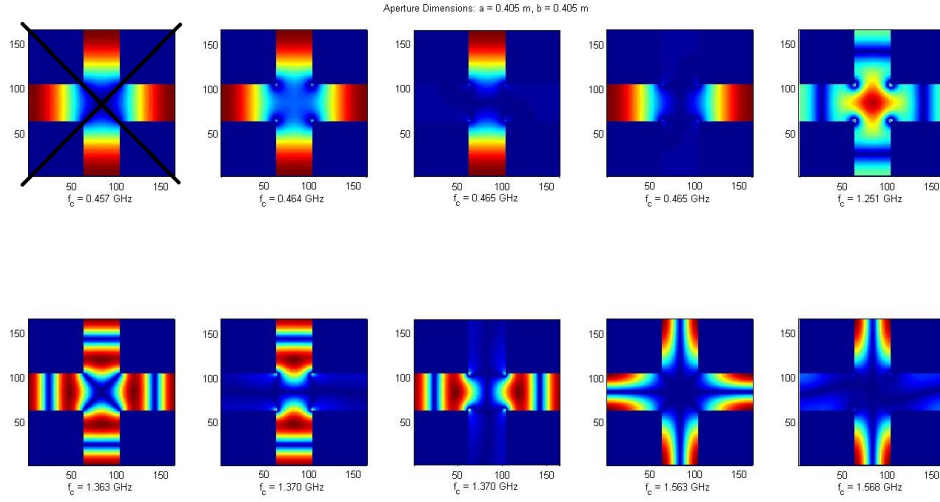


Figure 4.18: First 10 TE^z approximated modes, Cross-Aperture, $N = 165$

only in the $+z$ -direction. The plots in Figures 4.19 - 4.22 show this valid region by omitting any field calculations in the $-z$ -direction, or where $|\theta| > \pi/2$.

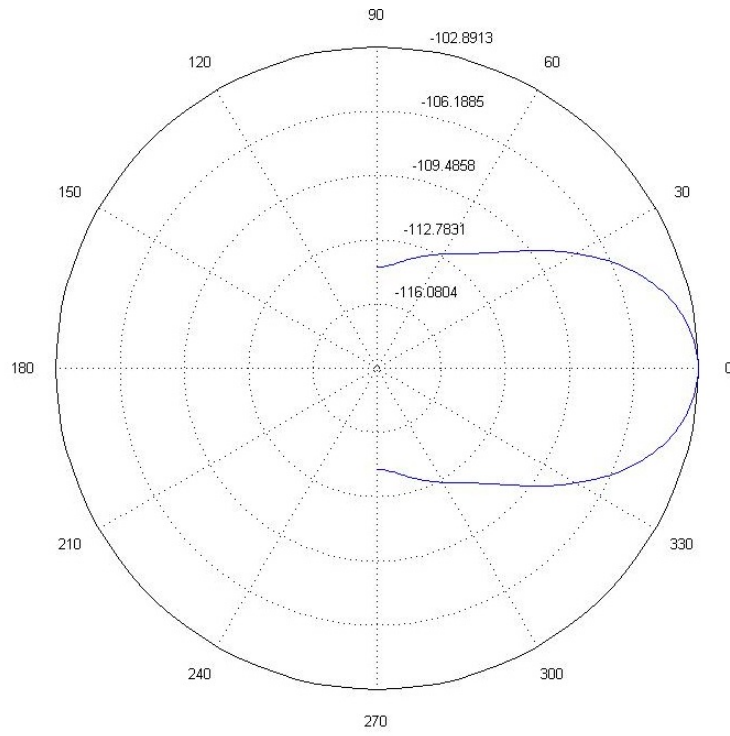
Comparing the FF radiation pattern of the square aperture to the cross-shaped aperture, it is apparent that the amount of energy output from the cross-shaped aperture is much less than the amount output from the square aperture. This reduction in energy is an expected result due to the reduction in physical cross-sectional area and the conservation of energy principle [2].

Another noticeable difference between the two apertures' FF radiation patterns is reduction in side lobes in the cross-shaped aperture pattern. This reduction is attributed to again the smaller physical cross-sectional area because it has been shown previously that increasing the physical size of an aperture increases the amount of side lobes [2]. In the cross-shaped aperture case, the dimensions are being reduced from the square aperture meaning less side lobes are present in the FF radiation pattern.

Another major difference between the patterns is the main lobe shape. The main lobe of the FF radiation pattern of the square aperture shown in Figure 4.15 has a fairly narrow shape with a FNBW of approximately 40° . In contrast, the FF radiation pattern of the cross-shaped aperture excited with a similar mode shown in Figure 4.19 exhibits a very wide main lobe with a FNBW of approximately 60° . This FNBW is expected because the original dimensions for the aperture are formulated based on the need of a wider FNBW. Further investigation is needed to determine which mode is optimal for the cross-shaped aperture. In addition, the FF radiation plot for the lowest order TM mode in the cross-shaped aperture is shown in Figure 4.20. However, the FF radiation pattern plot for the TM_{11} mode in the square aperture is not generated due to its poor performance leaving no comparing plot for Figure 4.20. In future work, it is still a possibility that a TM mode may produce the optimal FF radiation pattern for the sparse reflector and thus will not be ruled out. However, for this thesis, using a TM mode for exciting the cross-shaped aperture is not explored further.

Finally, the additional planar cuts of the FF radiation patterns for the cross-shaped aperture are included here to show how the aperture performs in the blank regions between the reflector arms. The pattern for the TE case shows a less directive pattern than the $\phi = 0$ cut, but still with more energy focused towards the center part of the reflector as expected. However, there are added side lobes that are unexpected. These are attributed to the smaller dimension of the aperture across the $\phi = \pi/4$ planar cut. The TM case shows an omnidirectional pattern which was unexpected and confirms that the lowest order TM mode is not a good choice for exciting the cross-shaped aperture.

From these plots, a TE mode exciting the cross-shaped aperture appears to be the best choice. However, more design iterations are needed to optimize the FF radiation pattern of the cross-shaped aperture antenna for feeding the sparse reflector. In particular, the cross-shaped aperture dimensions should be optimized with a particular TE or TM mode or mode combination.



FF radiation pattern $\phi = 0$ planar cut, dB

Figure 4.19: $\phi = 0$, $0 \leq \theta \leq \pi/2$ planar cut of FF radiation pattern, in dB, of cross-shaped aperture excited by lowest order TE^z mode

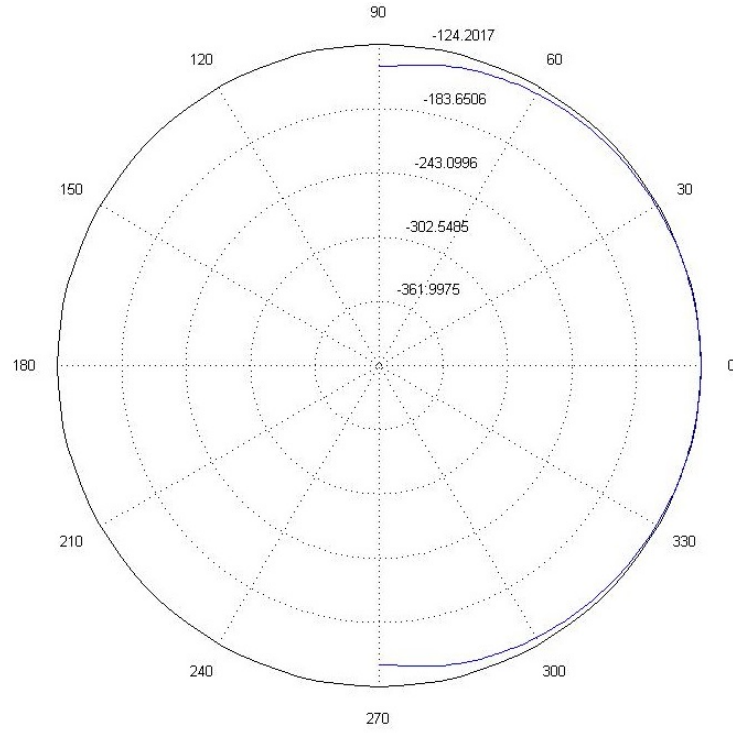
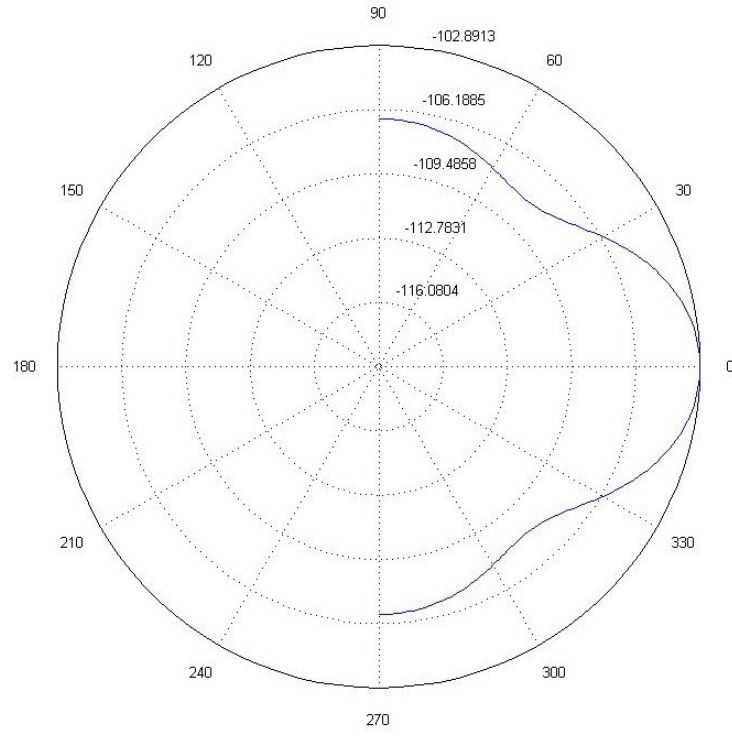
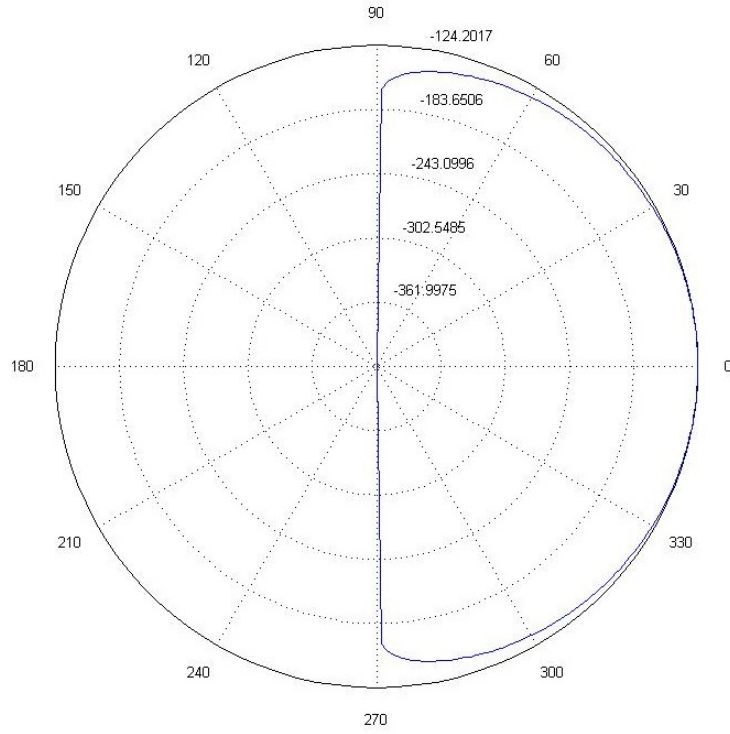


Figure 4.20: $\phi = 0$, $0 \leq \theta \leq \pi/2$ planar cut of FF radiation pattern, in dB, of cross-shaped aperture excited by lowest order TM^z mode



FF radiation pattern $\phi = \pi/4$ planar cut, dB

Figure 4.21: $\phi = \pi/4$, $0 \leq \theta \leq \pi/2$ planar cut of FF radiation pattern, dB, of cross-shaped aperture excited by lowest order TE^z mode



FF radiation pattern $\phi = \pi/4$ planar cut, dB

Figure 4.22: $\phi = \pi/4$, $0 \leq \theta \leq \pi/2$ planar cut of FF radiation pattern, in dB, of cross-shaped aperture excited by lowest order TM^z mode

V. Discussion

In summary, this research has examined two electrically large, custom-shaped reflector antennas: a rectangular shaped, spherically contoured reflector (spherical reflector), and a cross-shaped, parabolically contoured reflector (sparse reflector). Both reflectors present a new concept in antenna design because of their size, unconventional cross-sectional shape, and their respective application. In particular, the spherical reflector antenna system is intended to be a earth-based antenna for Geosynchronous (GEO) satellite communications with offset feed beam steering, and the sparse reflector antenna system is intended to be a foldable reflector for easier deployability in a space-based communications application. Pursuing both of these reflector antenna concepts for this thesis was prompted by a discontinuation in the spherical reflector antenna project.

This thesis presents a methodology for designing electrically large custom-shaped reflector antennas based on well known published works. The methodology is systematic and consistent for each reflector antenna except for one distinct procedure for each reflector. These include a sky study for the spherical reflector and a baseline antenna design for the sparse reflector. The need for an additional procedure for each reflector is attributed to the difference in custom-shaping of each reflector and the difference in contour. However, the general methodology is summarized as:

1. Geometrical analysis
2. Plane wave analysis
3. Feed antenna design
4. Feed antenna analysis

For the spherical reflector, procedures one and two listed above are applied. For the sparse reflector, all procedures are applied. The sections that follow summarize the results of each step in the methodology for each reflector antenna and provide conclusions based on the findings.

5.1 Geometrical Analysis

Analysis of the spherical reflector geometry shows the only degree of freedom is the radius of curvature. This is because the height and width of the rectangular cross-section are specified. In order to accommodate design changes in the simulation code, the known dimensions are related to the radius of curvature. The chord length of a circle is analogous to the known dimensions of the spherical reflector and thus the expression for the chord length of a circle is used to relate the radius of curvature to the known dimensions. This relationship is used in defining the spherical reflector in computer simulations for ray-tracing and plane wave analysis.

The sparse reflector geometry has been predetermined for deployability and therefore does not have any degrees of freedom. Geometrical analysis is required however, because the sparse reflector has a complex cross-sectional shape that must be specified in computer simulations from the field data generated in geometrical analysis. In particular, the parabolic contour of the sparse reflector and the angles subtended by the sparse reflector are determined from geometrical analysis. These field data are then used in performing ray-tracing and plane wave analysis.

5.1.1 Ray-Tracing Procedure: Rectangular Shaped, Spherically Contoured Reflector.

The results from performing the ray-tracing for the spherical reflector illustrate the formation of a caustic envelope. The caustic envelope formation is attributed to the inherent spherical aberrations as described in [1]. However, using a radius of curvature that is 60.96 meters in length, determined from the later plane wave analysis, caused a relatively smaller caustic to form as opposed to the caustic shown in Section 2.1 and [5]. Therefore, a complex feeding structure, such as the dual Gregorian reflector system that feeds the Arecibo radio astronomy antenna, can be avoided for the spherical reflector because the aberrations are not as prominent. Finally, the ray-tracing procedure confirms that steering the main beam

of the spherical reflector can be accomplished by moving the feeding structure due to the symmetry of the spherical reflector.

5.1.2 Ray-Tracing Procedure: Cross-shaped, Parabolically Contoured Reflector Geometry.

The ray-tracing procedure for the sparse reflector confirms that the focal point forms at a distance of 80 meters from the apex of the reflector. In addition, the procedure confirms that the feeding structure for the sparse reflector is best placed at the focal point which leads to the conclusion that in order to steer the antenna beam, the sparse reflector and its feeding structure must be moved in unison. Moving the feeding structure away from the focal point will cause a reduction in the amount of energy received.

5.2 Plane Wave Analysis

Because the two reflectors examined in this thesis exhibit different contours, the feed placement for each reflector is different. This dissimilarity between the two reflectors leads to the use of different procedures for plane wave analysis. The methods are explained previously in Section 3.2 and the conclusions from each follow. The results from the plane wave analysis of each reflector provide field data used in the feeding structure design.

5.2.1 Rectangular Shaped, Spherically Contoured Reflector.

The general procedure for the spherical reflector plane wave analysis is to first, propagate a plane wave towards the spherical reflector, and second, place an image plane at the paraxial focus, or where the reflected energy is centered, to visualize the amplitude distribution of the received energy. Two approaches are taken to calculate the amplitude distribution at the paraxial focus: the Fourier transform method and the Fresnel-Kirchoff Diffraction Integral (FKDI) method.

The Fourier transform method does not result in an accurate representation of the amplitude distribution at the paraxial focus. It does not account for diffraction as the FKDI method does. However, the Fourier transform method confirms that as the incident angle of

the plane wave is shifted off-axis, the amplitude distribution at the paraxial focus shifts as well. This shift confirms that steering the antenna can be accomplished from moving the feeding structure.

The FKDI method shows a more accurate representation of the amplitude distribution at the paraxial focus because the diffraction effects are modeled. The on-axis plane wave shows an amplitude distribution with minimal energy spreading, but the spreading effect becomes more noticeable as the plane wave angle of incidence shifts off-axis. To capture the spreading energy, a feeding structure that is 10 meters by 10 meters will be used. Also, the steering will be limited to $\pm 15^\circ$ in azimuth and $\pm 5^\circ$ in elevation.

5.2.2 Cross-shaped, Parabolically Contoured Reflector Geometry.

As stated earlier, the feed placement was determined to be the focal point of the sparse reflector. Also, there are no inherent aberrations exhibited by the sparse reflector. Therefore, the plane wave analysis for the sparse reflector is performed in the transmit mode as opposed to the receive mode. This is a valid approach because of the reciprocity of antenna patterns [2] [6]. Defining an analytical Far-Field (FF) radiation pattern for a feeding structure to uniformly illuminate the sparse reflector is analogous to a plane wave incident upon the sparse reflector and therefore, the overall FF radiation pattern is obtained.

The FF radiation pattern of the sparse reflector confirms that a “pencil beam” forms as is typical for a parabolically contoured reflector. Also, its highest directivity is in the boresight, or directly out in front of the reflector. However, the feeding structure for the sparse reflector must direct energy more towards the arms of the sparse reflector and less energy towards the blank areas between the arms. Ultimately, the performance of the sparse reflector will be improved from the added directivity of the feeding structure because energy will not be directed towards the blank areas between the reflector arms. Particularly, a higher directivity and narrower FNBW will result and the sparse reflector performance will better match the baseline antenna performance.

5.3 Sky Study for the Rectangular, Spherically Contoured Reflector

Using publicly available Two Line Element (TLE) data from www.space-track.org and Systems Tool Kit (STK) software from Analytical Graphics Inc. (AGI), the sky study is performed [25]. In particular, all publicly available Geosynchronous (GEO) satellite data are imported into STK and plotted to visualize the regions of the sky that the spherical reflector must have line of sight for. In order to accommodate all GEO satellites in orbit over the Continental United States (CONUS), a total of five spherical reflector stations across the CONUS are needed. The placement of these stations varies in latitude and longitude, but the more important variable is latitude. Figures 4.8 and 4.9 previously presented show the relative latitudes for the stations.

5.4 Baseline Calculation for the Cross-shaped, Parabolically Contoured Reflector Geometry

The design and simulation of the 50 meter diameter circular shaped, parabolically contoured reflector antenna as a baseline for the sparse reflector is presented in Sections 3.4 and 4.4. The sparse reflector needs to have a directivity close to 41.43 dB, a First Null Beam Width (FNBW) close to 0.4° , and a front to back ratio around 55.92 dB in order to be comparable to the baseline antenna system. From the FF radiation pattern plotted from the plane wave analysis, the sparse reflector has a directivity of 50.58 dB, a FNBW of 0.8° , and a front to back ratio of 37.32 dB. These results show that the sparse reflector is comparable to the baseline antenna system by these figures of merit except for a decrease in the front to back ratio. These figures of merit are summarized in Table 5.1. However, the FF patterns of the reflectors differ and thus the same performance cannot be expected from these antenna systems.

The difference in directivities of the two antennas is attributed to the blockage that occurs from the secondary reflector in the baseline Cassegrain antenna system. Adding the secondary reflector more uniformly illuminates the primary reflector, but blocks incoming

Table 5.1: Summary of results from the Plane Wave Analysis of sparse reflector and baseline antenna simulation

	Sparse Reflector	Baseline Antenna (Analytic Feed Pattern)	Baseline Antenna (Cassegrain system with Horn Feed)
Maximum Directivity (boresight)	50.58 dB	55.70 dB	41.43 dB
FNBW	0.8°	0.4°	0.4°
Front to Back Ratio	37.32 dB	77.03 dB	55.92 dB

signals, thus reducing the maximum directivity of the overall system. However, the aperture efficiency increases from the uniform illumination of the primary reflector. The difference in the front to back ratios is due to the diffraction of energy around the arms of the sparse reflector. This diffraction causes an increased back lobe to form which then decreases the ratio of energy directed towards the front and energy directed towards the back of sparse reflector. The decrease in the front to back ratio is tolerable however and the sparse reflector is expected to be able to perform well with an optimal feeding structure.

5.5 Feed Design for the Cross-shaped, Parabolically Contoured Reflector Geometry

From the methods and results presented in Sections 3.5 and 4.5, the use of a cross-shaped aperture antenna is a feasible option for feeding the sparse reflector. The cross-shaped aperture shows a reduction in output power as compared to a square aperture with similar dimensions. The use of a different mode to excite the cross-shaped aperture may prove feasible in future work to increase the output power. Higher order modes for the cross-shaped aperture show higher concentrations of energy as compared to the lowest order modes used in this thesis.

Also, the FNBW of the cross-shaped aperture is much larger than the square aperture due to the inverse Fourier relationship between the FF radiation pattern and the dimensions of an antenna aperture. The larger FNBW will better illuminate the sparse reflector resulting in an overall higher directivity of the antenna system.

5.6 Future Work

To further the work presented in this thesis, two research directions are of interest for the sparse reflector. These include:

1. Further refining the cross-shaped aperture antenna and simulating it with the sparse reflector.
2. Designing the phased array feeding structure and simulating it with the sparse reflector.

Further refinement of the cross-shaped aperture antenna includes exploring the use of higher order modes to excite the aperture for feeding the sparse reflector, revising the dimensions of the aperture to improve the FF radiation pattern to better direct energy towards the arms of the sparse reflector, and exploring the usage of special materials such as metamaterials and dielectrics to improve the FF radiation pattern.

Designing the phased array and refining it will be the newest focus for this project. The benefits of a phased array are that:

1. The FF radiation pattern of the array may be altered by phasing the individual elements of the array.
2. The array can be reconfigured to alter its performance.
3. The output power is much greater than an aperture antenna.

However, the design of a phased array feeding structure poses a new challenge if the array size gets too large relative to wavelength. In particular, the array will have to be analyzed in segments that are electrically smaller and the results from each segment will then be combined into the overall result for the array.

Appendix: MATLAB Code

A.1 Ray-Tracing Code for Rectangular Shaped, Spherically Contoured Reflector

```
1      % Housekeeping
2      clc;
3      clear all;
4      close all;
5
6      %% Ray-Tracing for Rectangular, Spherically contoured reflector
7
8      % User inputs
9      D.width = 1000;           % Reflector width, ft
10     D.height = 300;           % Reflector length, ft
11     D.R_s = 2000;             % Reflector Radius of curvature, ft
12     N = 10;
13
14     %% Calculations (origin wrt the center of curvature)
15
16     N_w = N;                  % Number of rays across width of dish
17     N_l = N;                  % Number of rays across length of dish
18
19     % Convert to meters
20     D.width = D.width*0.3048;
21     D.height = D.height*0.3048;
22     D.R_s = D.R_s*0.3048;
23
24     % Lay out grid for where each ray will be incident
25     D.theta = linspace(pi/2 + asin(-D.height/2/D.R_s), pi/2 + ...
26         asin(D.height/2/D.R_s), N_l);
27     D.phi = linspace(pi+asin(-D.width/2/D.R_s), ...
28         pi+asin(D.width/2/D.R_s), N_w);
29     [D.THETA,D.PHI] = meshgrid(D.theta,D.phi);
30     [D.X,D.Y,D.Z] = sph2cart(D.PHI,D.THETA-pi/2,D.R_s);
31
32     % Generate geometry
33     figure; hold on
34     % Change camera view to slightly above reflector
35     view([D.R_s,D.R_s/2,D.R_s/2]);
36     % Plot reflector
37     ref = surf(D.X,D.Y,D.Z);
38     % Make it better looking
39     set(ref,'FaceColor',[0.41,0.41,0.41],'EdgeLighting','gouraud');
40     % Plot radius of curvature line and label it
41     quiver3(0,0,0,-D.R_s,0,0,1);
42     text(-D.R_s/2,0,0,'\leftarrow Radius of Curvature = 5000 ft.',...
43         'HorizontalAlignment','left');
44     % Label origin
45     text(0,0,0,'O \rightarrow ', 'HorizontalAlignment','right');
```

```

46 % Plot z axis and label it
47 quiver3(0,0,0,D.width/2,0,0);
48 text(D.height,0,0,'X','HorizontalAlignment','right');
49 % Plot x axis and label it
50 quiver3(0,0,0,0,0,D.height/2);
51 text(0,0,D.height/2,'Z','HorizontalAlignment','right');
52 % Plot y axis and label it
53 quiver3(0,0,0,0,D.height/2,0);
54 text(0,D.height/2,0,'Y','HorizontalAlignment','right');
55 axis equal
56 axis off
57 axis vis3d
58 hold off
59
60 % This plots the center cross section of the RIMSHOT
61 % reflector (XZ plane) Note: The use of X is still the
62 % x axis in these plots, but the use of Z
63 % is the y axis in these plots.
64 THETA = reshape(D.THETA,1,size(D.THETA,1)*size(D.THETA,2));
65 PHI = reshape(D.PHI,1,size(D.PHI,1)*size(D.PHI,2));
66 % Draw 2D geometry
67 [D.twoDX,D.twoDY,D.twoDZ] = sph2cart(pi,D.theta - pi/2,D.R_s);
68 figure;
69 hold on
70 plot(D.twoDX,D.twoDZ);
71
72 % Calculate surface normals
73 N = zeros(3,size(D.THETA,1)*size(D.THETA,2));
74 N(1,:) = D.R_s.*sin(THETA).*cos(PHI); %x
75 N(2,:) = D.R_s.*sin(THETA).*sin(PHI); %y
76 N(3,:) = D.R_s.*cos(THETA); %z
77
78 % % Plot surface normals (XZ plane) for i = 5:10:N_l^2
79 %     quiver(0,0,N(1,i),N(3,i),1,'r','MaxHeadSize',0.02);
80 % end
81
82 % Calculate incident rays
83 I = zeros(3,size(D.THETA,1)*size(D.THETA,2));
84 I(1,:) = D.R_s.*sin(THETA).*cos(PHI);
85 Ipos = zeros(3,size(D.THETA,1)*size(D.THETA,2));
86 Ipos(2,:) = D.R_s.*sin(PHI); %y
87 Ipos(3,:) = D.R_s.*cos(THETA); %z
88
89 % Plot incident rays (XZ plane)
90 for i = 5:10:N_l^2
91     quiver(Ipos(1,i),Ipos(3,i),I(1,i),I(3,i),1, ...
92           'b','MaxHeadSize',0.02);
93 end
94
95 % Calculate reflected rays
96
97 Nhat = N./(ones(3,1)*sqrt(sum(N.^2,1)));

```

```

98
99     % Incoming wave vector (unit vector)
100    D0 = [cos(pi)*sin(pi/2), ...
101          sin(pi)*sin(pi/2), ...
102          cos(pi/2)];
103
104    R = D0'*ones(1,size(N,2)) - ...
105        ([2;2;2]*sum((D0'*ones(1,size(N,2))).*Nhat)).*Nhat;
106
107    R = 1000.*R;
108
109    Rpos = zeros(3,size(D.THETA,1)*size(D.THETA,2));
110    Rpos(1,:) = D.R_s.*sin(THETA).*cos(PHI); %x
111    Rpos(2,:) = D.R_s.*sin(THETA).*sin(PHI); %y
112    Rpos(3,:) = D.R_s.*cos(THETA); %z
113
114    % Plot reflected rays
115    for i = 5:10:N_l^2
116        quiver(Rpos(1,i),Rpos(3,i),R(1,i),R(3,i),1, ...
117              'k','MaxHeadSize',0.02);
118    end
119    xlabel('Meters');
120    ylabel('Meters');
121    set(gca,'FontSize',15);
122    hold off
123
124    %% Plot 3D GO
125
126    % Generate geometry
127    figure; hold on
128    % Change camera view to slightly above reflector
129    view([D.R_s,D.R_s/2,D.R_s/2]);
130    % Plot reflector
131    ref = surf(D.X,D.Y,D.Z);
132    % Make it pretty
133    set(ref,'FaceColor',[0.41,0.41,0.41],'Edgelighting','gouraud');
134    % Label origin
135    text(0,0,0,'O \rightarrow ','HorizontalAlignment','right');
136    % Plot z axis and label it
137    quiver3(0,0,0,D.width/2,0,0);
138    text(D.height,0,0,'Z','HorizontalAlignment','right');
139    % Plot x axis and label it
140    quiver3(0,0,0,0,D.height/2);
141    text(0,0,D.height/2,'X','HorizontalAlignment','right');
142    % Plot y axis and label it
143    quiver3(0,0,0,0,D.height/2,0);
144    text(0,D.height/2,0,'Y','HorizontalAlignment','right');
145    axis equal
146    axis off
147    %axis vis3d
148
149    % Plot surface normals for i = 1:size(N,2)

```



```

150     %      ...
151     quiver3(0,0,0,N(1,i),N(2,i),N(3,i),1,'r','MaxHeadSize',0.02);
152     % end
153     %Plot incident rays
154     for i = 1:size(I,2)
155         quiver3(Ipos(1,i)+(3*I(1,i)/4),Ipos(2,i),Ipos(3,i), ...
156             I(1,i),I(2,i),I(3,i),0.25,'b','MaxHeadSize',0.02);
157     end
158
159     % Plot reflected rays
160     for i = 1:size(N,2)
161         quiver3(Rpos(1,i),Rpos(2,i),Rpos(3,i),R(1,i),R(2,i), ...
162             R(3,i),1,'k','MaxHeadSize',0.02);
163     end
164
165     hold off

```

A.2 Ray-Tracing Code for Cross-Shaped, Parabolically Contoured Reflector

```

1     %Housekeeping
2     clear;
3     close all;
4     clc;
5
6     % Ray-Tracing for Cross-shaped, Parabolically Contoured Reflector
7
8     %% User Inputs
9
10    % Sampling
11    Ns = 12;    % Number of ray samples across each dimension
12
13    % Dimensions
14    D = 150;    % Aperture diameter, meters
15    f = 80;    % Focus of parabola, meters
16    w = 6.74;  % Arm width, meters
17    L = 71.63; % Arm length, meters
18
19    %% Calculations
20
21    % Standard equation:  $y = ax^2$ ,  $a = 1/4f$ 
22    a = 1/(4*f);
23
24    % Define y
25    y = -D/2:0.1:D/2;
26
27    % Equation
28    x = a*y.^2-100;

```

```

29
30 % Plot 2D geometry
31 figure;
32 hold on
33 plot(x,y);
34 axis equal
35 xlabel('Meters','fontsize',12);
36 ylabel('Meters','fontsize',12);
37
38 % Calculate and Plot Incident rays
39 I = zeros(2,Ns);
40 Ipos = zeros(2,Ns);
41 for i = 1:Ns
42     I(1,i) = x(i*round(length(x)/Ns));
43     Ipos(2,i) = y(i*round(length(x)/Ns));
44     quiver(Ipos(1,i),Ipos(2,i),I(1,i),I(2,i),1,'b', ...
45           'MaxHeadSize',0.02);
46 end
47
48 % Calculate and Plot Surface Normals
49 N = zeros(2,Ns);
50 Npos = zeros(2,Ns);
51 Npos(1,:) = I(1,:);
52 Npos(2,:) = Ipos(2,:);
53 for i = 1:Ns
54
55     % Calculate derivative at this point
56     slope = 2*a*Npos(2,i);
57
58     % Calculate second point to make a vector
59     Px = 1;
60     Py = slope*Px;
61
62     % Make surface normal
63     N(2,i) = Px*cos(pi/2)-Py*sin(pi/2);
64     N(1,i) = Px*sin(pi/2)+Py*cos(pi/2);
65     quiver(Npos(1,i),Npos(2,i),N(1,i),N(2,i),10,'r', ...
66           'MaxHeadSize',0.02);
67 end
68
69 % Reflected Rays
70 R = zeros(2,Ns);
71 Rpos = zeros(2,Ns);
72 Rpos(1,:) = I(1,:);
73 Rpos(2,:) = Ipos(2,:);
74 for i = 1:Ns
75     % Calculate angle between the incident ray and the
76     % surface normal
77     theta = pi - acos(dot(I(:,i),N(:,i))/...
78           (sqrt(I(1,i)^2+I(2,i)^2)*sqrt(N(1,i)^2+N(2,i)^2)));
79
80     % Calculate Reflected ray

```

```

81         if i < round(Ns/2) % Flip over the axis of symmetry
82             R(1,i) = N(1,i)*cos(theta)-N(2,i)*sin(theta);
83             R(2,i) = N(1,i)*sin(theta)+N(2,i)*cos(theta);
84         else
85             R(1,i) = N(1,i)*cos(-theta)-N(2,i)*sin(-theta);
86             R(2,i) = N(1,i)*sin(-theta)+N(2,i)*cos(-theta);
87         end
88
89         quiver(Rpos(1,i),Rpos(2,i),R(1,i),R(2,i),100,'k', ...
90             'MaxHeadSize',0.02);
91     end
92
93     % Plot the focus point
94     scatter(-20,0);
95
96     %% Cross section Geometry
97
98     % New Way, uses surface plot instead
99     x1 = linspace(-D/2,D/2,256);
100    y1 = linspace(-w/2,w/2,8);
101    x2 = linspace(-w/2,w/2,8);
102    y2 = linspace(-D/2,D/2,256);
103
104    [X1,Y1] = meshgrid(x1,y1);
105    [X2,Y2] = meshgrid(x2,y2);
106    Z1 = a*X1.^2 + a*Y1.^2;
107    Z2 = a*X2.^2 + a*Y2.^2;
108
109    % To match dimensions, the matrices were found to be
110    % transposed incorrectly
111    X1 = X1';
112    Y1 = Y1';
113    Z1 = Z1';
114
115    %% Surface plot
116
117    figure;
118    hold on
119    surf(X1,Y1,Z1);
120    surf(X2,Y2,Z2);
121    axis equal
122    xlabel('Meters','fontsize',12);
123    ylabel('Meters','fontsize',12);
124    zlabel('Meters','fontsize',12);
125
126    % Plot rays for 3D geometry
127    % Calculate and Plot Incident rays for each set of arms
128    % (sections 1 and 2)
129    I1 = zeros(3,round(size(X1,1)*size(X1,2)/5));
130    I1(3,:) = -100*ones(1,round(size(X1,1)*size(X1,2)/5));
131    I2 = zeros(3,round(size(X2,1)*size(X2,2)/5));
132    I2(3,:) = -100*ones(1,round(size(X1,1)*size(X1,2)/5));

```

```

133 X1 = reshape(X1,1,size(X1,1)*size(X1,2));
134 Y1 = reshape(Y1,1,size(Y1,1)*size(Y1,2));
135 Z1 = reshape(Z1,1,size(Z1,1)*size(Z1,2));
136 X2 = reshape(X2,1,size(X2,1)*size(X2,2));
137 Y2 = reshape(Y2,1,size(Y2,1)*size(Y2,2));
138 Z2 = reshape(Z2,1,size(Z2,1)*size(Z2,2));
139 for i = 1:size(I1,2)
140     % Only Plot a subset of the overall sampled surface
141     if (10*i) < length(X1)
142         Ipos1(1,i) = X1(10*i);
143         Ipos1(2,i) = Y1(10*i);
144         Ipos1(3,i) = Z1(10*i)+100;
145         Ipos2(1,i) = X2(10*i);
146         Ipos2(2,i) = Y2(10*i);
147         Ipos2(3,i) = Z2(10*i)+100;
148     end
149     if i ≤ size(Ipos1,2)
150         quiver3(Ipos1(1,i),Ipos1(2,i),Ipos1(3,i),I1(1,i), ...
151             I1(2,i),I1(3,i),1,'b','MaxHeadSize',0.02);
152         quiver3(Ipos2(1,i),Ipos2(2,i),Ipos2(3,i),I2(1,i), ...
153             I2(2,i),I2(3,i),1,'b','MaxHeadSize',0.02);
154     end
155 end
156
157 % Surface Normals
158 N1 = zeros(3,round(size(X1,1)*size(X1,2)/5));
159 N2 = zeros(3,round(size(X2,1)*size(X2,2)/5));
160 for i = 1:size(I1,2)
161     % Only Plot a subset of the overall sampled surface
162     if (10*i) < length(X1)
163         Npos1(1,i) = X1(10*i);
164         Npos1(2,i) = Y1(10*i);
165         Npos1(3,i) = Z1(10*i);
166         Npos2(1,i) = X2(10*i);
167         Npos2(2,i) = Y2(10*i);
168         Npos2(3,i) = Z2(10*i);
169     end
170     if i ≤ size(Ipos1,2)
171         % Calculate derivative at this point
172         slope1x = 2*a*Npos1(1,i);
173         slope1y = 2*a*Npos1(2,i);
174         slope2x = 2*a*Npos2(1,i);
175         slope2y = 2*a*Npos2(2,i);
176
177         % Calculate second point to make a vector
178         Px = 1;
179         Py = 0;
180         Pz1 = slope1x*Px + slope1y*Py;
181         Pz2 = slope2x*Py + slope2y*Px;
182
183         % Make surface normal
184         N1(1,i) = Px*cos(pi/2)-Pz1*sin(pi/2);

```

```

185     N1(2,i) = Py;
186     N1(3,i) = Px*sin(pi/2)+Pz1*cos(pi/2);
187     N2(1,i) = Py;
188     N2(2,i) = Px*cos(pi/2)-Pz2*sin(pi/2);
189     N2(3,i) = Px*sin(pi/2)+Pz2*cos(pi/2);
190
191     % Plot the surface normals
192     quiver3(Npos1(1,i),Npos1(2,i),Npos1(3,i),N1(1,i), ...
193             N1(2,i),N1(3,i),5,'r','MaxHeadSize',0.02);
194     quiver3(Npos2(1,i),Npos2(2,i),Npos2(3,i),N2(1,i), ...
195             N2(2,i),N2(3,i),5,'r','MaxHeadSize',0.02);
196 end
197 end
198
199 % Reflected Rays
200 R1 = zeros(3,round(size(X1,1)*size(X1,2)/5));
201 R2 = zeros(3,round(size(X2,1)*size(X2,2)/5));
202 for i = 1:size(I1,2)
203     % Only Plot a subset of the overall sampled surface
204     if (10*i) < length(X1)
205         Rpos1(1,i) = X1(10*i);
206         Rpos1(2,i) = Y1(10*i);
207         Rpos1(3,i) = Z1(10*i);
208         Rpos2(1,i) = X2(10*i);
209         Rpos2(2,i) = Y2(10*i);
210         Rpos2(3,i) = Z2(10*i);
211     end
212     if i ≤ size(Ipos1,2)
213         % Calculate angle between the incident ray and the
214         % surface normal
215         thetal = pi - acos(dot(I1(:,i),N1(:,i))/ ...
216                             (sqrt(I1(1,i)^2+I1(2,i)^2+I1(3,i)^2)* ...
217                             sqrt(N1(1,i)^2+N1(2,i)^2+N1(3,i)^2)));
218         theta2 = pi - acos(dot(I2(:,i),N2(:,i))/ ...
219                             (sqrt(I2(1,i)^2+I2(2,i)^2+I2(3,i)^2)* ...
220                             sqrt(N2(1,i)^2+N2(2,i)^2+N2(3,i)^2)));
221
222         % Calculate Reflected rays
223         if Rpos1(1,i) > 0 % Flip over the axis of symmetry
224             R1(1,i) = N1(1,i)*cos(thetal)-N1(3,i)*sin(thetal);
225             R1(2,i) = N1(2,i);
226             R1(3,i) = N1(1,i)*sin(thetal)+N1(3,i)*cos(thetal);
227         else
228             R1(1,i) = N1(1,i)*cos(-thetal)-N1(3,i)*sin(-thetal);
229             R1(2,i) = N1(2,i);
230             R1(3,i) = N1(1,i)*sin(-thetal)+N1(3,i)*cos(-thetal);
231         end
232         if Rpos2(2,i) > 0 % Flip over the axis of symmetry
233             R2(1,i) = N2(1,i);
234             R2(2,i) = N2(2,i)*cos(theta2)-N2(3,i)*sin(theta2);
235             R2(3,i) = N2(2,i)*sin(theta2)+N2(3,i)*cos(theta2);
236         else

```

```

237         R2(1,i) = N2(1,i);
238         R2(2,i) = N2(2,i)*cos(-theta2)-N2(3,i)*sin(-theta2);
239         R2(3,i) = N2(2,i)*sin(-theta2)+N2(3,i)*cos(-theta2);
240     end
241
242     % Plot the surface normals
243     quiver3(Rpos1(1,i),Rpos1(2,i),Rpos1(3,i),R1(1,i), ...
244             R1(2,i),R1(3,i),100,'k','MaxHeadSize',0.02);
245     quiver3(Rpos2(1,i),Rpos2(2,i),Rpos2(3,i),R2(1,i), ...
246             R2(2,i),R2(3,i),100,'k','MaxHeadSize',0.02);
247 end
248 end

```

A.3 FF Radiation Pattern Computation Code Using FD Eigenmode Analysis to Determine Equivalent Sources

```

1     % NOTE: This code only works for equal width/length
2     % dimensions with equal numbers of discrete steps.
3
4     % Housekeeping
5     clear;
6     close all;
7     clc;
8
9     %% Inputs
10
11     fmin = 1e9;           % Operational frequency minimum, Hz
12     fmax = 2e9;           % Operational frequency maximum, Hz
13     HPBW = 100.459;       % Desired Maximum Half-Power
14                             % Beamwidth, degrees
15     A = 1;                % Source strength, volts/meter
16     N = 165;              % Grid width/length number of samples
17     flag = 1;              % Flag to introduce boundaries or not
18                             % (1=boundaries on, 0 = off)
19     mode = 'TM';          % Which modes to explore, TM or TE
20
21     %% Constants
22
23     % Permittivity of Free Space,
24     % (seconds^4*Amperes^2)/(meters^3*kilograms)
25     epsilon = 8.85418782e-12;
26
27     % Permeability of Free Space, (Volts*Seconds)/(Amperes*meters)
28     mu = (4*pi)*1e-7;
29
30     %% Calculations
31

```

```

32 % Medium calculations
33 % Speed of light, meters/second
34 c = 1/sqrt(epsilon*mu);
35 % Intrinsic impedance, ohms
36 eta = sqrt(mu/epsilon);
37
38 % Frequency, wavelength, wave number calculations
39 % Vector of frequencies, Hz
40 f = fmin:(0.1e9):fmax;
41 % Vector of frequencies, rad/s
42 omega = 2*pi.*f;
43 % Vector of wavelengths, meters
44 lambda = c./f;
45 % Vector of wave numbers, rad/m
46 k = 2*pi./lambda;
47
48 % Aperture dimensions calculations (Square aperture,
49 % to later have additional boundaries added in to
50 % change the FF pattern)
51 a = (lambda./sind(HPBW/2));
52 b = a;
53
54 %% Grid Generation
55
56 % Sampling the aperture
57 x = zeros(length(f),N+1);
58 y = zeros(length(f),N+1);
59 for i = 1:length(f)
60     % Vector of x spatial steps, meters
61     x(i,:) = 0:a(i)/N:a(i);
62     % Vector of y spatial steps, meters
63     y(i,:) = 0:b(i)/N:b(i);
64 end
65
66 % Grid spacing
67 dx = mean(diff(x,[],2),2); % spatial step size, meters
68
69 %% Solve for cutoff frequencies of aperture
70
71 % Flag to tell numgrid to make cross-shaped aperture
72 if flag == 1
73     R = 'K';
74     u = (lambda./sind(6.18/2));
75
76     % Fraction of the width/length to include (all else excluded)
77     frac = mean(a./u);
78 else
79     R = 'S';
80     frac = 1;
81 end
82
83 % Grid Generation

```

```

84 G = numgrid(R,N,frac);
85
86 % Create Laplacian Matrix
87 L = delsq(G);
88
89 % Apply normal derivative condition for TE modes
90 if strcmp(mode, 'TE')
91     % Edges and cross-shape
92     if flag == 1
93         % First corner
94         ind1 = find(G(:,2) # 0, 1, 'first');
95         % Second corner
96         ind1 = [ind1 find(G(:,2) # 0, 1, 'last')];
97         corners = G(ind1, 2);
98         % All other outer corners
99         corners = [corners G(ind1, N-1) G(2, ind1) .' ...
100                    G(N-1, ind1) .'];
101         % Inner corners of cross
102         corners = [corners G(ind1, ind1)];
103         % Top most boundary
104         edges = G(2, ind1(1)+1:ind1(2)-1);
105         % Bottom most boundary
106         edges = [edges G(N-1, ind1(1)+1:ind1(2)-1)];
107         % Left most boundary
108         edges = [edges G(ind1(1)+1:ind1(2)-1, 2) .'];
109         % Right most boundary
110         edges = [edges G(ind1(1)+1:ind1(2)-1, N-1) .'];
111         % Top left cross boundary (horizontal)
112         edges = [edges G(ind1(1), 3:ind1(1)-1)];
113         % Bottom left cross boundary (horizontal)
114         edges = [edges G(ind1(2), 3:ind1(1)-1)];
115         % Top Right cross boundary (horizontal)
116         edges = [edges G(ind1(1), ind1(2)+1:N-2)];
117         % Bottom Right cross boundary (horizontal)
118         edges = [edges G(ind1(2), ind1(2)+1:N-2)];
119         % Top left cross boundary (vertical)
120         edges = [edges G(3:ind1(1)-1, ind1(1)) .'];
121         % Top Right cross boundary (vertical)
122         edges = [edges G(3:ind1(1)-1, ind1(2)) .'];
123         % Bottom left cross boundary (vertical)
124         edges = [edges G(ind1(2)+1:N-2, ind1(1)) .'];
125         % Bottom right cross boundary (vertical)
126         edges = [edges G(ind1(2)+1:N-2, ind1(2)) .'];
127         for i = 1:(size(corners,1)*size(corners,2))
128             L(corners(i), corners(i)) = ...
129                 2*L(corners(i), corners(i))/4;
130         end
131         for i = 1:length(edges)
132             L(edges(i), edges(i)) = 3*L(edges(i), edges(i))/4;
133         end
134     end
135 % Edges only
136 else

```



```

134         % diagonal index for four corners
135         idx1 = [1 N-2 (N-2)^2-N+3 (N-2)^2];
136         % diagonal index for the sides
137         idx2 = [2:(N-3) ((N-2)^2-N+4):(N-2)^2-1];
138         % add index for the top
139         idx2 = [idx2 (N-1):N-2:(N-2)^2-N+2];
140         % add index for the bottom
141         idx2 = [idx2 (2*N-4):N-2:(N-2)^2-1];
142         for i = 1:length(idx1)
143             L(idx1(i),idx1(i)) = 2*L(idx1(i),idx1(i))/4;
144         end
145         for i = 1:length(idx2)
146             L(idx2(i),idx2(i)) = 3*L(idx2(i),idx2(i))/4;
147         end
148     end
149 end
150
151 % Calculate the Eigenvalues of the Laplacian Operator Matrix
152 [D,E] = eigs(-L,[],10,'sm');
153
154 % Calculate the cutoff frequencies from the eigenvalues
155 j = 1;
156 for i = 1:size(E,1)
157     f(i,:) = (1./(2*pi.*dx)).*sqrt(-E(i,j)/(mu*epsilon));
158     j = j + 1;
159 end
160
161 % Sort modes
162 f = sort(f);
163
164 % Only calculate analytical cutoff frequencies for square
165 % apertures
166 if flag == 0
167     if strcmp(mode,'TE')
168         % Analytical Cutoff frequencies
169         m = 0:4;
170         n = 0:4;
171         f_an = zeros(length(m),length(n),length(a));
172         for o = 1:length(a)
173             for i = 1:5
174                 for j = 1:5
175                     f_an(i,j,o) = ...
176                         (1/(2*pi*sqrt(mu*epsilon)))* ...
177                         sqrt(((m(i)*pi)/a(o)).^2+...
178                             ((n(j)*pi)/b(o)).^2);
179                 end
180             end
181         else
182             % Analytical Cutoff frequencies
183             m = 1:5;
184             n = 1:5;

```

```

185         f_an = zeros(length(m),length(n),length(a));
186     for o = 1:length(a)
187         for i = 1:5
188             for j = 1:5
189                 f_an(i,j,o) = ...
190                     (1/(2*pi*sqrt(mu*epsilon)))* ...
191                     sqrt(((m(i)*pi)/a(o)).^2+...
192                         ((n(j)*pi)/b(o)).^2);
193             end
194         end
195     end
196
197     % reshape and sort data in ascending order. This order
198     % corresponds to how to count the Transverse modes.
199     % Store the indexes to indicate which modes are which.
200     % Grab only modes for one set of dimensions, they will
201     % count the same way with any set of dimensions (it's the
202     % proportions that matter)
203     f_an_sort(:, :) = f_an(:, :, 1);
204
205     % Sort them, store the indexes for counting
206     [f_an_sort, I] = ...
207         sort(reshape(f_an_sort, 1, size(f_an_sort, 1)*...
208             size(f_an_sort, 2)));
209
210     % Get the indexes for counting
211     [I, J] = ind2sub(size(f_an(:, :, 1)), I);
212 end
213
214 % Check numerical results against analytical results
215 % Loop over each set of dimensions
216 for o = 1:length(a)
217     string = ...
218         sprintf('For Aperture Dimensions: a = %f, b = ...
219             %f\n', a(o), b(o));
220     disp(string);
221     % Loop over calculated numerical modes
222     for i = 1:size(f, 1)
223         if flag == 0
224             if strcmp(mode, 'TE')
225                 s_num = sprintf('TE %i %i mode numerical:...
226                     %g\n', m(I(i)), n(J(i)), f(i, o));
227                 s_an = sprintf('TE %i %i mode analytical:...
228                     %g\n', m(I(i)), n(J(i)), f_an(I(i), J(i), o));
229                 % Percent error
230                 s_error = sprintf('TE %i %i mode Percent ...
231                     error: %g%%\n', m(I(i)), n(J(i)), abs(100*...
232                         (f_an(I(i), J(i), o) - f(i, o)) / f_an(I(i), J(i), o)));
233             else
234                 s_num = sprintf('TM %i %i mode numerical:...
235                     %g\n', I(i), J(i), f(i, o));

```

```

236         s_an = sprintf('TM %i %i mode analytical:...
237             %g\n', I(i),J(i),f_an(I(i),J(i),o));
238         % Percent error
239         s_error = sprintf('TM %i %i mode Percent ...
240             error: %g%%\n',I(i), J(i),abs(100*...
241             (f_an(I(i),J(i),o)-f(i,o))/f_an(I(i),J(i),o)));
242     end
243     disp(s_num);
244     disp(s_an);
245     disp(s_error);
246 else
247     s_num = sprintf('Cutoff Frequency = %g\n',f(i,o));
248     disp(s_num);
249 end
250
251     disp('-----');
252 end
253 end
254
255 %% Plot modes
256
257 % Loop over the different aperture dimensions
258 Z = zeros(size(G));
259
260 % Sort the Eigenvectors and eigenvalues
261 [D,E] = sortem(D,E);
262
263 for i = 1:size(f,2)
264
265     figure;
266
267     % Loop for each eigenvalue (mode distribution)
268     for o = 1:size(f,1)
269         subplot(2,5,o);
270
271         % Find indexes for where aperture resides
272         P = find(G ~= 0);
273
274         % Calculate the distribution
275         temp = E(o,o).*D(:,o);
276
277         % Layout distribution
278         Z(P) = temp;%reshape(temp,N-2,N-2);
279
280         % Plot the distribution
281         pcolor(abs(Z));
282         shading flat
283         set(gca,'YDir','normal');
284         string = sprintf('Cutoff frequency = %0.3f ...
285             GHz',f(o,i)*10^(-9));
286         xlabel(string);
287     end

```

```

287         string = sprintf('Aperture Dimensions: a = ...
288             %0.3f m, b = %0.3f m',a(i),b(i));
289         mtit(string);
290     end
291
292     %% Post-Processing
293
294     % NOTE: for TE case, the TE00 mode is not valid,
295     % so move up a mode!!!
296
297     temp = E(1,1).*D(:,1);
298     Z(P) = temp;
299
300     % Which aperture to use as the input
301     ap_num = 1;
302     % Observation phi angle, radians
303     phi = 0:(pi/180):(2*pi);
304     % Observation theta angles, radians
305     theta = -pi/2:(pi/180):pi/2;
306     % Coefficient for nine point integration rule
307     C = 4*dx(ap_num)^2;
308     % Weights for nine point integration rule
309     wq = [1/36, 1/9, 1/36, 1/9, 4/9, 1/9, 1/36, 1/9, 1/36];
310     % Far-Field Distance, meters
311     r = 4*a(ap_num)^2/lambda(ap_num);
312
313     % Allocate space for run time vector
314     t = zeros(1,length(theta));
315
316     if flag == 1
317         % NOTE: for Brevity, this is hard coded for a grid size
318         % of 165. Later revisions will make it more robust
319         % Calculate Center points
320         Center = [find(G(:,3)~=0,1,'first')+1,3];
321         len = length(Center(2):2:163);
322         Center = [Center(1)*ones(1,len); ...
323             3:2:163];
324         for i = 1:3
325             Center = [Center(1,:) ...
326                 (Center(1,i*len)+2)*ones(1,len); ...
327                 Center(2,:) 3:2:163];
328         end
329         Center = [Center(1,:) Center(2,:); ...
330             Center(2,:) Center(1,:)];
331         Center = sub2ind(size(Z),Center(1,:),Center(2,:));
332     else
333         % Square aperture
334         Center = [3,3];
335         len = length(Center(2):2:163);
336         Center = [Center(1)*ones(1,len); ...
337             3:2:163];
338         for i = 1:len-1

```

```

338         Center = [Center(1,:) ...
339                   (Center(1,i*len)+2)*ones(1,len); ...
340                   Center(2,:) 3:2:163];
341     end
342     Center = sub2ind(size(Z),Center(1,:),Center(2,:));
343 end
344 % TE modes
345 if strcmp(mode,'TE')
346
347     Ex = zeros(size(Z));
348     Ey = zeros(size(Z));
349     % Calculate tangential field components
350     for i = 1:length(P)
351         [temp1,temp2] = ind2sub(size(Z),P(i));
352         Ex(temp1,temp2) = (Z(temp1 + 1,temp2) -...
353                           Z(temp1 - 1,temp2))/(1i*2*omega(ap_num)*...
354                           epsilon*dx(ap_num));
355         Ey(temp1,temp2) = -(Z(temp1,temp2 + 1) - ...
356                             Z(temp1,temp2 - 1))/(1i*2*omega(ap_num)*...
357                             epsilon*dx(ap_num));
358     end
359
360     % Initialize FF variables
361     Lth = zeros(length(theta),length(phi));
362     Lph = zeros(length(theta),length(phi));
363
364     % Loop over far field observations
365     for j = 1:length(theta)
366
367         %Update run time to user
368         if j > 1 % All other iterations
369             t_sofar = sum(t(1:(j-1)));
370             t_est = (t_sofar*length(theta)/(j-1)-t_sofar)/60;
371             fprintf('Theta %d of %d, %.02f minutes ...
372                     remaining\n', j,length(theta),t_est);
373         else % First Iteration
374             fprintf('Theta %d of %d\n',j,length(theta));
375         end
376
377         tic
378
379         for o = 1:length(phi)
380
381             sumth = 0;
382             sumph = 0;
383
384             % Loop over aperture (subdomains)
385             for i = 1:length(Center)
386
387                 tempth = 0;
388                 tempph = 0;

```

```

389
390     [p1,p2] = ind2sub(size(Z),Center(i));
391
392     % Calculate Current Subdomain
393     sub = [ p1 + 1, p2 - 1; p1 + 1, p2; p1 + 1, ...
394            p2 + 1; p1 - 1, p2 - 1; p1 - 1, p2; p1, ...
395            p2 + 1; p1 - 1, p2 - 1; p1 - 1, p2; ...
396            p1 - 1, p2 + 1];
397     sub_lin = sub2ind(size(Z),sub(:,1),sub(:,2));
398
399     % Loop over current subdomain
400     for q = 1:9
401
402         % Calculate exponential for integral
403         ex = exp(-li*k(ap_num) ...
404                * ((x(ap_num,sub(q,2))-a(ap_num)/2)*...
405                  sin(theta(j))*cos(phi(o)) + ...
406                  (y(ap_num,sub(q,1))-a(ap_num)/2)*...
407                  sin(theta(j))*sin(phi(o))));
408
409         % L Theta
410         tempth = tempth + wq(q)*ex*...
411                (-Ey(sub_lin(q))*cos(theta(j))*...
412                 cos(phi(o)) + -Ex(sub_lin(q))*...
413                 cos(theta(j))*sin(phi(o)));
414
415         % L Phi
416         tempph = tempph + wq(q)*ex*...
417                (Ey(sub_lin(q))*sin(phi(o)) + ...
418                 -Ex(sub_lin(q))*cos(phi(o)));
419
420     end
421     sumth = sumth + C*tempth;
422     sumph = sumph + C*tempph;
423 end
424
425     Lth(j,o) = sumth;
426     Lph(j,o) = sumph;
427 end
428
429     % Time Keeping
430     t(j) = toc;
431 end
432
433     % Calculate FF radiation pattern
434     Eth = (-li*k(ap_num)*exp(-li*k(ap_num)*r).*Lph)./(4*pi*r);
435     Eph = (li*k(ap_num)*exp(-li*k(ap_num)*r).*Lth)./(4*pi*r);
436
437     Eff = sqrt(Eth.*conj(Eth) + Eph.*conj(Eph));
438     Eff_db = 20*log10(Eff);
439
440     % Plot FF pattern

```

```

441     figure;
442     B = find(theta < 0);
443     theta(B) = theta(B) + 2*pi;
444     polar2(theta, Eff_db. ');
445     xlabel('FF radiation pattern, dB', 'FontSize', 18);
446
447     else % TM modes
448
449         Hx = zeros(size(Z));
450         Hy = zeros(size(Z));
451         % Calculate the Tangential field components
452         for i = 1:length(P)
453             [temp1,temp2] = ind2sub(size(Z),P(i));
454             Hx(temp1,temp2) = -(Z(temp1 + 1,temp2) -...
455                 Z(temp1 - 1,temp2))/(1i*2*omega(ap_num)*...
456                 mu*dx(ap_num));
457             Hy(temp1,temp2) = (Z(temp1,temp2 + 1) - ...
458                 Z(temp1,temp2 - 1))/(1i*2*omega(ap_num)*...
459                 mu*dx(ap_num));
460         end
461
462         % Initialize FF variables
463         Nth = zeros(length(theta),length(phi));
464         Nph = zeros(length(theta),length(phi));
465
466         % Loop over far field observations
467         for j = 1:length(theta)
468
469             %Update run time to user
470             if j > 1 % All other iterations
471                 t_sofar = sum(t(1:(j-1)));
472                 t_est = (t_sofar*length(theta)/(j-1)-t_sofar)/60;
473                 fprintf('Theta %d of %d, %.02f minutes...
474                     remaining\n',j,length(theta),t_est);
475             else % First Iteration
476                 fprintf('Theta %d of %d\n',j,length(theta));
477             end
478
479             tic
480
481             for o = 1:length(phi)
482                 sumth = 0;
483                 sumph = 0;
484                 % Loop over aperture (subdomains)
485                 for i = 1:length(Center)
486
487                     tempth = 0;
488                     tempph = 0;
489
490                     [p1,p2] = ind2sub(size(Z),Center(i));
491
492                     % Calculate Current Subdomain

```

```

493         sub = [ p1 + 1, p2 - 1; p1 + 1, p2; p1 + 1, ...
494                p2 + 1; p1, p2 - 1; p1, p2; p1, ...
495                p2 + 1; p1 - 1, p2 - 1; p1 - 1, p2; ...
496                p1 - 1, p2 + 1];
497         sub_lin = sub2ind(size(Z),sub(:,1),sub(:,2));
498
499         % Loop over current subdomain
500         for q = 1:9
501
502             % Calculate exponential for integral
503             ex = exp(1i*k(ap_num)* ...
504                    ((x(ap_num,sub(q,2))+a(ap_num)/2)*...
505                     sin(theta(j))*cos(phi(o)) + ...
506                     (y(ap_num,sub(q,1))+a(ap_num)/2)*...
507                     sin(theta(j))*sin(phi(o))));
508
509             % N Theta
510             tempth = tempth + wq(q)*ex*...
511                    (-2*Hy(sub_lin(q))*cos(theta(j))*...
512                     cos(phi(o)) + 2*Hx(sub_lin(q))*...
513                     cos(theta(j))*sin(phi(o)));
514
515             % N Phi
516             tempph = tempph + wq(q)*ex*...
517                    (2*Hy(sub_lin(q))*sin(phi(o)) + ...
518                     2*Hx(sub_lin(q))*cos(phi(o)));
519
520         end
521         sumth = sumth + C*tempth;
522         sumph = sumph + C*tempph;
523     end
524
525     Nth(j,o) = sumth;
526     Nph(j,o) = sumph;
527 end
528
529 % Time Keeping
530 t(j) = toc;
531 end
532
533 Eth = ...
534     (-1i*k(ap_num)*exp(-1i*k(ap_num)*r).*Nth*eta)./(4*pi*r);
535 Eph = ...
536     (-1i*k(ap_num)*exp(-1i*k(ap_num)*r).*Nph*eta)./(4*pi*r);
537
538 Eff = sqrt(Eth.*conj(Eth) + Eph.*conj(Eph));
539 Eff_db = 20*log10(Eff);
540
541 % Plot FF pattern
542 figure;
543 B = find(theta < 0);
544 theta(B) = theta(B) + 2*pi;

```



```

543     polar2(theta, Eff_db. ');
544     xlabel('FF radiation pattern, dB', 'FontSize', 18);
545 end

```

A.4 Pattern Addition Code

```

1      % This script takes in data from SatCom *.oaa files and
2      % combines them into a single group of data to then plot
3      % the far-field of the particular antenna. This is
4      % accomplished from pattern addition
5
6      % Housekeeping
7      clear;
8      close all;
9      clc;
10
11     %% Import Data
12
13     % Open the input files
14     fin1 = fopen('R150_RW-001500MHz.oaa', 'r');
15     fin2 = ...
16         fopen('R150_opposite-orientation_RW-001500MHz.oaa', 'r');
17
18     % Take in the header information
19     temp1 = fgetl(fin1);
20     temp2 = fgetl(fin2);
21
22     % Read in the numerical data
23     temp1 = fscanf(fin1, '%f, %f, %f, %f, %f\n');
24     temp2 = fscanf(fin2, '%f, %f, %f, %f, %f\n');
25
26     % Check to be sure that data files were the same length
27     if length(temp1) == length(temp2)
28
29         THETA = zeros(1, length(temp1)/5-1);
30         E_TH_DB1 = zeros(1, length(temp1)/5-1);
31         E_TH_DB2 = zeros(1, length(temp1)/5-1);
32         E_TH_DG1 = zeros(1, length(temp1)/5-1);
33         E_TH_DG2 = zeros(1, length(temp1)/5-1);
34         E_PH_DB1 = zeros(1, length(temp1)/5-1);
35         E_PH_DB2 = zeros(1, length(temp1)/5-1);
36         E_PH_DG1 = zeros(1, length(temp1)/5-1);
37         E_PH_DG2 = zeros(1, length(temp1)/5-1);
38
39         % Separate the data
40         for i = 0:(length(temp1)/5-1)
41             THETA(i + 1) = temp1(1+5*i);

```

```

42         E_TH_DB1(i + 1) = temp1(2+5*i);
43         E_TH_DB2(i + 1) = temp2(2+5*i);
44
45         E_TH_DG1(i + 1) = temp1(3+5*i);
46         E_TH_DG2(i + 1) = temp2(3+5*i);
47
48         E_PH_DB1(i + 1) = temp1(4+5*i);
49         E_PH_DB2(i + 1) = temp2(4+5*i);
50
51         E_PH_DG1(i + 1) = temp1(5+5*i);
52         E_PH_DG2(i + 1) = temp2(5+5*i);
53     end
54 else
55
56     % Separate the data
57     for i = 0:(length(temp1)/5-1)
58         THETA1(i + 1) = temp1(1+5*i);
59         E_TH_DB1(i + 1) = temp1(2+5*i);
60         E_TH_DG1(i + 1) = temp1(3+5*i);
61         E_PH_DB1(i + 1) = temp1(4+5*i);
62         E_PH_DG1(i + 1) = temp1(5+5*i);
63     end
64     for i = 0:(length(temp2)/5-1)
65         THETA2(i + 1) = temp2(1+5*i);
66         E_TH_DB2(i + 1) = temp2(2+5*i);
67         E_TH_DG2(i + 1) = temp2(3+5*i);
68         E_PH_DB2(i + 1) = temp2(4+5*i);
69         E_PH_DG2(i + 1) = temp2(5+5*i);
70     end
71 end
72
73 % Free up memory
74 clear temp1 temp2
75
76 % Close input files
77 fclose(fin1);
78 fclose(fin2);
79
80 %% Pattern Addition
81
82 % Create Phi vector
83 PHI = 0:1:360;
84
85 % Change phase components to radians for coherent summation
86 E_TH_R1 = E_TH_DG1.*(pi/180);
87 E_TH_R2 = E_TH_DG2.*(pi/180);
88 E_PH_R1 = E_PH_DG1.*(pi/180);
89 E_PH_R2 = E_PH_DG2.*(pi/180);
90
91 % Theta component pattern addition
92 % E_TH_DB = E_TH_DB1 + E_TH_DB2;
93 E_TH_linear = (10.^(E_TH_DB1./20) + 10.^(E_TH_DB2./20)).*...

```

```

94         exp(-1i*(E_TH_R1 + E_TH_R2));
95
96     % Phi component pattern addition
97     % E_PH_DB = E_PH_DB1 + E_PH_DB2;
98     E_PH_linear = (10.^(E_PH_DB1./20) + 10.^(E_PH_DB2./20)).*...
99         exp(-1i*(E_PH_R1 + E_PH_R2));
100
101     %% 3D plots
102
103     % Reformat the data
104     I = find(THETA == 0);
105     dtheta = mean(diff(I));
106     E_TH_linear = reshape(E_TH_linear,dtheta,length(PHI));
107     E_TH_DB = 20.*log10(abs(E_TH_linear));
108
109     E_PH_linear = reshape(E_PH_linear,dtheta,length(PHI));
110     E_PH_DB = 20.*log10(abs(E_PH_linear));
111
112     % Plot the theta component of the E-field in dB
113     figure;
114     sphere3d(E_TH_DB,-pi,pi,-pi/2,pi/2, ...
115         max(max(E_TH_DB)),2,'surf');
116     colorbar('off');
117     title('Theta component of FF E-field, dB');
118
119     % Plot the phi component of the E-field in dB
120     figure;
121     sphere3d(E_PH_DB,-pi,pi,-pi/2,pi/2, ...
122         max(max(E_PH_DB)),2,'surf');
123     colorbar('off');
124     title('Phi component of FF E-field, dB');
125
126     % Plot the E-field in dB
127     figure;
128     E_abs = sqrt(E_TH_linear.*conj(E_TH_linear) + ...
129         E_PH_linear.*conj(E_PH_linear));
130     E_DB = 20*log10(E_abs);
131     sphere3d(E_DB,-pi,pi,-pi/2,pi/2,1,1,'surf');
132     colorbar('off');
133     title('FF E-field, dB');

```

Bibliography

- [1] G. Hyde and R. C. Spencer, "Studies of the focal region of a spherical reflector: Geometric optics," *IEEE Transactions on Antennas and Propagation*, vol. AP-16, pp. 317–324, May 1968.
- [2] C. A. Balanis, *Antenna Theory: Analysis and Design, Third Edition*. Hoboken, NJ: John Wiley & Sons Inc., 2005.
- [3] R. Harrington, *Time-Harmonic Electromagnetic Fields*. McGraw-Hill, Inc., 1961.
- [4] W. A. Imbriale, *Large Antennas of the Deep Space Network*. Hoboken, NJ: John Wiley & Sons Inc., 2003.
- [5] S. V. Hoerner, "Arecibo three-mirror systems: Optimizing the optics," Engineering Division Internal Report 112, National Radio Astronomy Observatory, Green Bank, WV, February 1983.
- [6] W. L. Stutzman and G. A. Thiele, *Antenna Theory and Design*. New York: John Wiley & Sons Inc., 1998.
- [7] T. Li, "A study of spherical reflectors as wide-angle scanning antennas," *IRE Transactions Antennas Propagation*, vol. AP-7, pp. 223–226, July 1959.
- [8] J. L. Volakis, *Antenna Engineering Handbook, Fourth Edition*. New York, NY: McGraw-Hill Companies, 2007.
- [9] R. Kaplan and J. L. Schultz, "Deployable reflector structure," 06 1977.
- [10] I. Stern, "Deployable reflector antenna with tensegrity support architecture and associated methods," 04 2003.
- [11] Y. Rahmat-Samii, A. Zaghoul, and A. Williams, "Large deployable antennas for satellite communications," *IEEE*, 2000.
- [12] M. W. Thomson, "The astromesh deployable reflector," *IEEE*, 1999.
- [13] R. Freeland, G. Bilyeu, G. Veal, and M. Mikulas, "Inflatable deployable space structures technology summary," *49th International Astronautical Congress*, 1998.
- [14] J. Goodman, *Introduction to Fourier Optics, Second Edition*. Greenwood Village, CO: Roberts & Co Publishers, 2005.
- [15] G. Hyde, "Studies of the focal region of a spherical reflector: Stationary phase evaluation," *IEEE Transactions on Antennas and Propagation*, vol. AP-16, pp. 646–656, November 1968.

- [16] C. A. Balanis, *Advanced Engineering Electromagnetics, Second Edition*. Hoboken, NJ: John Wiley & Sons Inc., 2012.
- [17] P. Beckmann, *The Depolarization of Electromagnetic Waves*. Boulder, CO: The Golem Press, 1968.
- [18] K. F. Warnick, *Numerical Methods For Engineering: An Introduction Using MATLAB and Computational Electromagnetics Examples, First Edition*. Edison, NJ: SciTech Publishing, 2011.
- [19] A. Love, “The integration of the equations of propagation of electric waves,” *Phil. Trans. Roy. Soc. London, Ser. A*, vol. 197, pp. 1–45, 1901.
- [20] A. Schell, “The diffraction theory of large aperture spherical reflector antennas,” *IEEE Transactions on Antennas and Propagation*, vol. AP-11, pp. 428–432, July 1963.
- [21] A. J. Terzuoli, “Class notes, eeng-625, em waves - maxwellian theory made elegant.”
- [22] S. Schelkunoff, “Some equivalence theorems of electromagnetics and their application to radiation problems,” *Bell System Tech. J.*, vol. 15, pp. 92–112, 1936.
- [23] M. O. Sadiku, “A simple introduction to finite element analysis,” *IEEE Transactions on Education*, vol. 32, pp. 85–93, January 1989.
- [24] L. R. Burchett, “Class report, diffraction analysis of rimshot antenna using fourier and rayleigh-sommerfield methods.”
- [25] Scitor, “Space-track,” February 2012.
- [26] C. Lee, S. Lee, and S. Chuang, “Plot of modal field distributions for rectangular and circular waveguides,” *IEEE Trans. on Microwave Theory and Techniques*, vol. MTT-33, no. 3, pp. 271–274, 1985.
- [27] M. Abramowitz and I. A. Stegun, *Handbook of Mathematical Functions: with Formulas, Graphs, and Mathematical Tables*. Mineola, NY: Dover Publications, 1964.
- [28] F. Holt and E. Bouche, “A gregorian corrector for spherical reflectors,” *IEEE Transactions on Antennas and Propagation*, pp. 44–47, January 1964.
- [29] G. McCormick, “A line feed for a spherical reflector,” *IEEE Transactions on Antennas and Propagation*, vol. AP-15, pp. 639–645, September 1967.

Vita

The author Joshua Michael Wilson was born in Middletown, OH on November 28, 1988. He was raised and attended grade school in Trenton, OH. He later attended Wright State University in Dayton, OH from 2007-2011 and received a Bachelor of Science in Electrical Engineering with a minor in Computer Science in 2011. He began work toward a Master of Science in Electrical Engineering at the Air Force Institute of Technology on Wright-Patterson Air Force Base, Dayton, OH in the winter of 2012.

REPORT DOCUMENTATION PAGE					<i>Form Approved</i> <i>OMB No. 0704-0188</i>	
The public reporting burden for this collection of information is estimated to average 1 hour per response, including the time for reviewing instructions, searching existing data sources, gathering and maintaining the data needed, and completing and reviewing the collection of information. Send comments regarding this burden estimate or any other aspect of this collection of information, including suggestions for reducing this burden to Department of Defense, Washington Headquarters Services, Directorate for Information Operations and Reports (0704-0188), 1215 Jefferson Davis Highway, Suite 1204, Arlington, VA 22202-4302. Respondents should be aware that notwithstanding any other provision of law, no person shall be subject to any penalty for failing to comply with a collection of information if it does not display a currently valid OMB control number. PLEASE DO NOT RETURN YOUR FORM TO THE ABOVE ADDRESS.						
1. REPORT DATE (DD-MM-YYYY) 13-06-2013		2. REPORT TYPE Master's Thesis		3. DATES COVERED (From — To) Jan 2012-Jun 2013		
4. TITLE AND SUBTITLE The Design and Analysis of Electrically Large Custom-Shaped Reflector Antennas				5a. CONTRACT NUMBER		
				5b. GRANT NUMBER		
				5c. PROGRAM ELEMENT NUMBER		
				5d. PROJECT NUMBER		
6. AUTHOR(S) Wilson, Joshua M., Civilian Student, USAF				5e. TASK NUMBER		
				5f. WORK UNIT NUMBER		
7. PERFORMING ORGANIZATION NAME(S) AND ADDRESS(ES) Air Force Institute of Technology Graduate School of Engineering and Management (AFIT/EN) 2950 Hobson Way WPAFB, OH 45433-7765				8. PERFORMING ORGANIZATION REPORT NUMBER AFIT-ENG-13-J-08		
9. SPONSORING / MONITORING AGENCY NAME(S) AND ADDRESS(ES) Intentionally Left Blank				10. SPONSOR/MONITOR'S ACRONYM(S) Intentionally Left Blank		
				11. SPONSOR/MONITOR'S REPORT NUMBER(S) Intentionally Left Blank		
12. DISTRIBUTION / AVAILABILITY STATEMENT DISTRIBUTION STATEMENT A: APPROVED FOR PUBLIC RELEASE; DISTRIBUTION UNLIMITED						
13. SUPPLEMENTARY NOTES This work is declared a work of the U.S. Government and is not subject to copyright protection in the United States.						
14. ABSTRACT Designing and analyzing electrically large reflectors poses numerically complex problems because the reflector must be sampled finely to obtain an accurate solution, causing an unwieldy number of samples. In addition to these complexities, a custom-shaped reflector poses a new analysis problem. Previously developed methods and theorems including Geometric Optics, Ray-Tracing, Surface Equivalence Theorems, Image Theory, and Physical Optics can be applied to these custom-shaped reflectors however. These methods all share in common their capability to provide accurate results in the analysis of electrically large structures. In this thesis, two custom-shaped reflector concepts are explored which include a rectangular shaped, spherically contoured reflector with largest dimension of 305 meters and a cross-shaped, parabolically contoured reflector with largest dimension of 150 meters. Each reflector is intended to operate in the Institute of Electrical and Electronics Engineers (IEEE) L-Band. The reflectors produced differing results, but the same methods apply to each. The motivation for pursuing these custom-shaped reflectors is for earth-based and space-based satellite communications respectively. In this thesis, the plane wave analysis and the ray tracing results are presented for each reflector, and the initial feed design results for the cross-shaped reflector are presented.						
15. SUBJECT TERMS Reflector, Antenna, Electrically Large, Custom-Shaping						
16. SECURITY CLASSIFICATION OF:			17. LIMITATION OF ABSTRACT		18. NUMBER OF PAGES	
a. REPORT U	b. ABSTRACT U	c. THIS PAGE U	UU		19a. NAME OF RESPONSIBLE PERSON Andrew J. Terzuoli (ENG)	
					19b. TELEPHONE NUMBER (include area code) (937) 255-3636 x4717 andrew.terzuoli@afit.edu	